UNIVERSIDAD DE CONCEPCIÓN
FACULTAD DE CIENCIAS FÍSICAS Y MATEMÁTICAS
MAGÍSTER EN ASTRONOMÍA

Magnetic activity of stars using TESS data

Actividad magnética de las estrellas usando datos TESS

Profesor Guía: Dr. Dominik Schleicher
Departamento de Astronomía
Facultad de Ciencias Físicas y Matemáticas
Universidad de Concepción

Tesis para ser presentada a la Dirección de Postgrado de la Universidad de Concepción para optar al grado de Magíster en Astronomía

JAVIERA IGNACIA SOTO BARRIOS
JULIO, 2022
CONCEPCIÓN, CHILE

A mi familia.

AGRADECIMIENTOS

En primer lugar, me gustaría agradecer a mis supervisores, el Dr. Dominik Schleicher y la Dra. Sandra Jeffers, por impulsar el desarrollo de esta investigación. El Profesor Dominik me apoyó en todo momento; gracias por guiarme en este proceso respondiendo inmediatamente a mis dudas de principiante, por ser empático y muy solidario. Gracias a la Dra. Sandra por evaluar con su experiencia mis resultados en cada momento del proyecto.

Al Dr. Ronald Mennickent del Departamento de Astronomia, por su disposición, sugerencias y gran apoyo al proporcionarme valiosas herramientas como softwares y programas de análisis de datos. También quiero agradecer al Dr. Jaime Rosales por ayudarme desde el inicio de este estudio con el manejo y análisis de datos.
Quiero agradecer el apoyo financiero del proyecto regular FONDECYT 1201280, por permitir el desarrollo de esta investigación desde sus inicios.

A mis padres y hermanos, por implusarme a "apuntar alto", celebrar mis logros y creer en mi.
A mi novio, Bastián, por ayudarme cuando más lo necesitaba.
A mis compañeros de pregrado y actuales magíster: Felipe B., Felipe A. y Daniel, por los buenos momentos, las risas y las tardes de estudio antes de los certamenes en la facultad, aprendí mucho con ellos y pasé una bonita vida universitaria.

Resumen

En las últimas décadas, se han realizado numerosos estudios sobre la teoría de la dínamo indicando una importante relación entre el periodo de rotación estelar y actividad magnética. Estos estudios sugieren la existencia de poblaciones de estrellas con diferentes tipos de actividad. Con el fin de determinar la eficacia de dos algoritmos para el análisis de la frecuencia el periodograma de Lomb Scargle generalizado y las ondículas (The weighted wavelet Z-transform (WWZ)) y los aplicamos a dos muestras de estrellas frías. Una muestra de 53 estrellas tomada de Boro Saikia et al. (2018) y una segunda muestra de 168 estrellas tomada de Messina et al. (2022). A partir de esto, comparamos los resultados obtenidos por los autores y los obtenidos en este estudio. El primer paso para el análisis de estas estrellas fue la observación de su curva de luz de las dos muestras de estrellas frías (estrellas de la secuencia principal F,G,K) y la posterior limpieza con Lightkurve y un ajuste con la técnica LOWESS (Locally- Weighted Scatterplot Smoothing). En segundo lugar, y sobre todo con el objetivo de conseguir la precisión necesaria para detectar los periodos, los periodogramas de cada estrella se analizaron en rangos entre 1 y 100 días (con la excepción de los análisis detallados de las variaciones de los de las variaciones en los periodogramas de las estrellas con periodos de rotación inferiores a 1 día) y posteriormente una ventana de observación en rangos de tiempo más pequeños para detectar el periodo más período más destacado en los gráficos de frecuencia frente al tiempo. Después, el análisis de la frecuencia se realizó de forma similar en los diagramas de color proporcionados por una búsqueda de ondículas. Se probaron ambos algoritmos de análisis de frecuencias, demostrando una estrecha concordancia en ambos métodos y sus respectivas incertidumbres. Los resultados de ambos y su comparación con sus antecedentes de investigación se presentan.

Keywords – estrellas: rotación — estrellas: actividad

Abstract

In recent decades, numerous studies have been carried out on dynamo theory indicating an important relationship between the stellar rotation period and magnetic activity. These studies suggested the existence of populations of stars with different types of activity.

In order to determine the effectiveness of two algorithms for frequency analysis: the Generalised Lomb Scargle periodogram and Wavelets (The weighted wavelet Z-transform (WWZ)).And we applied them to two samples of cool stars. A sample of 53 stars taken from Boro Saikia et al. (2018) and a second sample of 168 stars taken from Messina et al. (2022). From this, we compare the results obtained by the authors and those obtained in this study.

The first step for the analysis of these stars was the observation of their light curve of the two cool star samples (F,G,K main sequence stars) and the subsequent cleaning by Lightkurve and an adjustment with the LOWESS technique (Locally-Weighted Scatterplot Smoothing) fit.

Secondly, and particularly with the aim of achieving the required precision to detect the periods, the periodograms of each star were analyzed in ranges between 1 and 100 days (with the exception of the detailed scans of the variations in the periodograms for stars with rotation periods of less than 1 day) and subsequently an observation window was created in smaller time ranges to detect the most prominent period in the frequency versus time plots.

After that, the frequency analysis was similarly performed on the color diagrams provided by a wavelet search.

Both frequency analysis algorithms were tested, demonstrating a close agreement in both methods and their respective uncertainties. The results of both and their comparison with their research background are presented.

Keywords – stars: rotation — stars: activity

Contents

ACKNOWLEDGMENTS i

Resumen ii

Abstract iii

1 Theoretical framework 1
- 1.1 Magnetic activity of Stars . . . 1
  - 1.1.1 Magnetism in the Sun . . . 1
  - 1.1.2 Magnetism in other stars . . . 5
- 1.2 Solar Dynamo Theory . . . 6
- 1.3 Determination of the rotation period: Rossby number . . . 9
  - 1.3.1 Period of magnetic activity . . . 11
    - 1.3.1.1 Magnetic Activity Indicators . . . 12
- 1.4 Importance of the study of the stellar rotation period and magnetism 15

2 Methods 16
- 2.1 Methods and Data . . . 16
  - 2.1.1 Description of the TESS data . . . 16
  - 2.1.2 Lightkurve . . . 17
  - 2.1.3 Background: The Fourier Transform . . . 17
    - 2.1.3.1 Convolution Theorem . . . 19
  - 2.1.4 Generalised Lomb scargle periodogram . . . 20
    - 2.1.4.1 Statistical Distribution . . . 22
  - 2.1.5 Wavelet Transform . . . 23
    - 2.1.5.1 Weighted Wavelet Z-transform (WWZ) . . . 26

3 Results 28
- 3.1 Analyzing the eruptive variable star EV Lac . . . 28
- 3.2 Statistical sample . . . 35
  - 3.2.0.1 Sample of Stars from Boro Saikia et al. (2018) . . 35
  - 3.2.0.2 Sample of stars from Messina et al. (2022) 46

4 Summary and Discussion 52

References **55**

Appendix **64**

A **64**

A1 **Sample of stars from the article by Boro Saikia et al. (2018)** 64

A2 Sample of stars from the article by Messina et al. (2022) 85

List of Tables

3.2.1 Table schematizing the stellar rotation periods calculated according to the Wavelet method and the GLS method, compared with the stellar rotation periods found in the literature. From a total of 53 stars present in Table A.2 of the article Boro Saikia et al. (2018). **References:** (P80)Pettersen (1980), (B17)Brandenburg et al. (2017),(SB99)Saar and Brandenburg (1999), (M99)Messina et al. (1999), (H16)Hempelmann et al. (2016). 35
3.2.2 Complete table containing the 53 analyzed stars from Table A.2 of Boro Saikia et al. (2018). (Continuation of caption, on next page). 36
3.2.3 Table of statistical data resulting from the rotation periods obtained with TESS using wavelets (WWZ). 42
3.2.4 Table of statistical data resulting from the errors associated with the rotation periods obtained with TESS using wavelets (WWZ). 43
3.2.5 Table of statistical data resulting from the rotation periods obtained with TESS using Generalised Lomb-Sacrgle(GLS) method. 43
3.2.6 Table of statistical data resulting from the errors associated with the rotation periods obtained with TESS using Generalised Lomb Scargle(GLS). 44
3.2.7 Reproduction of the star sample of Messina et al. (2022). In the first column we note the analyzed star number of the sample, in the second column its name in the TESS project, in the third column the TESS sector of each star, in the fourth column the stellar rotation period found by Messina et al. (2022), finally in the fifth and sixth columns the rotation periods in determined under the GLS and WWZ method respectively. 47
3.2.8 Table of statistical data resulting from the rotation periods obtained with TESS using wavelets (WWZ). 48
3.2.9 Table of statistical data resulting from the errors associated with the rotation periods obtained with TESS using wavelets (WWZ). 48
3.2.10Table of statistical data resulting from the rotation periods obtained with TESS using Generalised Lomb-Sacrgle(GLS) method. 49
3.2.11Table of statistical data resulting from the errors associated with the rotation periods obtained with TESS using Generalised Lomb Scargle(GLS). 50

List of Figures

1.1.1 Image of the Sun, taken during a period of maximum solar activity, it shows several groups of sunspots. The largest spots in the image are more than 20,000 km across, almost twice the diameter of the Earth. Typical sunspots are only half that size. Images taken by Palomar Observatory/Caltech. Sunspots: (a) Sunspots always seem to occur in pairs of opposite magnetic polarities. An enlarged image of a sunspot pair is shown. Also shown is the structure of a sunspot consisting of a cool, dark umbra surrounded by a warmer, brighter penumbra. (b) A high-resolution image of a typical sunspot is shown, showing surface granules surrounding the sunspot. Image from Carnegie Observatories; SST/Royal Swedish Academy of Sciences. 2

1.1.2 Solar butterfly diagram. (Top panel): The positions of the spots are shown for each rotation of the Sun during the 20th century. During the epoch of solar minimum activity, very few sunspots are seen. While during the epoch of maximum solar activity, the number of spots increases to about 100 spots in a month. (Bottom panel): Sunspots cluster at mid-latitudes, widening and then being displaced toward the equator as the solar cycle progresses. Image from the Solar Group at the NASA Marshall Space Flight Center, by Dr. David Hathaway. 3

1.1.3 Representation of the Solar Minimum (left image). Increase in the number of sunspots at Solar Maximum (right image). This indicates the magnetic variation of the Sun. Image taken from NASA's Solar Dynamics Observatory. 4

1.1.4 (a, b) The Sun's differential rotation coils and deforms the solar magnetic field. (c) Magnetic field lines emerge from the surface and generate a loop generating sunspot pair. The shown pattern of field lines explains the pattern observed later in the sunspot polarities. Illustration taken from Chaisson, E. & McMillan, S. (2017). Astronomy today. (9th edition, Vol.1 and Vol. 2). Pearson. 5

1.2.1 Representation of the **Ω effect**. Differential rotation over the toroidal magnetic field. The light arrows indicate magnetic field lines and the dark arrows indicate the shear flux. Figure taken from Priest (2020). 8

1.2.2 Description of the α **effect**, magnetic flux tubes entering and leaving by convection creating sunspot pairs of opposite directions. Figure taken from Priest (2020). 8
1.2.3 Schematic of the α **effect**. The magnetic field flux enters with upward motions creating a poloidal magnetic field. Figure taken from Priest (2020). 9
1.3.1 On the left we see the relation Böhm-Vitense (2007) of the periods of the activity cycles, Pcyc in years, as a function of the rotation periods, Prot in days, with two important branches, A and I. The "A" sequence of stars showing chromospheric activity and the "I" sequence of cooler and slower rotating stars. The data represented were high quality data taken from Saar and Brandenburg (1999) and Lorente and Montesinos (2005). Crosses indicate stars belonging to sequence "A" and asterisks indicate stars belonging to sequence "I". Square symbols around dots show stars with a B-V < 0.62. The triangles depicted in the figure indicate secondary periods for some stars belonging to the A sequence. The Sun is represented as a blue square. While an update by Boro Saikia et al. (2018) is shown on the right side. Red symbols represent activity cycles classified as CA (cool stars with a well-defined solar activity cycle), green symbols are activity cycles classified as CB (cool stars with multiple cycles), and black symbols are activity cycles classified as CC (cool stars with probable activity cycles). The circles show Mount Wilson stars and the triangles represent HARPS stars. The horizontal black line indicates the midpoint of the maximum cycle length of 25 years. Figure extracted from the Master's Thesis of Fabricio Villegas Villegas (2019). 12

2.1.1 Representation of the convolution between a continuous signal and a rectangular smoothing kernel. The rectangular function is applied to each point of the signal (upper panel), smoothing the original signal (lower panel). Scheme taken from VanderPlas (2018). . . . 19
2.1.2 Visualization of the convolution theorem. The black and gray lines show the real and imaginary parts of the Fourier transform, respectively. Scheme taken from VanderPlas (2018). 20
2.1.3 Schematic of the time and frequency resolutions between the different transformations: Fourier Transform and Wavelet Transform. The size and orientations of the block indicate the size of the resolution. Scheme taken from Ahmet Taspinar (https://ataspinar.com/). 23
2.1.4 Representation of a sine wave and a wavelet. We can see that the sine wave covers the entire time range while the wavelet is localized in the time domain. Scheme taken from Ahmet Taspinar (https://ataspinar.com/). 24

2.1.5 Wavelet families. Discrete wavelets are arranged in the first row and continuous wavelets are arranged in the second row. Scheme taken from Ahmet Taspinar (https://ataspinar.com/). 25

3.1.1 Light curve of the eruptive variable star EV Lac in the optical, in which we can see the flares represented through these eruptions. Image taken from Soto et al. 2022, Boletín 63 Asociación Argentina de Astronomía, accepted. 29
3.1.2 Target pixel file (TPF) of the star EV Lac. The centered red circle corresponds to the source in the field with scaled magnitudes. magnitudes. The white cross indicates the location of the target. The aperture mask used by the pipeline to extract the photometry was also plotted on the TPF. Image taken from Soto et al. 2022, Boletín 63 Asociación Argentina de Astronomía, accepted. 30
3.1.3 We developed the Wavelet analysis of the star EV Lac (TIC 154101678): (A) Time series, star light curve (solid black line) in the optical. (B) Normalized wavelet power spectrum using the Morlet-type wavelet ($\omega_0 = 6$) as a function of time and Fourier equivalent wavelet period (in days). Solid black contour lines enclose regions with greater than 95% confidence relative to a random red noise process ($\alpha = 0.77$). The shaded, dashed area indicates the area affected by the cone of influence of the parent wavelet. (C) C) Global wavelet power spectrum (solid black line) and the power spectrum of the inverse of the Fourier transform (solid gray line). The dashed blue line indicates the 95% confidence level and the dashed red line represents the Fourier transform. (D) Wavelet power averaged over the 2-10 days band (solid black line), power trend (solid black line) and 95% confidence level (dashed black line). Plot of own authorship. 32
3.1.4 Period found by the generalized Lomb-Scargle method using Peranso software. The x-axis indicates the time interval during which the period analysis was performed. The y-axis shows the Lomb-Scargle Theta statistic. Image taken from Soto et al. 2022, Boletín 63 Asociación Argentina de Astronomía, accepted. 33
3.1.5 Phase versus PDCSAP flow window. The pink center line shows the mean curve fit while the vertical dots indicate small, short-lived flares. 34
3.1.6 WWZ transform display. The x-axis represents time, the y-axis represents frequency, and a color (z-axis) is used to plot the WWZ response. The red color shows the most repetitive values indicating a period close to 4.24 days. Image taken from Soto et al. 2022, Boletín 63 Asociación Argentina de Astronomía, accepted. 34
3.2.1 w_{cyc}/Ω vs. R_o^{-1} for the sample of stars in Table A.2 from Boro Saikia et al. (2018) and for the sample obtained from the agreement between the two method analysed: GLS and WWZ. 38

3.2.2 w_{cyc}/Ω vs. R_o^{-1}. *Left*:(a) Sample stars from Table A.2 of Boro Saikia et al. (2018), where CA means Cool stars with clear well defined solar-like activity cycles, CB to refer to Cool stars with multiple cycles and CC to Cool stars with probable activity cycles. *Right*:(b) Reproduction of the stellar rotation periods of the sample of stars in Table A.2. 39
3.2.3 Activity-cycle period in years as a function of rotation period in days for the sample of stars in Table A.2 from Boro Saikia et al. (2018) and for the sample obtained from TESS data showing agreement between the two methods analyzed: GLS and WWZ. 40
3.2.4 P_{rot} versus P_{cyc}. *Left*: (a) Figure 9 of the Boro Saikia et al. (2018) article is shown, for a sample of 53 stars with the same activity cycles, i.e., CA, CB and CC. *Right*: (b) Recreation of the figure on the left, with the new rotation periods found with TESS data. . . 41
3.2.5 Histogram from TESS data for rotation periods obtained with wavelets (WWZ). 42
3.2.7 Histogram from TESS data for rotation periods obtained with Generalised Lomb Scargle(GLS). 44
3.2.8 Histogram of the TESS data for the errors associated with the rotational periods obtained with Generalised Lomb Scargle(GLS). 45
3.2.9 TIC 1102311836 star. *Left*: (a) Light curve. *Right*: (b) Periodogram using GLS. 46
3.2.10 TIC 1102311837 star. *Left*: (a) Light curve. *Right*: (b) Periodogram using GLS. 47
3.2.11 Histogram from TESS data for rotation periods obtained with wavelets (WWZ). 48
3.2.12 Histogram of the TESS data for the errors associated with the rotational periods obtained with wavelets (WWZ). 49
3.2.13 Histogram from TESS data for rotation periods obtained with Generalised Lomb Scargle(GLS). 50
3.2.14 Histogram of the TESS data for the errors associated with the rotational periods obtained with Generalised Lomb Scargle(GLS). 50

Chapter 1

Theoretical framework

In this chapter we will discuss the magnetism in the Sun and other stars, as a way of providing the context for this study.

1.1 Magnetic activity of Stars

1.1.1 Magnetism in the Sun

Among the billions of stars that make up our galaxy, there is one medium-sized star in one arm of the Milky Way spiral: the Sun. For ancient civilizations it was a god and for us, a power plant that generates heat and sustains the existence of life.

Far from what appears to be a motionless point in the glow, the Sun has more complex structures, writhing and glowing. The Sun's magnetic field is behind many of the phenomena on the solar surface. Solar-type stars show solar activity due to magnetism (see, Solanki et al. (2006); de Wijn et al. (2009)).

The Sun's magnetic field is a phenomenon that originates in the interior of the layers, driving solar activity.

The most obvious signs of the presence of solar activity are sunspots. Sunspots occur in the photosphere and are regions of lower temperatures than their surroundings, with intense magnetic fields ($\sim$ 0.1 - 0.5 T). They are limited to low heliocentric latitudes, rarely forming near the solar equator, following Spörer's Law Spoerer (1889).

The first documentation of sunspots appeared in 350 BC, attributed to one of

Aristotle's students, who observed the presence of sunspots. Although sunspots were meticulously observed by Chinese astronomers of the Middle Ages, sunspots were only rediscovered in the West with the advent of telescopes in the 17th century.

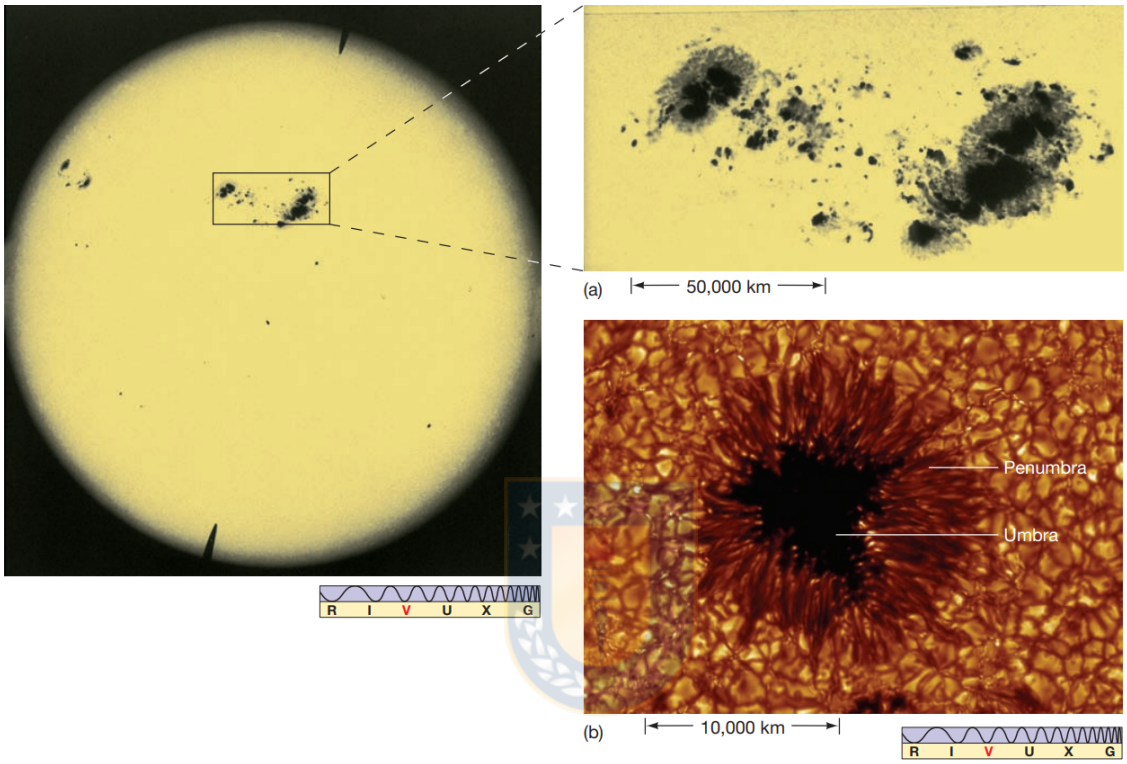

Figure 1.1.1: Image of the Sun, taken during a period of maximum solar activity, it shows several groups of sunspots. The largest spots in the image are more than 20,000 km across, almost twice the diameter of the Earth. Typical sunspots are only half that size. Images taken by Palomar Observatory/Caltech.
Sunspots: (a) Sunspots always seem to occur in pairs of opposite magnetic polarities. An enlarged image of a sunspot pair is shown. Also shown is the structure of a sunspot consisting of a cool, dark umbra surrounded by a warmer, brighter penumbra. (b) A high-resolution image of a typical sunspot is shown, showing surface granules surrounding the sunspot. Image from Carnegie Observatories; SST/Royal Swedish Academy of Sciences.

The sunspot cycle shows great variability in amplitude and variation, taking into consideration the time period from 1645 to 1715, when sunspots became extremely rare. This so-called "quiet period" is also known as the Maunder Minimum Eddy (1976).

Samuel Heinrich Schwabe, who had been systematically observing to discover intra-mercurial planets, determined that the mean number of average sunspots on

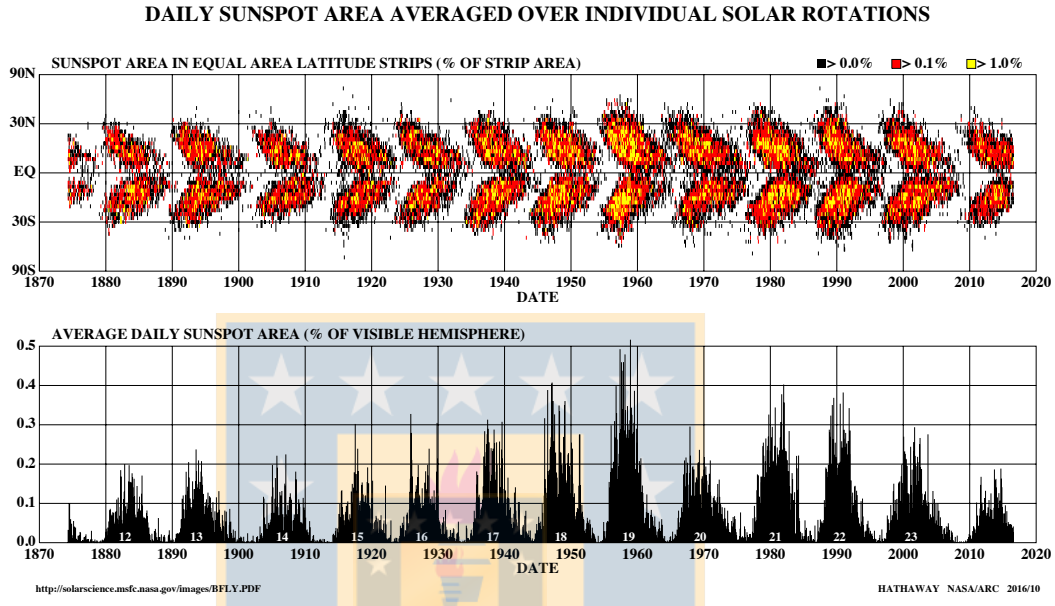

Figure 1.1.2: Solar butterfly diagram. (Top panel): The positions of the spots are shown for each rotation of the Sun during the 20th century. During the epoch of solar minimum activity, very few sunspots are seen. While during the epoch of maximum solar activity, the number of spots increases to about 100 spots in a month. (Bottom panel): Sunspots cluster at mid-latitudes, widening and then being displaced toward the equator as the solar cycle progresses. Image from the Solar Group at the NASA Marshall Space Flight Center, by Dr. David Hathaway.

the solar surface varied cyclically with a period he estimated to be about 10 years Schwabe (1843).

The number of sunspots increases and decreases over a period of 11 years, which corresponds to an energy exchange between the toroidal and poloidal solar magnetic fields. The latitudes where sunspots are located can vary, depending on the solar cycle of the sunspot.

As new sunspots are generated (near the equator), sunspots that are older and located at higher latitudes progressively fade away. Figure 1.1.2 shows a plot of the latitude of observed sunspots as a function of time. During the "Solar Minimum", sunspots are confined between 25° to 30° north and south of the solar

equator. During the "Solar Maximum", sunspots are re-positioned between 15° to 20° from the equator, increasing the number of sunspots. Finally, at the end of the cycle at solar minimum, the number of sunspots has decreased again, and most of the sunspots are located about 10° from the solar equator. Each new cycle seems to overlap with the end of the previous solar cycle.

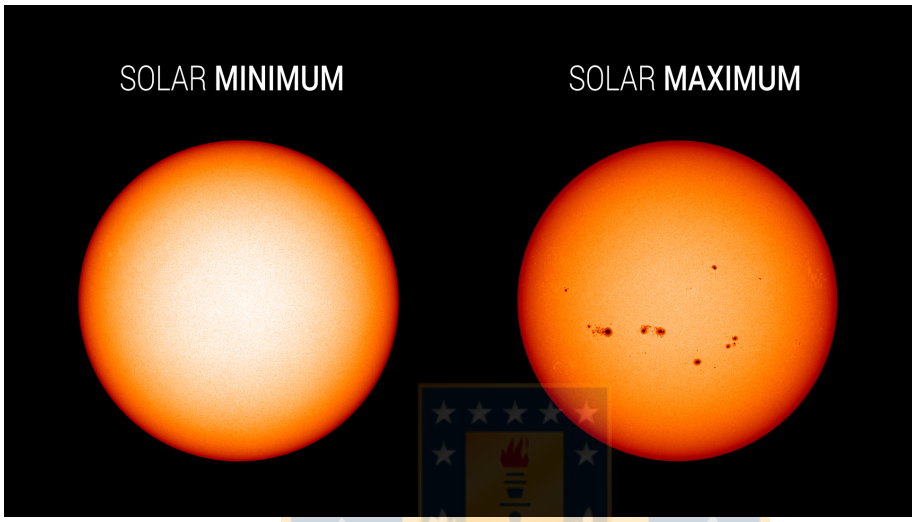

Figure 1.1.3: Representation of the Solar Minimum (left image). Increase in the number of sunspots at Solar Maximum (right image). This indicates the magnetic variation of the Sun. Image taken from NASA's Solar Dynamics Observatory.

During the 11 years of the solar cycle, the leading spot in the sunspot pair in the northern hemisphere of the Sun have the same polarity, while the sunspots in the southern hemisphere indicate an opposite polarity. These polarities reverse their signs in another 11 years, so that the complete solar cycle has a duration of 22 years.
The magnetic polarity of each sunspot pair is known as the Hale cycle Hale et al. (1919).

Recent advances in numerical simulations using a flux transport model and knowledge of the fluxes in the Sun's interior from helioseismology aim to predict the strength of the next solar cycles.

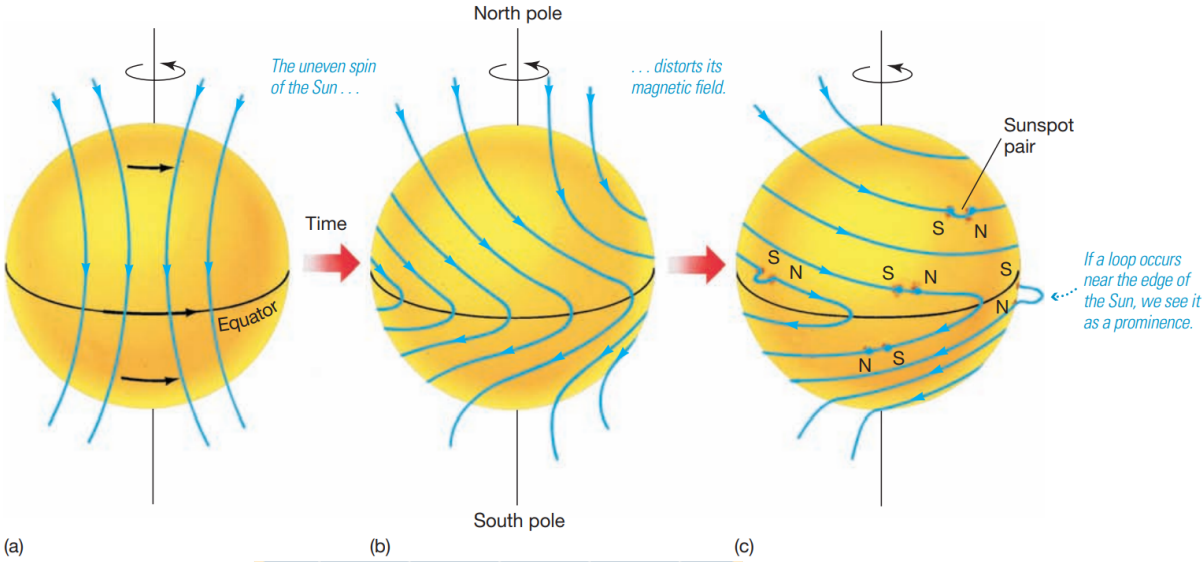

Figure 1.1.4: (a, b) The Sun's differential rotation coils and deforms the solar magnetic field. (c) Magnetic field lines emerge from the surface and generate a loop generating sunspot pair. The shown pattern of field lines explains the pattern observed later in the sunspot polarities. Illustration taken from Chaisson, E. & McMillan, S. (2017). Astronomy today. (9th edition, Vol.1 and Vol. 2). Pearson.

1.1.2 Magnetism in other stars

There are no disturbing doubts about the Sun. The point here is to observe other stars with a similar internal structure as the Sun. The study of stellar magnetic activity makes it possible to test solar dynamo models and to understand stellar magnetic evolution. A wide variety of stars along and outside the Hertzsprung-Russell diagram exhibits magnetic activity.

It has been shown that emission in the H and K-line cores from ionized calcium is a good indicator of chromospheric magnetic activity Noyes et al. (1984).

A sample of more than 100 stars has been monitored about three decades ago and an extensive database has been organized Baliunas et al. (1995). The most outstanding results are:

- Young, rapidly rotating stars show a high level of variable and irregular magnetic activity. Older, slowly rotating stars show Sun-like levels of magnetic activity and magnetic activity cycles with periods ranging from 2 to about 20 years.
- Extremely active stars, such as some binaries and very young stars, can exhibit brightness variations due to huge sunspots by 10%. The relationship

between the brightness of a star and its magnetic activity is dependent on its level of magnetic activity Radick et al. (1998).

- The Sun has an average level of activity but a much smaller photometric variability than other stars. This cycle variability of the Sun is a factor of 2-4 smaller than the variability of stars with a comparable level of activity Radick et al. (1998). A possible explanation for this phenomenon could be the fact that active regions are generated at low latitudes Schatten (1993).
- The level of magnetic activity for stars that have cycles of activity is anti-correlated with the course of the cycle Baliunas and Soon (1995). A similar type of relationship has been observed in the Sun Ossendrijver and Hoyng (1996).

In summary, solar-type stars show a wide variety of behaviors from systematic solar observational databases. Understanding these observations would provide us with more information regarding the Sun.

1.2 Solar Dynamo Theory

It is widely believed that the Sun's magnetic field is generated by a magnetic dynamo inside the Sun. The fact that the Sun's magnetic field changes dramatically over the course of a few years, and the fact that it changes cyclically indicates that the magnetic field continues to be generated within the Sun.
The dynamo mechanism turns out to be a fairly common phenomenon in the cosmos, explaining the origin of the magnetic field in different astronomical systems in the universe.
Larmor (1919) proposed a dynamo process as a possible answer to the mechanism behind the solar magnetic field, through a short paper entitled "How can a rotating body like the Sun become a magnet?". The basis of the theory is that the magnetic field is sustained by the motion of an electrically charged fluid.
The motion of a conductive fluid (such as the highly ionized plasma of the Sun) in which the motion of the fluid induces these electric flows can be expressed as:

- The movement ($\mathbf{u}$) of the electrically conducting fluid through a magnetic field ($\mathbf{B}$) induces an electric field ($\mathbf{u} \times \mathbf{B}$).
- The variation of the magnetic field creates an electric field ($\mathbf{E}$) by Faraday's

law ($\nabla \times \mathbf{E} = -\,\partial\mathbf{B} \,/\, \partial t$).

- This electric field (created in (a) and (b)) incites a current ($\mathbf{j}$) in the fluid, given by Ohm's law for a moving conductor ($\mathbf{j} = \sigma(\mathbf{E} + \mathbf{u} \times \mathbf{B})$).
- The electric current produces a magnetic field by Ampere's law ($\nabla \times \mathbf{B} = \mu_0 \mathbf{j}$).
- The interaction of the magnetic field with the current produces a Lorentz force ($\mathbf{j} \times \mathbf{B}$) acting on the motion of the electrically conducting fluid. Note that this force is quadratic in the magnetic field since $\mathbf{j} = (1/\mu_0)\nabla \times \mathbf{B}$ of Ampere's law.

The induction equation can be defined thanks to the pre-Maxwell equations with Ohm's law for a conductor in motion

$$\frac{\partial \mathbf{B}}{\partial t} = \nabla \times (\mathbf{u} \times \mathbf{B}) + \eta \nabla^2 \mathbf{B}, \tag{1.2.1}$$

where η is the magnetic diffusivity of the fluid.

This equation tells us that there are two processes involved that induce the evolution of the magnetic field B. The second term ($\eta\nabla^2\mathbf{B}$) is a diffusion term leading to the decay of the magnetic field. The first term ($\nabla \times (\mathbf{u} \times \mathbf{B})$) represents the inductive effects of the motions within the fluid leading to an increase of the magnetic field. The equation shows how any gradient in the flow (due to the presence of shear or differential rotation) will lead to a stretching of the poloidal field into toroidal. This process is called the "omega effect". The first part of the dynamo problem can be rephrased as "is there a velocity (u) for which the inductive term is more efficient in generating the field than the diffusive term in destroying the field?". After 50 years, following Larmor's questioning Larmor (1919), several demonstrations have been carried out.

An important step in dynamo theory came with Thomas George Cowling, who put forward Cowling's antidynamo theorem Cowling (1934), which ruled out a wide class of configurations by stating that no stable axisymmetric magnetic field can be maintained by dynamo action.

By separating the toroidal and poloidal magnetic field inside the Sun, the differential rotation produces a stretching of the poloidal magnetic flux, thus generating a new toroidal flux.

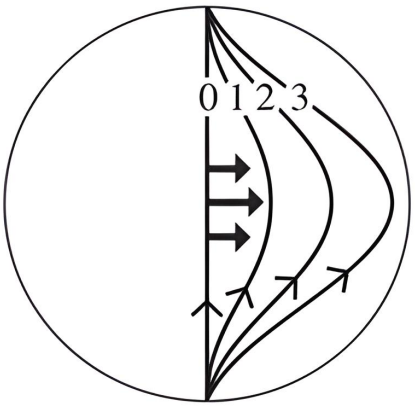

Figure 1.2.1: Representation of the **Ω effect**. Differential rotation over the toroidal magnetic field. The light arrows indicate magnetic field lines and the dark arrows indicate the shear flux. Figure taken from Priest (2020).

Rotation induces anisotropic momentum and energy transport, which defines differential rotation and global meridional circulations that amplify and transport magnetic flux Miesch and Toomre (2009). Rotation also gives way to helical flows and fields that allow promoting hydro-magnetic self-organization by coupling large and small scales.

Parker (1955) and years later Steenbeck et al. (1966) considered the problem of a turbulent flow and a magnetic field varying on two scales.

Parker (1955) expressed that magnetic buoyancy would cause, by convection, the magnetic flux tubes to form sunspot pairs, where, many of these flux cycles would originate through a toroidal flux a poloidal flux through an α **effect** Parker (1955).

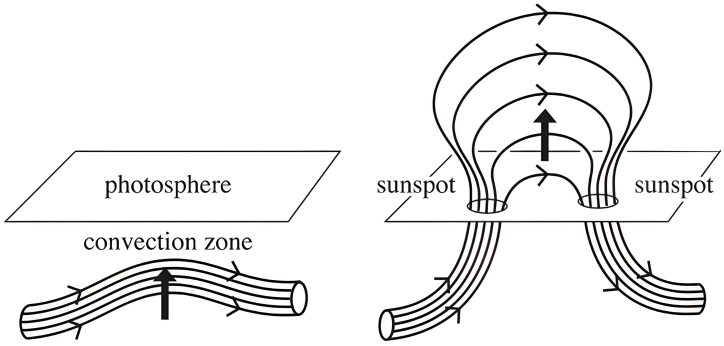

Figure 1.2.2: Description of the α **effect**, magnetic flux tubes entering and leaving by convection creating sunspot pairs of opposite directions. Figure taken from Priest (2020).

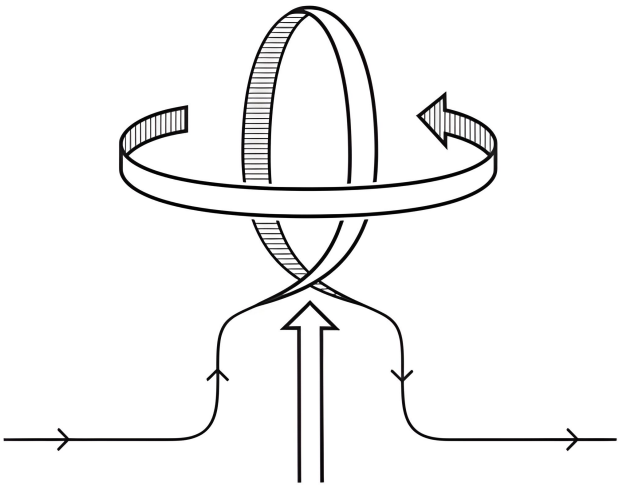

Figure 1.2.3: Schematic of the α **effect**. The magnetic field flux enters with upward motions creating a poloidal magnetic field. Figure taken from Priest (2020).

Recent papers address the issues of solar and stellar convection in detail, see Miesch (2005) and Miesch and Toomre (2009), and Howe (2009) on the observational (helioseismic) front.

1.3 Determination of the rotation period: Rossby number

The triggering of the magnetic fields subsequently involved in the chromospheric activity of stars as measured through the Ca II HK lines and their rotation period has been widely explained as a result of dynamo action Hartmann and Noyes (1987). Stellar rotation has been a key parameter in deriving stellar ages and is closely related to magnetic activity.

One widely used technique for deriving rotation periods has been photometry. Photometry is the process of measuring the brightness of the stars that have been captured. It gives us a direct amount of the energy flux received from celestial objects in a certain wavelength interval.

We can distinguish two types of photometry:

- Differential photometry:

  The magnitude obtained for a variable star is compared with the magnitude

obtained for other stars with known brightness from the literature and located in a nearby field, for the purpose of obtaining a "normalized magnitude" for the variable star.

- Absolute photometry:
  The magnitudes of the stars are measured using the results of the calibration of our system each night and the atmospheric conditions, employing a set of stars outside the field of view.

Photometry allows us to classify stars by means of a color-color diagram, the analysis of light curves through the temporal variation of their magnitude, for the determination of distances and sizes. Photometry also allows us to measure the rotation periods of stars, which is a measure of how fast they rotate and is linked to the generation of magnetic activity.

Another technique was presented by Eberhard and Schwarzschild (1913), where they first proposed the measurement of stellar activity in cool stars through the emission from the core of the Ca II H+K spectral lines. In an attempt to test this hypothesis, the Mount Wilson project measured the chromospheric activity of over a thousand stars Wilson (1968); Duncan et al. (1991), finding that cool stars have cycles of magnetic activity, classifying the stars into an Active Branch and an Inactive Branch. Years later, some stars were found to show intermediate activity, in the parameter space known as the Vaughan-Preston Gap Vaughan and Preston (1980).
Baliunas and Soon (1995) concluded that there are different stellar populations with three distinct activity cycles. The relationship between chromospheric activity and stellar rotation has been pointed out by Kraft (1967) as a product of rotation-dependent dynamo action, which triggers magnetic fields that influence activity (see, Rutten and Schrijver (1987)). Noyes et al. (1984) observed that the calcium emission flux depends on the Rossby number R_o, and reported a possible correlation between the period of the P_{cyc} activity cycle and the Rossby number, $R_o = P_{rot}/4\pi\tau_c$, with P_{rot} being the stellar rotation period and τ_c the stellar convection time scale.

This relation was subsequently studied by Soderblom et al. (1993); Brandenburg

et al. (1998); Saar and Brandenburg (1999); Bohm-Vitense (2007), where $R_o \equiv P_{rot}/\tau_c$. For values of R_o corresponding to faster rotating stars, the activity of the stars shows saturation, while, on the other hand, for higher R_o values, i.e., when the star has a relatively shorter rotation period, the activity and R_o are shown to be correlated Pallavicini et al. (1981); Noyes et al. (1984); Pizzolato et al. (2003).

In a recent study, Boro Saikia et al. (2018) have determined the rotation and activity periods for a larger sample of stars, finding that potentially the relation between rotation and activity period may form a continuum between active and inactive R_o, rather than a strict relation to them.

Some authors such as Schleicher and Mennickent (2017) propose magnetic activity as a possible explanation for the long periods observed in periodic double variables (DPVs) where cyclic variations in their light curve were recorded atypically.

1.3.1 Period of magnetic activity

The Mount Wilson project Wilson (1968) was a project dedicated to measuring the chromospheric activity of over 1000 stars. In it, the sample of stars was classified according to their magnetic activity:

- Stars with active branch
- Stars with an Intermediate level of activity
- Stars of an Inactive branch

On this topic, several authors have led research on the relationship between activity and the rotation period (examples are Noyes et al. (1984);Rutten and Schrijver (1987);Stepien (1993);Baliunas et al. (1996b);Montesinos et al. (2001);Böhm-Vitense (2007); among others).

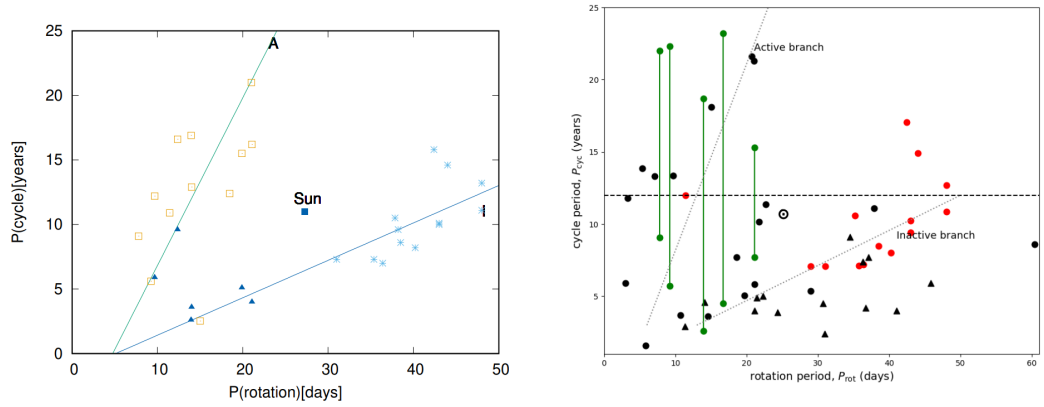

Figure 1.3.1: On the left we see the relation Böhm-Vitense (2007) of the periods of the activity cycles, Pcyc in years, as a function of the rotation periods, Prot in days, with two important branches, A and I. The "A" sequence of stars showing chromospheric activity and the "I" sequence of cooler and slower rotating stars. The data represented were high quality data taken from Saar and Brandenburg (1999) and Lorente and Montesinos (2005). Crosses indicate stars belonging to sequence "A" and asterisks indicate stars belonging to sequence "I". Square symbols around dots show stars with a B-V < 0.62. The triangles depicted in the figure indicate secondary periods for some stars belonging to the A sequence. The Sun is represented as a blue square.
While an update by Boro Saikia et al. (2018) is shown on the right side. Red symbols represent activity cycles classified as CA (cool stars with a well-defined solar activity cycle), green symbols are activity cycles classified as CB (cool stars with multiple cycles), and black symbols are activity cycles classified as CC (cool stars with probable activity cycles). The circles show Mount Wilson stars and the triangles represent HARPS stars. The horizontal black line indicates the midpoint of the maximum cycle length of 25 years. Figure extracted from the Master's Thesis of Fabricio Villegas Villegas (2019).

1.3.1.1 Magnetic Activity Indicators

◇ S-Index

A recognized indicator of chromospheric activity is the S-index Wilson (1968).

It was subsequently introduced by Vaughan et al. (1978) as a dimensionless indicator of Ca II activity using the HKP-1 and HKP-2 spectrometers at the Mount Wilson Observatory (MWO).

The S-index values were denoted as:

$$S - index \;=\; \alpha \frac{H \;+\; K}{R \;+\; V}\;, \tag{1.3.1}$$

where α is an instrumental calibration factor. H and K correspond to the flux measured in a 1.09 Å wide window (FWHM) centered on each line of the Ca II doublet. R and V evaluate the pseudo-continuum on both sides with flux measured in 20 Å wide windows centered at 3900 Å and 4000 Å, respectively. Values of α range from 1.3 Cincunegui et al. (2007) to 5 Gray et al. (2003).
Middelkoop (1982) transformed the S-index to a R_{HK} value (chromosphere emission ratio R_{HK} value described in equation 1.3.2) as a function of B-V, from a sample of 85 main sequence stars, in order to eliminate the color independence of the S-index and the photospheric contribution of some quiescent stars in the H and K flux measurements. Defining

$$R_{HK} = 1.34 \times 10^{-4} C_{cf} S \, , \tag{1.3.2}$$

Rutten (1984) created a new conversion for the C_{cf} factor (conversion factor) given by Middelkoop (1982) by extending the number of stars studied to 30 main sequence stars and 27 giant stars, with improved fits via,

$$log\ C_{cf} = 0.25(B-V)^3 - 1.33(B-V)^2 + 0.43(B-V) + 0.24 \, , \tag{1.3.3}$$

in main sequence stars with $0.3 \leq B - V \leq 1.6$ Rutten (1984) and,

$$log\ C_{cf} = -0.066(B-V)^3 - 0.25(B-V)^2 - 0.49(B-V) + 0.45 \, , \tag{1.3.4}$$

for giant stars between $0.3 \leq B - V \leq 1.7$ Middelkoop (1982).
The use of this new relation originates from a larger sample of stars and the relations between B - V, T_{eff} and BC (Bolometric Correction).
Schröder et al. (2009) used the expression given by Rutten (1984) to modify the photospheric contribution to the flux in the Ca II line cores, Noyes et al. (1984). They obtained

$$log\ R_{phot} = -4.898 + 1.918(B-V)^2 - 2.893(B-V)^3 \tag{1.3.5}$$

in the category of $0.44\langle(B-V)\rangle 0.82$, which delivers the photospheric component for the correction

$$R'_{HK} = R_{HK} - R_{phot} \, . \tag{1.3.6}$$

For values of $B - V > 0.82$ the photospheric contribution is within the expectation and in good agreement, but negligible for $B - V \geq 1$ Noyes et al. (1984).

◇ **Log R'_{HK}**

It measures the chromospheric contribution of the H and K Ca lines without the photospheric component in the lines.

Noyes et al. (1984) detected a relationship between R_o and $log\ R_{HK}$ that indicates a smaller scatter for α values in the (1.3.1) equation. For a convective time τ_c and a rotation period P, one can obtain the dimensionless Rossby number $R_o = P_{obs}/\tau_c$ which allows a description of chromospheric activity that is better than rotational activity alone.

◇ **X-Ray Luminosity**

X-ray emissions have been detected in flares as well as in "quiet" emissions, an example is the star HD 85945 Haisch and Schmitt (1994).

Some authors such as Mathioudakis and Doyle (1992) noted that X-ray emission is related to Mg II emission in active stars, causing chromospheric and coronal heating.

Other authors, such as Mullan and Johnson (1995), performed modeling of the chromosphere of X-ray stars using the flaring loops of magnetic fields heated due to resonant magneto-hydrodynamic absorption. They noted that these loops had resonance times that matched the convection times.

The relationship between X-ray emission and point waves fits quite well with the magnetic model of chromospheric and coronal heating (Kürster, 1996), proposing that the magnetic field motions unfold as magnetic flux tubes entering and exiting through the photosphere, tubes of material generating motions in the crosmosphere, finally launching jets of material into the stellar corona.

1.4 Importance of the study of the stellar rotation period and magnetism

The rotation period of a star has turned out to be a key parameter for the understanding of the stellar dynamo and the generation of magnetic fields in cool stars with outward convection zones Ruediger (1989); Rüdiger and Hollerbach (2004).

Stellar rotation measurements have proven to be essential in stellar astrophysics, in determining the age and activity of a star.

Although rotation itself is not an activity phenomenon, it exerts a crucial role in stellar dynamos. Differential rotation determines whether a dynamo resembles an $\alpha\Omega$ or α^2 dynamo; for more details see Charbonneau (2010).

The Sun has well-studied and well-known parameters. Studying solar-type stars describes how stars that resemble our Sun behave. It allows us to see how the dynamo behaves and influences its interior.

The understanding of stellar rotation periods shows us the impact it can have when related to the cyclic period. It has given us clues on how to change our concept of what was understood, for example Böhm-Vitense (2007), observed that the stars he analyzed behaved like what was obtained in Saar and Brandenburg (1999). But he noted that there were stars that did not fit either of the two branches of activity (active branch and inactive branch), hypothesizing that different dynamo types were influencing a certain group of stars.

The reproduction of the calculations of the rotation periods could give us clues as to how the different types of dynamos proposed by Böhm-Vitense (2007) behave. It allows us to understand if the stellar rotation periods obtained by this study are similar to those obtained in the literature. To test the effectiveness of two frequency analysis methods, we will test: Generalized Lomb Scargle and Wavelets (which will be discussed in more detail in the next chapter).

Chapter 2

Methods

In this chapter we show a description of data extraction with TESS and methods used for frequency analysis.

2.1 Methods and Data

2.1.1 Description of the TESS data

The Transiting Exoplanet Survey Satellite (TESS) Ricker et al. (2015) is a space telescope that is part of the NASA Exploration Program led by MIT. TESS was launched on April 18, 2018 via a SpaceX Falcon 9 rocket.

The TESS telescope uses four cameras covering each sector. These cameras have four CCDs with a pixel scale of 21 arcseconds per pixel providing a huge field of view of $24° \times 96°$.

TESS observations are classified into sectors. For each sector, the pointing of the spacecraft is kept invariant with respect to the celestial reference frame. His oriented along a line of longitude of the ecliptic with the instrument pointing at an ecliptic latitude of $\pm 54°$, which centers Camera 4 at one pole of the ecliptic. Each sector comprises two continuous orbits with a period of $P_{TESS} \approx 13.7$ d. During each sector, the entire field of view is surveyed as full frame images (FFI) at a cadence of 30 min, and at a cadence of 2 min for selected targets.

It is designed to search for exoplanets using the transit method by scanning a large area of space in which it will monitor more than 200,000 stars over a two-year period. It is sensitive to low amplitude and short duration events, such

as flares. Its photometric bandpass ($\sim 600 - 1000\ nm$) is more sensitive to redder wavelengths compared to Kepler Borucki (2017).

2.1.2 Lightkurve

Lightkurve [1] Lightkurve Collaboration et al. (2018) is an open source Python package that offers a nice way to handle analysis of astronomical flux time series data, such as pixels and light curves obtained from NASA's Kepler and TESS exoplanet missions [2].

It aims to support the analysis of time series data on planets, stars and galaxies obtained by telescopes that collect images in visible or infrared light.

Its main uses include:

- Obtaining Kepler and TESS data programmatically from their data files.
- Reading, visualizing and interacting with Kepler and TESS pipeline products.
- Extracting light curves from pixel data using custom aperture masks; perform common light curve operations (e.g., folding, clustering, outlier removal).
- Extract different types of periodograms.
- Systematic removal using adjustable implementations of the most common systematic removal strategies.

2.1.3 Background: The Fourier Transform

As a way to give a clear interpretation of the generalized Lomb Scargle periodogram and wavelets, we will begin by analyzing the Fourier transform.
Given a continuous signal designated g(t), the Fourier transform is given by the following integral,

$$\hat{g}(f) \equiv \int_{-\infty}^{\infty} g(t) e^{-2\pi_i f t} dt \ , \tag{2.1.1}$$

[1] https://docs.lightkurve.org/
[2] https://tess.mit.edu/

where $i \equiv \sqrt{-1}$ represents the imaginary unit.
The inverse Fourier transform is given by

$$g(t) \equiv \int_{-\infty}^{\infty} \hat{g}(f) e^{+2\pi_i f t} df \ . \tag{2.1.2}$$

We will also define the Fourier transform operator $\mathcal{F}$, so that

$$\mathcal{F}\{g\} \ = \hat{g} \ , \tag{2.1.3}$$

$$\mathcal{F}^{-1}\{\hat{g}\} \ = \ g \ . \tag{2.1.4}$$

The functions g and $\hat{g}$ are known as even Fourier functions, denote as g $\Longleftrightarrow$ $\hat{g}$.

Some properties of the Fourier Transform

We will highlight some of the properties of the Fourier transform, which are useful when analyzing signals:

i. The Fourier transform is a linear operation:

For given constant A, and given functions f(t) and g(t), we can write

$$\mathcal{F}\{f(t) \ + \ g(t)\} \ = \ \mathcal{F}\{f(t)\} + \mathcal{F}\{g(t)\} \ , \tag{2.1.5}$$

$$\mathcal{F}\{Af(t)\} \ = \ A\mathcal{F}\{f(t)\} \ . \tag{2.1.6}$$

ii. The Fourier transform of a sinusoid with frequency f_0 is a sum of delta functions at $\pm f_0$:

From the definition of the Dirac delta function,

$$\delta(f) \ \equiv \ \int_{-\infty}^{\infty} e^{-2\pi i x f} df \ , \tag{2.1.7}$$

we can write

$$\mathcal{F}\{e^{2\pi f_0 t}\} \ = \ \delta(f \ - \ f_0) \ . \tag{2.1.8}$$

According to Euler's formula $e^{ix} \ = \ cosx \ + \ i \ sinx$, we have the following identities:

$$\mathcal{F}\{cos(2\pi f_0 t)\} \ = \ \frac{1}{2}[\delta(f \ - \ f_{0)} \ + \ \delta(f \ + \ f_0)] \ , \tag{2.1.9}$$

$$\mathcal{F}\{sin(2\pi f_0 t)\} \ = \ \frac{1}{2i}[\delta(f \ - \ f_{0)} \ - \ \delta(f \ + \ f_0)] \ . \tag{2.1.10}$$

Therefore, for a sinusoidal signal with a frequency f_0, the Fourier Transform is

the sum of the delta functions at $\pm f_0$. The study of the Fourier Transform proves to be effective for the study of periodic signals.

2.1.3.1 Convolution Theorem

The convolution theorem states that the Fourier Transform of a convolution is the dotted product of the transforms, usually denoted by the symbol *

$$[f * g](t) \equiv \int_{-\infty}^{\infty} f(\tau)g(t - \tau)d\tau \ . \tag{2.1.11}$$

It can be understood as an operation that "slides" one function over another function, smoothing the resulting function.

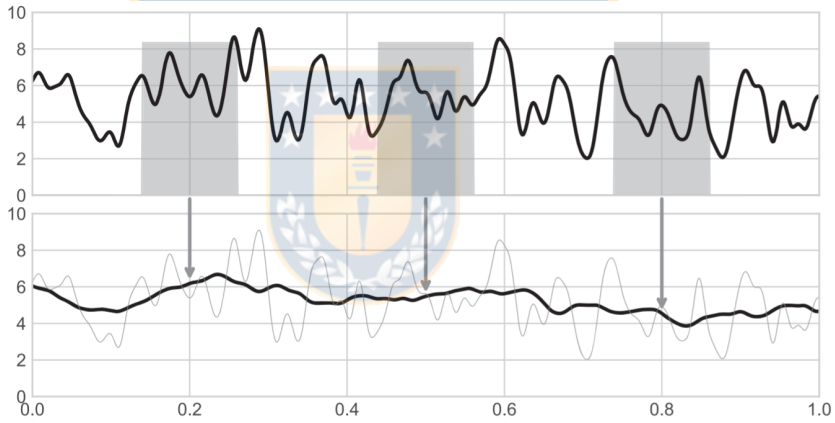

Figure 2.1.1: Representation of the convolution between a continuous signal and a rectangular smoothing kernel. The rectangular function is applied to each point of the signal (upper panel), smoothing the original signal (lower panel). Scheme taken from VanderPlas (2018).

The Fourier transform of the convolution corresponds to the product of the individual transforms,

$$\mathcal{F}\{f * g\} = \mathcal{F}\{f\} \cdot \mathcal{F}\{g\} \ . \tag{2.1.12}$$

This equation is known as the Convolution Theorem.

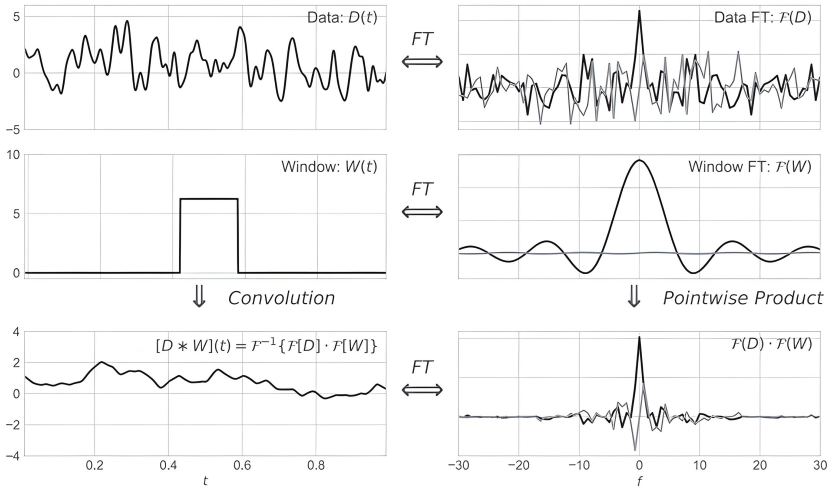

Figure 2.1.2: Visualization of the convolution theorem. The black and gray lines show the real and imaginary parts of the Fourier transform, respectively. Scheme taken from VanderPlas (2018).

The Fourier Transform of a product is the convolution of both transforms

$$\mathcal{F}\{f \cdot g\} = \mathcal{F}\{f\} * \mathcal{F}\{g\} . \tag{2.1.13}$$

2.1.4 Generalised Lomb scargle periodogram

The Lomb-Scargle Scargle (1982) periodogram was implemented as a useful tool in the analysis of periods and frequencies of data. The method is equivalent to sine wave fitting of the form $y = a\ coswt + b\ sinwt$ Barning (1963).
Lomb (1976) and Scargle (1982) studied the statistical behavior of this method. Using a time series (t_i, y_i) with zero mean ($\bar{y} = 0$) the Lomb-Scargle periodogram was defined as

$$\hat{p}(\omega) = \frac{1}{\hat{Y}Y}\left[\frac{\hat{Y}C_{\hat{\tau}}^2}{\hat{C}C_{\hat{\tau}}} + \frac{\hat{Y}S_{\hat{\tau}}^2}{\hat{S}S_{\hat{\tau}}}\right] \tag{2.1.14}$$

$$= \frac{1}{\sum_i y_i^2}\left\{\frac{[\sum_i y_i cosw(t_i - \hat{\tau})]^2}{\sum_i cos^2\ w(t_i - \hat{\tau})} + \frac{[\sum_i y_i sin\ w(t_i - \hat{\tau})]^2}{\sum_i sin^2\ w(t_i - \hat{\tau})}\right\} , \tag{2.1.15}$$

where, the parameter $\hat{\tau}$ is calculated

$$tan\ 2w\hat{\tau} = \frac{\sum_i sin\ 2wt_i}{\sum_i cos\ 2wt_i} . \tag{2.1.16}$$

However, the Lomb-Scargle periodogram does not consider measurement errors.

For the data analysis, the difference between the mean of the data is applied, showing that the mean of the data and the mean of the fitted sine function are equal.
Cumming et al. (2008), by adding a constant shift c, achieved a further generalization of this periodogram, of the form $y = a\ coswt\ +\ b\ sinwt\ +\ c$.

The generalised lomb scargle (GLS) periodogram Zechmeister and Kürster (2009) is a commonly used statistical tool that allows efficient calculation of a Fourier-type estimator power spectrum from unevenly sampled data, resulting in an intuitive means of determining the period of oscillations. GLS considers measurement errors and a constant variable in the wave function fit.
Let y_i be the N measurements of a time series at time t_i and with errors σi. The fit of a complete sine function is then given as

$$y(t) = a\ cos\ \omega t + b\ sin\ \omega t + c \tag{2.1.17}$$

at a certain frequency ω. Therefore, minimising the squared difference between y_i and the model function $y(t)$,

$$\chi^2 = \sum_{i=1}^{N} \frac{[y_i - y(t_i)]^2}{\sigma_i^2} = W \sum \mathtt{w}_i [y_i - y(t_i)]^2\ , \tag{2.1.18}$$

where

$$\mathtt{w}_i = \frac{1}{W}\frac{1}{\sigma_i^2} \qquad (W = \sum \frac{1}{\sigma_i^2} \qquad \sum \mathtt{w}_i = 1) \tag{2.1.19}$$

corresponds to the normalised weights. The generalised Lomb-Scargle periodogram $p(\omega)$ normalised in a range of $0 \leq p \leq 1$ (where p = 0 means an inadequate adjustment and p = 1 indicates a "perfect fit", i.e, 100% of reduction of χ^2 or χ^2=0), with

$$p(\omega) = \frac{\chi_0^2 - \chi^2(\omega)}{\chi_0^2}. \tag{2.1.20}$$

After several steps, the generalised Lomb-Scargle periodogram at an arbitrary time of reference τ ($t_i \rightarrow\ t_i\ -\ \tau$) becomes

$$p(\omega) = \frac{1}{YY}\left[\frac{YC_\tau^2}{CC_\tau} + \frac{YS_\tau^2}{SS_\tau}\right] , \tag{2.1.21}$$

where $Y = \sum w_i y_i$, $C = \sum w_i \; cos \; \omega t_i$ and $S = \sum w_i \; sin \; \omega t_i$.
Examples of statistical analyses characterizing the periodicity in time series have been derived, among others, by Scargle (1998).

2.1.4.1 Statistical Distribution

The false alarm probability (FAP) is a metric that expresses the importance of a period. A false alarm occurs in period analysis techniques when a period is incorrectly found that does not actually exist. In the development of the NASA Exoplanet Archive, the power of the periodogram is normalized by the inverse of the variance of the original signal data. Horne and Baliunas Horne and Baliunas (1986) showed that this scaled power has an exponential distribution for data values with Gaussian noise and a large number of number of independent frequencies, N_i observations. The probability p of observing a power less than or equal to P_0 in a sample when the time series is a noise signal is given by:

$$p \; = \; Pr \; \{P <= \; P_0\} \; = \; 1 \; - \; e^{-P_0} \; , \tag{2.1.22}$$

whereas, the probability of finding a value exceeding this value is given as,

$$pv \; = \; 1 \; - \; p^M \; , \tag{2.1.23}$$

where M corresponds to the number of periods sampled.
The above expression ceases to be valid within a small number of observations, N_{obs}. When N_{obs} is less than 50, the following formula is applied as in Zechmeister and Kürster (2009):

$$p \; = \; Pr \; \{P <= \; P_0\} \; = \; (1 \; - \; \frac{2P}{N \; - \; 1})^{\frac{N \; - \; 3}{2}} \tag{2.1.24}$$

and

$$pv \; = \; 1 \; - \; p^M \; , \tag{2.1.25}$$

where M equals the number of independent frequencies. The theoretical value of independent frequencies for a given data set is between N and $N \cdot (N-1)/2$. Therefore, the number of independent frequencies is determined as,

$$M = \frac{maxf - minf}{df} \tag{2.1.26}$$

where df is the width (in frequency) of an upper peak in the periodogram Zechmeister and Kürster (2009). The initial and final values of a peak are denoted as the frequencies at which the power is half the maximum of the peak.

2.1.5 Wavelet Transform

The Wavelet transform Torrence and Compo (1998) is a method for analyzing signals with a dynamic frequency spectrum.
The Wavelet transform has a high resolution in both the frequency and time domain. It not only tells us what frequencies are present in a signal, but also at what time those frequencies have been produced. This is achieved by working with different time scales Burrus C. (1998). We can schematically summarize the frequency resolutions by making a variation of the time series:

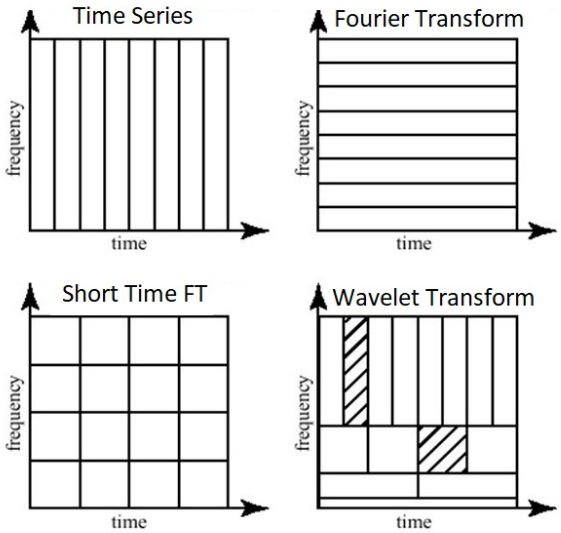

Figure 2.1.3: Schematic of the time and frequency resolutions between the different transformations: Fourier Transform and Wavelet Transform. The size and orientations of the block indicate the size of the resolution. Scheme taken from Ahmet Taspinar (https://ataspinar.com/).

- For small frequencies a high resolution in the frequency domain, low resolution in the time domain.
- For large frequencies a low resolution in the frequency domain, high resolution in the time domain.

The Wavelet transform consists of a series of functions called wavelets. We can analogously decompose the light curve of a star by frequencies represented in the power spectrum at different scales. The wavelet being placed in time, our signal can be convoluted with the wavelet in different time ranges.

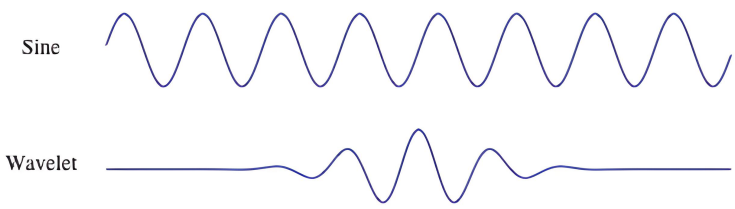

Figure 2.1.4: Representation of a sine wave and a wavelet. We can see that the sine wave covers the entire time range while the wavelet is localized in the time domain. Scheme taken from Ahmet Taspinar (https://ataspinar.com/).

We can define this scale as

$$f_a = \frac{f_c}{a}\,, \tag{2.1.27}$$

where f_a is equivalent to the pseudo-frequency, f_c is the center frequency of the mother wavelet and a is the scaling factor.
A higher scale factor (longer wavelet) allows us to visualize and analyze smaller frequencies and therefore we obtain a higher resolution in the frequency domain. Similarly, by applying smaller scales we will have a higher resolution in the time domain.
Several studies have pioneered with the use of Wavelets:
Frick et al. (1997) applied a wavelet analysis to study the irregular behavior of the chromospheric activity in the data obtained from the observations of the HK project of the Mount Wilson Observatory. In this analysis, the wavelet transform and energy spectra were calculated for four stars: HD 3651, HD 10700, HD 10476 and HD 201091.
Bravo et al. (2014) applied the so-called Morlet wavelet to Kepler and CoRoT light curves, in stars with planetary transits, binary systems, a variable star dominated by magnetic activity, and pulsating stars, where they identified

patterns in the rotation period due to active regions affecting the light curves.

Wavelet Families

There are numerous families of wavelets. Each wavelet family is different and has a representative shape according to its smoothness and appearance. We can choose which type of wavelet best suits our data.
A wavelet must meet two mathematical conditions called normalization and orthogonalization constraints:

- Finite energy:
  Means that it is localized in time and frequency; it is integrable and the inner product between the wavelet and the signal always exists.
- Zero mean:
  The admissibility condition implies that a wavelet has zero mean in the time domain, at zero frequency in the time domain. This is necessary to ensure that it is integrable and also the inverse of the wavelet transform can be calculated.

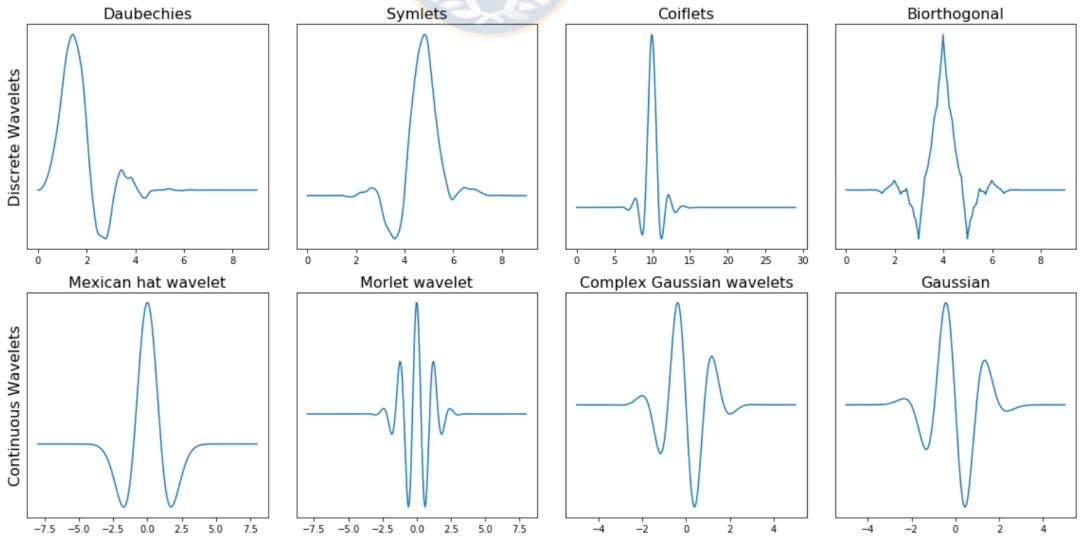

Figure 2.1.5: Wavelet families. Discrete wavelets are arranged in the first row and continuous wavelets are arranged in the second row. Scheme taken from Ahmet Taspinar (https://ataspinar.com/).

The continuous wavelet transform is mathematically described as

$$X_\omega(a,b) \;=\; \frac{1}{\|a\|^1/2}\int_{-\infty}^{\infty} x(t)\bar{\psi}\left(\frac{t\;-\;b}{a}\right)\,dt\;, \tag{2.1.28}$$

where ψ corresponds to the mother wavelet, "a" to the scale factor shifted by a factor "b"; with a and b as continuous values.
For the case of the discrete wavelet transform (DWT), it uses discrete values for both its scale and translation factor. The scale factor increases progressively in even powers, i.e., a= 1,2,4,... and for the shift factor b, it increases in integer values, i.e., b=1,2,3,.... .

2.1.5.1 Weighted Wavelet Z-transform (WWZ)

In 1996, Foster (1996) developed the weighted wavelet z-transform. His method widely used in variability analysis based on the principle of the wavelet transform. It is a very useful tool for discerning the time evolution of period and amplitude from visual observations of long period variables. The wavelet transform can be considered as a a projection,

$$y(t) \;=\; \sum_a y_a\varphi_a(t)\;, \tag{2.1.29}$$

where the function $\varphi_a(t)$ represents the wavelet function. The purpose of the wavelet transform is to expand a signal into a series of coefficients with a given energy and to retain fine and coarse details at different scales.
The weighted wavelet Z-transform corresponds to a projection of functions $y(t) \;=\; \sum_a\; y_a\varphi_a(t)$, with a statistical approach to plot the response as a function of two variables, where the X-axis represents time, the Y-axis represents frequency and a color (Z-axis) is used to plot the WWZ response. From Foster (1996),

$$\varphi_1(t) \;=\; 1(t)\;, \tag{2.1.30}$$

$$\varphi_2(t) \;=\; cos(\omega(t\;-\;\tau))\;, \tag{2.1.31}$$

$$\varphi_3(t) \;=\; sin(\omega(t\;-\;\tau))\;, \tag{2.1.32}$$

where each WWZ projection incorporates the statistical weights and the addition of a constant function solves the non-zero mean value problem.
We denote

$$w_\alpha = e^{-cw^2(t_\alpha-\tau)^2}, \tag{2.1.33}$$

which corresponds to a fragment of the Morlet wavelet, $\varphi(t) = e^{iw(t-\tau)}e^{-cw^2(t_\alpha-\tau)^2}$ with the constant c as a factor measuring the wavelet decay rate.
Therefore, the weighted wavelet Z-transform can be denoted as

$$WWZ = \frac{N_{eff} - 3}{2(V_x - V_y)}, \tag{2.1.34}$$

where

$$N_{eff} = \frac{\sum w_\alpha^2}{\sum w_\alpha^2} = \frac{[\sum e^{-cw^2(t_\alpha-\tau)^2}]^2}{\sum e^{-2cw^2(t_\alpha-\tau)^2}}, \tag{2.1.35}$$

where N_{eff} is the effective number of data that represents the statistical density of the data,

$$V_x = \frac{\sum_\alpha w_\alpha x^2(t_\alpha)}{\sum \lambda w_\lambda} - \left[\frac{\sum_\alpha w_\alpha x(t_\alpha)}{\sum \lambda w_\lambda}\right]^2, \tag{2.1.36}$$

with V_x the weighted variation of the data,

$$V_y = \frac{\sum_\alpha w_\alpha y^2(t_\alpha)}{\sum \lambda w_\lambda} - \left[\frac{\sum_\alpha w_\alpha y(t_\alpha)}{\sum \lambda w_\lambda}\right]^2, \tag{2.1.37}$$

and V_y the weighted variation of the model function. It follows an F distribution with $N_{eff} - 3$ and 2 degrees of freedom, and an expected value of 1.
For more mathematical details, see Foster (1996).
As visualized, the constant decay factor c measures how fast the exponential term $(-cw^2(t_\alpha - \tau)^2)$ in the wavelet function decreases in a $(2\pi/w)$ cycle. That is, c defines a constraint on the width of the frequency window. Large c values allow identifying low-frequency components in detail.

Chapter 3

Results

In this section we show an analysis using both methods and their results, for two star samples: one from the paper by Boro Saikia et al. (2018) and one from Messina et al. (2022).

3.1 Analyzing the eruptive variable star EV Lac

In order to verify the effectiveness of the tested methods, we analyze a test star of previously known rotation period.

The star EV Lac (TIC 154101678; R.A = 22:46:49.73 , Dec = +44:20:02.37 (J2000)), 16.5 light-years from the solar system in the constellation Lacerta, is one of our closest stellar neighbors. Better known as EV Lacertae, it is a common red dwarf, like most of the stars in the firmament. Many researchers have been suspicious about the magnitude variations presented in the quiet state of the eruptive star EV Lac.

Pettersen (1980) was the first to determine a rotation period for this star, successfully finding a periodic light variation of 0.07 in magnitude V with a period of 4.378 days resulting from three months of photometric observation in 1979. This periodicity was later confirmed by Pettersen et al. (1983) and Roizman (1984). The analogy with magnetically driven sunspots in the photosphere of the sun directed research for observational support of the starspot theory (see Vogt (1981); Berdyugina (2005)). Since sunspots exhibit a periodicity and their regions are often associated with regions of active plague, which in turn are often associated with the development of solar flares, one would expect, by analogy in

the case of stars, a periodicity in flare activity and a correlation of flare activity with stellar luminosity.

Mavridis and Avgoloupis (1986) have demonstrated the existence of a 5-year cycle in EV Lac in both the mean steady-state luminosity and the level of flare activity. Doyle (1987) has found a correlation between flare frequency and rotation period for the years 1973 to 1976, but not for the years 1976 to 1982. Pettersen et al. (1992) have found periodic light variations of about 0.1 in V magnitude, with a period of 4.376 days and flat light curve periods which they have attributed to the restructuring of starspot zones during the decade 1980-1890.

Spectroscopic analyses of flares and CMEs in M dwarf stars are shown by Priest (2020), who found 27 active flares during 457 hours of TESS observation.

With this in mind, we can define a time series of brightness as the light curve of a star.

The light curves of stars observed by the Kepler, K2 or TESS missions are created from the raw images collected by these telescopes using software created for this purpose by the mission teams.

TESS observes EV Lac in sector 16. This eruptive star has been known and classified as a flare star since about 67 years Roques (1955). EV Lac produces flares at X-ray (see, Schmitt (1994); Sciortino et al. (1999); Favata et al. (2000); Huenemoerder et al. (2010)), UV (see, Ambruster et al. (1986); Pomerance et al. (1995)), optical (see, Kodaira et al. (1976); Abdul-Aziz et al. (1995)), and radio wavelengths (see, White et al. (1989); Abdul-Aziz et al. (1995)).

We extracted the light curve from the Mikulski Archive for Space Telescopes (MAST) using Lightkurve Lightkurve Collaboration et al. (2018).

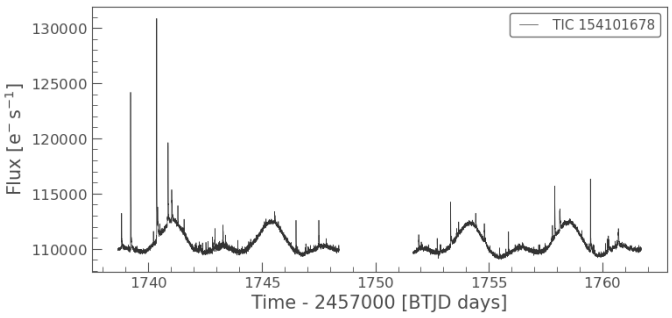

Figure 3.1.1: Light curve of the eruptive variable star EV Lac in the optical, in which we can see the flares represented through these eruptions. Image taken from Soto et al. 2022, Boletín 63 Asociación Argentina de Astronomía, accepted.

We then used Target Pixel Files (TPF). Target Pixel File are files common to Kepler/K2 and the TESS mission. They correspond to movies consisting of data pixels centered on a single target. They are equivalent to stacks of images, with one image for each timestamp at which the data were taken. Each one is called a cadence. These images are "postage stamps" cropped from the full observation for ease of work. Each of the pixels is 4 arc seconds wide.

The point spread function (PSF) of the telescope causes the starlight to fall on several different pixels. Because of this scattering, it is necessary to sum a collection of many pixels to consider all the light from the source by summing all the pixels in an aperture. Aperture photometry is the simple act of summing the values of all pixels of a predefined aperture, as a function of time. By carefully choosing the shape of the aperture mask, you can avoid nearby contaminants or improve the quality of the source signal you are trying to measure relative to the background. By summing all aperture pixels, a single aperture photometry light curve (SAP) is created.

In this work we applied custom apertures via "create_threshold_mask(threshold=3)" which selects all pixels that have a flux greater than 3 standard deviations above the mean luminosity, representing the drawn aperture mask that is used to determine the light fraction of each star in the Target Pixel File (TPF) (see Aller et al. (2020)).

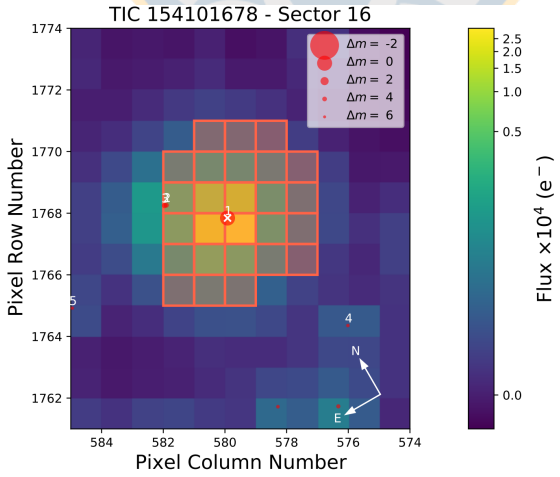

Figure 3.1.2: Target pixel file (TPF) of the star EV Lac. The centered red circle corresponds to the source in the field with scaled magnitudes. magnitudes. The white cross indicates the location of the target. The aperture mask used by the pipeline to extract the photometry was also plotted on the TPF. Image taken from Soto et al. 2022, Boletín 63 Asociación Argentina de Astronomía, accepted.

The aperture of the pipe is small in this case, but it avoids capturing the light from the background star. Once the light curve is altered, we save it as a FITS file.
The SPOC pipeline provides target pixel files, light curves from two-minute cadence target data. It contains SAP (Single Aperture Photometry) data and pre-search data conditioning SAP (PDCSAP) stream. For the purpose of this research, the PDCSAP light curves are used, where the PDCSAP stream is characterized by cleaner data than the SAP stream and fewer systematic trends.

To access the data, we made use of the Fv software [1] in order to visualize the data and eliminate outliers (if applicable). In this way, the resulting light curve in this study is a clean light curve without eruptions (see Figure 3.1.3 (A)), which could interfere with the estimation of the rotation period of this star.
We applied the wavelet transform method Torrence and Compo (1998) to analyze signals with a dynamic frequency spectrum and compared with the Generalised Lomb-Scargle method Zechmeister and Kürster (2009).
We applied the Morlet wavelet (6th order), which proves to have high temporal and frequency resolution. A sensitivity test on each of the wavelets of the wavelet family indicates that a wavelet function with a higher order value generates much smoother decomposition results than those wavelets analyzed with a lower order Wang and Sassen (2008).
We visualize the local (B) and global wavelet power spectra (C) (see Figure 3.1.3). The wavelet power spectrum plot interprets the energy distribution of the signal in the time-frequency space, while the global wavelet spectrum is generated by time integration of the local map.

[1] https://heasarc.gsfc.nasa.gov/ftools/fv/ :
Fv is a FITS file editor capable of manipulating virtually all aspects of a FITS file and performing basic data analysis of its contents.

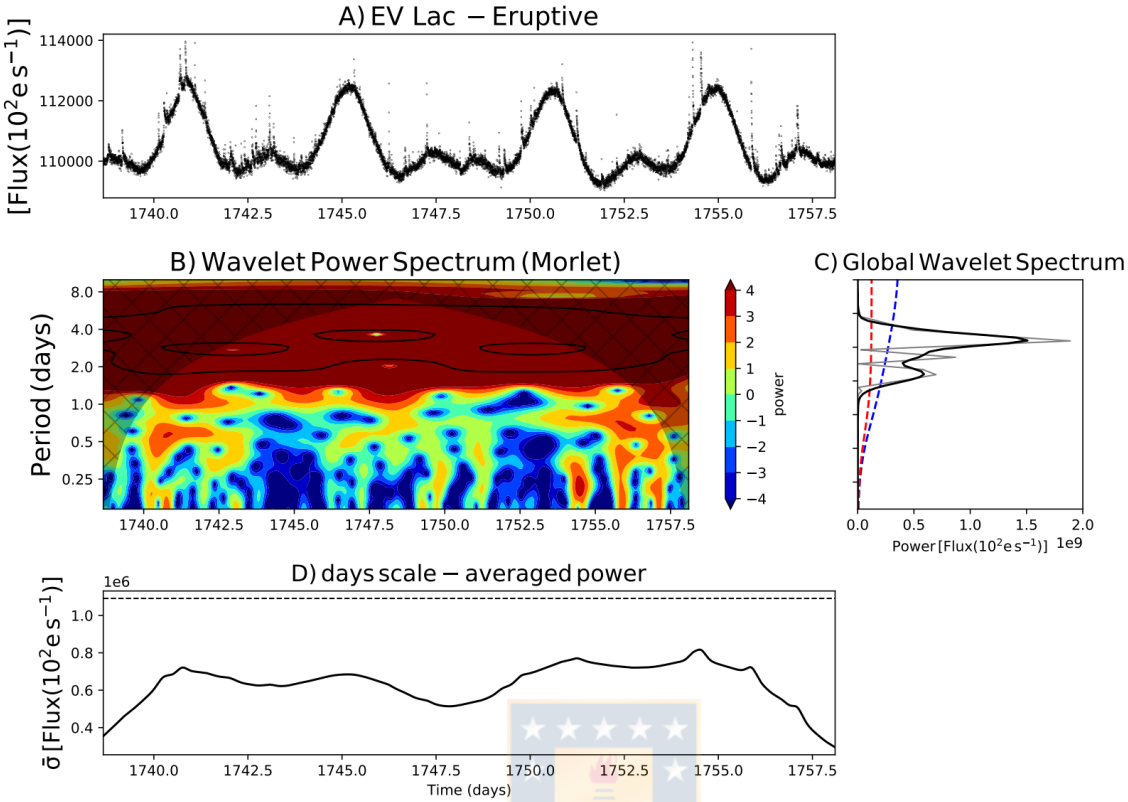

Figure 3.1.3: We developed the Wavelet analysis of the star EV Lac (TIC 154101678): (A) Time series, star light curve (solid black line) in the optical. (B) Normalized wavelet power spectrum using the Morlet-type wavelet ($\omega_0 = 6$) as a function of time and Fourier equivalent wavelet period (in days). Solid black contour lines enclose regions with greater than 95% confidence relative to a random red noise process ($\alpha = 0.77$). The shaded, dashed area indicates the area affected by the cone of influence of the parent wavelet. (C) C) Global wavelet power spectrum (solid black line) and the power spectrum of the inverse of the Fourier transform (solid gray line). The dashed blue line indicates the 95% confidence level and the dashed red line represents the Fourier transform. (D) Wavelet power averaged over the 2-10 days band (solid black line), power trend (solid black line) and 95% confidence level (dashed black line). Plot of own authorship.

We note that the most dominant periodicity of the Global wavelet spectrum (C) is about 4.32 days. We average within a range of 2-10 days (solid black line) due to the expected rotation period according to the literature.

Despite the closeness of the period found with the rotation periods for EV Lac already estimated in the literature, it has been found that this type of analysis has not demonstrated total accuracy because for some sources, the light curves in TESS have gaps in the measured data. This method turns out to be quite successful for continuously measured observational data, since the code

used, as we can see in the figure above, it integrates over a continuous range of time, thus predicting the future values of the light curve present in the data gap.

The Peranso software [2] was used to perform a GLS analysis to determine the rotation period of EV Lac and to obtain the rotation period of this star by means of a wavelet analysis.
In the following figure (see Figure 3.1.4) we notice a period found for the EV Lac star of 4.33 ± 0.13 days. It is quite close and in agreement with the periods found in the literature.

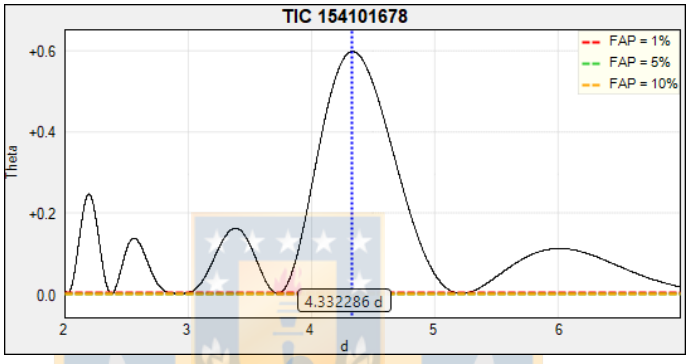

Figure 3.1.4: Period found by the generalized Lomb-Scargle method using Peranso software. The x-axis indicates the time interval during which the period analysis was performed. The y-axis shows the Lomb-Scargle Theta statistic. Image taken from Soto et al. 2022, Boletín 63 Asociación Argentina de Astronomía, accepted.

We note that there are other periods but the most prominent is at its peak at 4.33 days. Performing an inspection of the phase window, we see the less prominent eruptions characteristic of this eruptive star.

[2] https://www.cbabelgium.com/peranso/ : period and light curve analysis software.

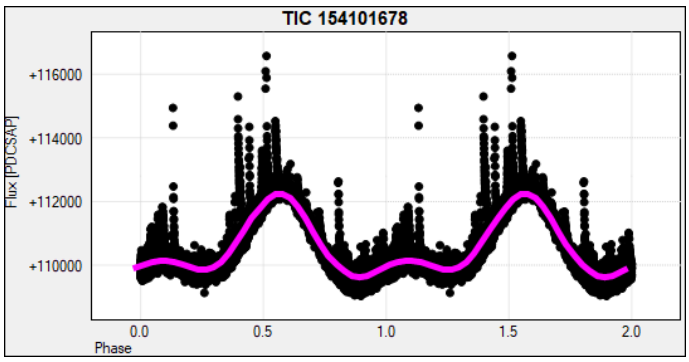

Figure 3.1.5: Phase versus PDCSAP flow window. The pink center line shows the mean curve fit while the vertical dots indicate small, short-lived flares.

We obtain the rotation period, this time using the WWZ method, also using the Peranso software. In it, we found a period of 4.24 days, which is close to the values previously obtained in the literature. close to the values previously obtained in the literature.

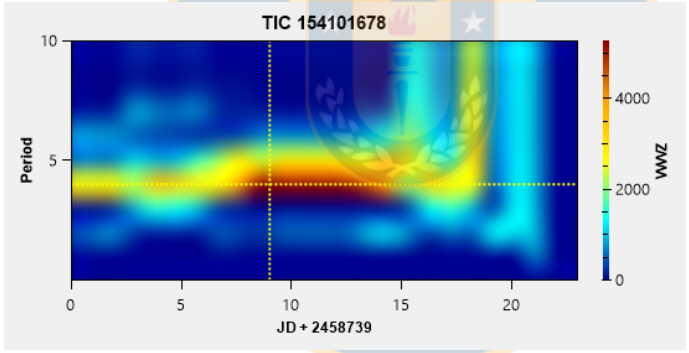

Figure 3.1.6: WWZ transform display. The x-axis represents time, the y-axis represents frequency, and a color (z-axis) is used to plot the WWZ response. The red color shows the most repetitive values indicating a period close to 4.24 days. Image taken from Soto et al. 2022, Boletín 63 Asociación Argentina de Astronomía, accepted.

3.2 Statistical sample

3.2.0.1 Sample of Stars from Boro Saikia et al. (2018)

A total of 53 stars were extracted from Table A.2 of the paper Boro Saikia et al. (2018). The sample of TESS stars belong to spectral types F, G, and K, i.e., stars with an effective temperature range of 7000-3500 K and and have been downloaded directly from the Mikulski Archive for Space Telescopes (MAST) database [3] the PDCSAP FLUX values, which are the single aperture photometry, SAP FLUX, after removing systematic trends.

The rotation period calculations shown in Table A.2 have been reproduced. As with our reference star EV Lac, they were analyzed with Lightkurve, and then a comparison was made between the rotation periods present in the literature with the rotation periods obtained using the GLS, WWZ and ANOVA methods (see Table 3.2.2). As highlighted in one table, for five stars (see Table 3.2.1) we found a concordance with the periods given in the aforementioned paper. However, for stars Boro Saikia et al. (2018) reported rotation periods longer than 10 days, both methods (both GLS and WWZ) indicate shorter periods when applied to TESS data, albeit partially with lower statistical significance. We consider this to be a limitation due to the observational time windows of TESS and could reflect shorter time periods, although it does not correspond to the physical rotation period.

Name	Period found using Wavelet method [d]	Period using GLS [d]	Period from Boro Saikia et al. 2018 [d]	Period from Literature [d]
EV Lac	4.24 ± 0.46	4.33 ± 0.13	-	4.37 (P80)
HD20630	9.00 ± 0.15	9.02 ± 1.05	9.24	9.2 (B17)
HD26913	6.76 ± 0.09	6.84 ± 0.23	7.1	7.15 (SB99)
HD82443	5.32 ± 0.05	5.43 ± 0.14	5.37	5.37 (M99)
HD115043	5.68 ± 0.07	5.67 ± 0.19	5.86	5.86 (H16)
HD115383	3.52 ± 0.02	3.40 ± 0.06	3.33	3.33 (SB99)

Table 3.2.1: Table schematizing the stellar rotation periods calculated according to the Wavelet method and the GLS method, compared with the stellar rotation periods found in the literature. From a total of 53 stars present in Table A.2 of the article Boro Saikia et al. (2018). **References:** (P80)Pettersen (1980), (B17)Brandenburg et al. (2017),(SB99)Saar and Brandenburg (1999), (M99)Messina et al. (1999), (H16)Hempelmann et al. (2016).

[3] https://archive.stsci.edu/

Name	Period using wavelet (WWZ)[d]	Period using GLS [d]	Period using ANOVA [d]	Rotation periods taken from Boro Saikia et al. 2018 [d]	Period from literature [d]
HD3651	10.80 ± 2.48	10.24 ± 0.88	19.23 ± 1.61	44.0	44.0 (SB99) ; 44.5 (F03) ; 48.0 (W11)
HD4628	8.01 ± 0.41	11.97 ± 1.45	13.31 ± 1.61	38.5	39.7 (N84) ; 38.5 (W11)
HD10476	3.20 ± 0.22	3.33 ± 0.12	3.74 ± 0.23	35.2	35.2 (SB99) ; 38.2 (B07) ; 35.2 (W11)
HD16160	12.40 ± 3.01	12.65 ± 1.28	12.80 ± 0.52	48.0	45 (B83) ; 45.0 (N84) ; 48.0 (SB99) ; 48.0 (W11)
HD26965	5.40 ± 0.58	5.14 ± 0.25	20.24 ± 1.46	43.0	43.0 (SB99) ; 43.0 (B07)
HD32147	6.00 ± 0.70	6.19 ± 0.33	6.43 ± 0.29	48.0	47.0 (B96) ; 48.0 (SB99) ; 48.0 (W11)
HD81809	9.00 ± 1.67	8.86 ± 0.66	18.80 ± 1.26	40.2	41 (B96) ; 40.2 (SB99)
HD103095	8.00 ± 1.21	9.89 ± 0.58	12.63 ± 0.56	31.0	31.0 (SB99) ; 31.1 (D92)
HD166620	7.20 ± 1.04	6.95 ± 0.47	4.01 ± 0.09	42.4	42 (B83) ; 42.0 (N84); 43V (B96) ;42.4 (SB99) ; 42.4 (W11)
HD185144	5.33 ±0.53	5.15 ± 0.24	10.56 ± 0.37	29.0	27 (B96) ; 29.0 (SB99)
HD201091	6.40 ± 0.79	2.89 ± 0.08	10.56 ± 0.37	35.7	37.9 (B83) ; 37.9 (N84) ; 35.37 (SB99) ; 35.37 (W11) ; 34.1 (H16) ; 35.4 (B17)
HD219834B	12.40 ± 2.84	12.80 ± 1.36	26.33	43.0	42.0 (N84) ; 43 (SB99) ; 42 (B83) ; 43.0 (B17)
HD101501	5.05 ± 0.49	5.05 ± 0.12	28.94 ± 1.32	16.68	17.1 (N84) ; 17 (B96) ; 16.68 (SB99) ; 16.06 (M17a)
HD20630	9.00 ± 1.58	9.02 ± 0.49	9.10 ± 0.25	9.24	9.4 (B83) ; 9.24 (B07) ; 9.40 (W11) ; 9.2 (B17)
HD10780	10.12 ± 2.19	10.46 ± 0.83	10.96 ± 0.71	21.7	23.0 (W11)
HD18256	2.00 ±0.84	1.49 ± 0.02	7.45 ± 0.17	3.0	3.0 (B96)
HD26913	7.00±0.96	6.82 ± 0.23	6.79 ± 0.11	7.1	7.17 (B83) ; 7.15 (SB99) ; 7.0 (B96) ; 7.15 (W11)
HD26923	5.80 ±0.66	5.94 ± 0.16	5.98 ± 0.11	60.4	60.4 (H16)
HD37394	5.50 ±0.61	5.53 ± 0.14	5.54 ± 0.12	10.74	11 (B96) ; 10.74 (H16) ; 10.78 (M17a)
HD76151	11.08±2.54	11.13 ± 2.10	9.79 ± 0.46	15.0	15.0 (B96) ; 15.0 (SB99) ; 15.2 (M16)
HD78366	4.60 ±0.39	4.87 ± 0.13	9.69 ± 0.18	9.67	9.67 (SB99) ; 9.7 (B17)
HD82443	5.32 ±0.52	5.43 ± 0.14	5.44 ± 0.04	5.37	6.0 (B96) ; 5.41 (W11)
HD82885	9.40 ±1.62	8.85 ± 1.05	8.57 ± 0.45	18.6	18.1 (N84) ; 18.0 (B96) ; 18.6 (W11)
HD100180	4.60 ±0.40	4.79 ± 0.14	14.06 ± 0.45	14.6	14.0 (N84) ; 14.0 (W11)
HD115043	5.68±0.66	5.67 ± 0.19	5.71 ± 0.05	5.86	6.0 (B96) ; 6.0 (W11) ; 5.86 (H16) ; 5.87 (M17a)
HD115383	3.52±0.25	3.40 ± 0.06	3.40 ± 0.02	3.33	3.0 (B96) ; 3.33 (SB99) ; 3.33 (W11)
HD201092	3.00±0.17	3.15 ± 0.09	12.73 ± 0.55	37.84	48 (B83) ; 48.0 (N84) ; 37.84 (SB99) ; 37.84 (W11)
HD20003	10.88 ±2.12	10.82 ± 1.09	11.25 ± 1.37	37.1	38.9 (M08)
HD20619	7.33 ±1.05	7.40 ± 0.58	13.95 ± 0.48	22.3	21.18 (H16)
HD21693	8.60±1.35	8.47 ± 0.57	8.35 ± 1.13	36.3	35.2 (M08)
HD45184	4.60±0.49	4.79 ± 0.18	9.61 ± 0.38	21.4	21.5 (M08)
HD7199	10.12 ±1.84	10.41± 0.70	12.42 ± 0.92	41.0	42.89 (D11)
HD82516	5.50 ±0.62	4.34 ± 0.12	8.55 ± 0.38	36.7	-
HD89454	8.46±1.49	8.47 ± 0.33	8.46 ± 0.10	21.1	-
HD157830	8.46±1.42	8.32 ± 0.82	15.05 ± 1.25	24.3	-
HD361	5.68±0.66	5.57 ± 0.25	16.91 ± 1.24	14.1	-
HD12617	8.92 ±1.96	8.29 ± 0.64	9.02 ± 0.55	30.7	-
HD166724	10.88±2.26	11.10 ± 0.67	11.79 ± 0.66	30.9	30 (M13)
HD21749	2.80 ±0.14	3.71 ± 0.10	11.11 ± 0.24	34.5	34.5 (M08) ; 38.95 (D19) ; 33.6 (G21)
HD154577	9.40 ±1.58	9.56 ± 0.75	10.55 ± 0.63	45.8	-
HD88742	6.85 ±0.97	6.74 ± 0.66	18.80 ± 1.12	11.3	-

Table 3.2.2: Complete table containing the 53 analyzed stars from Table A.2 of Boro Saikia et al. (2018). (Continuation of caption, on next page).

The first column shows the HD name of each star. The following columns show the rotation period obtained for each star by various methods. In the second column we provide the rotation period obtained using the Wavelets method (WWZ). In the third column the rotation period using the GLS method is given, in the fourth column the rotation period for each star using the ANOVA method, in the fifth column, the rotation periods found in Table A.2 of the article Boro Saikia et al. (2018). Sources HD152391, HD160346, HD1835, HD149661, HD190406, HD146233, HD155885, HD155886, HD156026, HD165341A and HD190007 have been discarded due to missing data in TESS in Peranso software. We do not consider the Sun within the sample of 53 stars shown in the table. Those with a dash symbol do not indicate rotation periods in the literature. Finally in the last column are the rotation periods found according to the literature.

References:(SB99)Saar and Brandenburg (1999),(F03)Fischer et al. (2003),(N84)Noyes et al. (1984),(B83)Baliunas et al. (1983),(W11)Wright et al. (2011),(D92)Dobson (1992),(M17a)Mittag et al. (2017),(B07)Böhm-Vitense (2007),(B17)Brandenburg et al. (2017),(M16)Metcalfe et al. (2016),(B96)Baliunas et al. (1996a),(M08)Mamajek and Hillenbrand (2008),(H16)Hempelmann et al. (2016),(D11)Dumusque et al. (2011),(M13)Marmier et al. (2013),(G21)Gan et al. (2021),(D19)Dragomir et al. (2019).

We have used the generalized Lomb Scargle periodogram for the 53 stars with the Peranso software. We created window-ranges for rotation period exploration with this method, i.e., we selected a minimum value of 1 day and a maximum value of 100 days. Based on this, rotation period searches were performed by assigning ranges of values closer to the most prominent peak in the curve. The same procedure was carried out for the WWZ method and ANOVA. The values of the rotation periods are also listed in Table 3.2.2.

In Figures 3.2.1 and 3.2.2 we reproduce the corresponding plots of the activity - rotation period relation from Boro Saikia et al. (2018), showing in red the new periods derived from TESS and in black the periods from their original data. We limit ourselves here to data points consistent with the previous periods.

Figure 3.2.2 recreated the plot present in Boro Saikia et al. (2018) (Figure 8), w_{cyc}/ω versus R_o^{-1}, similar to Fig. 1 of Saar and Brandenburg (1999).
The values of τ_c (convective turnover or correlation time) and R_o were extracted from Table A.2 of Boro Saikia et al. (2018). The values of τ_c and R_o follow the definition given by Noyes et al. (1984), obtained empirically.
Brandenburg et al. (1998) studied the relationship between the ratio of cycle and rotation frequencies w_{cyc}/Ω ($=P_{rot}/P_{cyc}$) and the inverse of the Rossby number $R_o = 2\tau_c\ \Omega = 4\pi\tau_c/P_{rot}$. We have taken this relationship for the derivation of our Y-axis calculations.

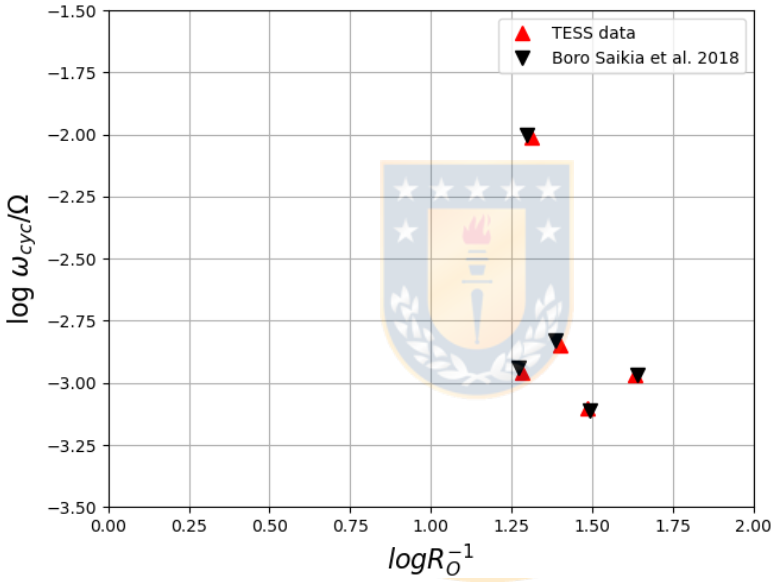

Figure 3.2.1: w_{cyc}/Ω vs. R_o^{-1} for the sample of stars in Table A.2 from Boro Saikia et al. (2018) and for the sample obtained from the agreement between the two method analysed: GLS and WWZ.

The figure above demonstrates the effectiveness of the methods used: Wavelets and GLS, since the periods found coincide with the periods found in the literature. The rotation periods in this study are very close to the stellar rotation periods already found.

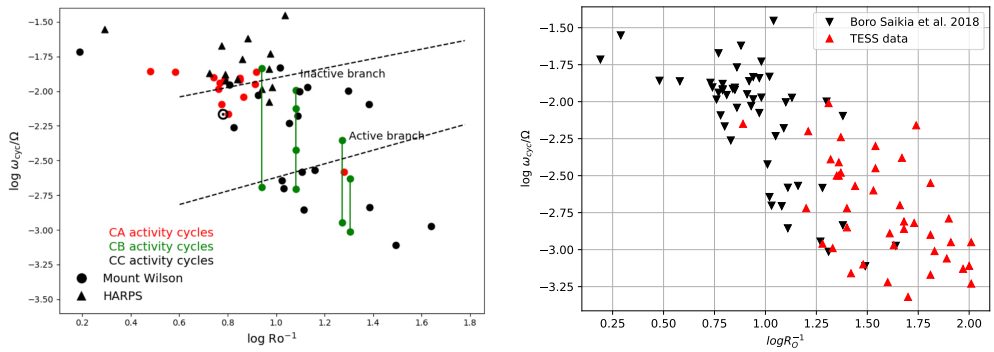

(a) **(b)**

Figure 3.2.2: w_{cyc}/Ω vs. R_o^{-1}. *Left*:(a) Sample stars from Table A.2 of Boro Saikia et al. (2018), where CA means Cool stars with clear well defined solar-like activity cycles, CB to refer to Cool stars with multiple cycles and CC to Cool stars with probable activity cycles. *Right*:(b) Reproduction of the stellar rotation periods of the sample of stars in Table A.2.

In Figure 3.2.2, (a) The authors studied the active and inactive branches in the plane of the rotation-activity-cycle period, according to the Mount Wilson program Wilson (1968). The stars were measured for their magnetic activity and classified into an active branch, intermediate magnetic activity branch and an inactive branch, as we can see in the diagonal dotted lines. It shows that stars with clear activity cycles (CA) including our Sun are all on the inactive branch, except for one star which is on the active branch Saar and Brandenburg (1999). In 3.2.2 (a) the rotation periods taken by the authors were rotation periods from periodograms analysis of Ca II chromospheric activity records of lower main sequence stars obtained at the Mount Wilson Observatory (MWO) (Horne and Baliunas (1986); Baliunas et al. (1995)). For more details see Saar and Brandenburg (1999) and Boro Saikia et al. (2018).

On the other hand, in Figure 3.2.2 (b), we highlight the rotation periods obtained in this study. In it, we observed an anti-correlation of the data. The rotation periods of the stars are located at low P_{rot}/P_{cyc} and high $logR_o$ ratios.

This difference could be due to observational gaps in the data acquisition, present in the TESS light curves. Despite this difference in the obtained rotation period, the errors associated with these rotation periods are less than 1% in most cases, as shown in Table 3.2.2 indicating the performance of both methods for the determination of stellar rotation periods.

In the following figure, Figure 3.2.3, we reproduce Figure 9 of the article Boro Saikia et al. (2018). We plot the activity-cycle period as a function of the rotation period similar to Figure 1 in Böhm-Vitense (2007).
Figure 3.2.3 shows those stars that are in agreement with the rotation periods found in the literature.
In red we show the new rotation periods obtained for the sample in In red we show the rotation periods obtained in this study with TESS data, for the sample in Table A.2. These new rotation periods are in a range between 0 and 10 days (see Figure 3.2.4). The P_{cyc} values were taken directly from Table A.2 Boro Saikia et al. (2018) as well as the rotation periods indicated in black.

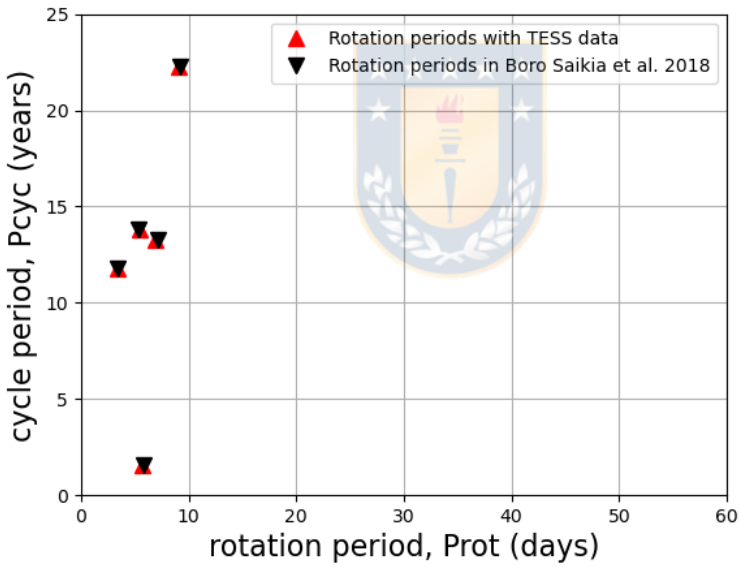

Figure 3.2.3: Activity-cycle period in years as a function of rotation period in days for the sample of stars in Table A.2 from Boro Saikia et al. (2018) and for the sample obtained from TESS data showing agreement between the two methods analyzed: GLS and WWZ.

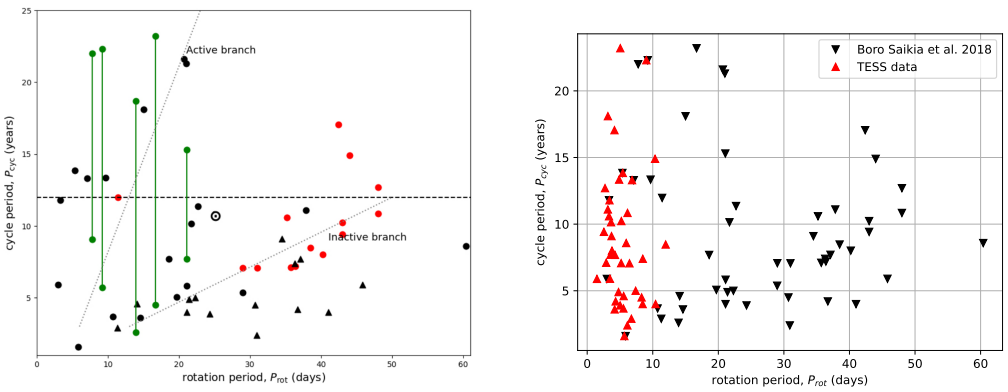

(a) **(b)**

Figure 3.2.4: P_{rot} versus P_{cyc}. *Left*: (a) Figure 9 of the Boro Saikia et al. (2018) article is shown, for a sample of 53 stars with the same activity cycles, i.e., CA, CB and CC. *Right*: (b) Recreation of the figure on the left, with the new rotation periods found with TESS data.

Figure 3.2.4 (a) shows a graph of rotation period versus cyclic period extracted from Boro Saikia et al. (2018). In it, the authors again see how the stars behave according to their calculations, in the active and inactive branches. Figure 3.2.4 (b) corresponds to a reproduction of figure (a) with stellar rotation periods analyzed with TESS data shown in Table 3.2.2. The cyclic periods were extracted directly from Table A.2 of Boro Saikia et al. (2018).
We can observe that these periods are concentrated in a range of less than 15 days.

Histograms were made of the rotation periods obtained and a normal distribution was applied in order to obtain a better way of visualizing the results. The distribution function of the normal distribution is defined as follows,

$$\Phi_{\mu,\sigma^2(x)} = \int_{-\infty}^{x} \varphi_{\mu,\sigma^2(x)}(u)du \tag{3.2.1}$$

$$= \frac{1}{\sigma\sqrt{2\pi}} \int_{-\infty}^{x} e^{-\frac{(u-mu)^2}{2\sigma^2}} du, \quad x \in R\,,$$

where
μ corresponds to the mean,
σ is the standard deviation,
σ^2 is the variance,

φ represents the probability density function.

WWZ periods - Boro Saikia et al. (2018)	
Distribution	Normal
μ	7.1778
σ	2.71633
Null hypothesis	0.1653
Chi-squared distribution	5.0902

Table 3.2.3: Table of statistical data resulting from the rotation periods obtained with TESS using wavelets (WWZ).

The mean distribution of the star sample by the wavelet method fits a normal distribution. The rotation periods determined with the TESS data show a higher frequency of rotation periods between 6 and 8 days, with a σ of 2.71633. The overall sample using this method has a μ of 7.17.

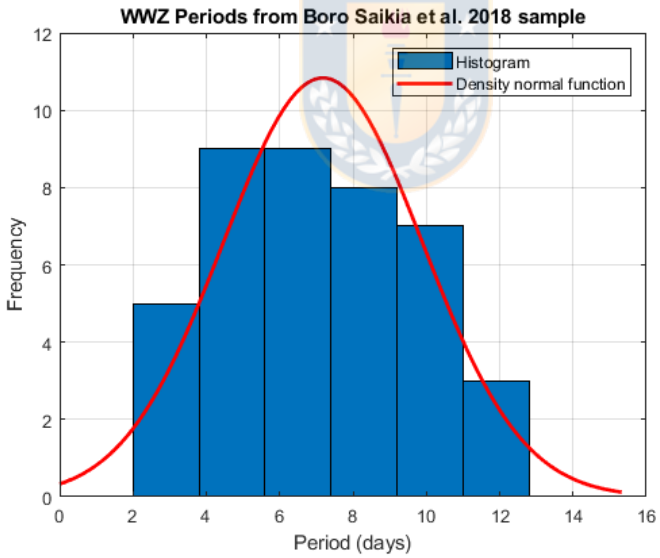

Figure 3.2.5: Histogram from TESS data for rotation periods obtained with wavelets (WWZ).

The errors associated with the wavelet method (WWZ) are centered between 0.5 and 1, with a σ of 0.54. Less frequent rotation periods of about 2 to 3 %. This tells us that most of the rotation periods determined are reliable, because they will tend to be values closer to the actual rotation period of each star.
The data fit the distribution used very well, taking into account only the positive values of the errors associated with the period.

WWZ errors - Boro Saikia et al. (2018)	
Distribution	Generalized Extreme Value distribution
k	0.18742
μ	0.712699
σ	0.547843
Chi-squared distribution	5.0434

Table 3.2.4: Table of statistical data resulting from the errors associated with the rotation periods obtained with TESS using wavelets (WWZ).

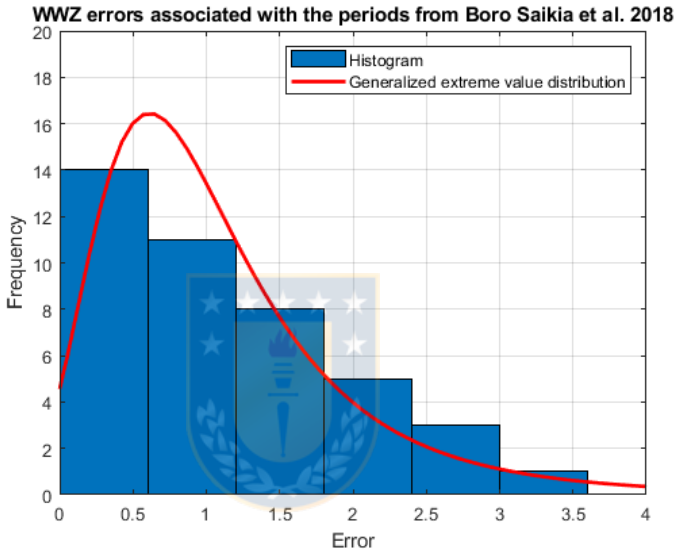

Figure 3.2.6: Histogram of the TESS data for the errors associated with the rotational periods obtained with wavelets (WWZ).

GLS periods - Boro Saikia et al. (2018)	
Distribution	Normal
μ	7.21098
σ	2.94307
Null hypothesis	0.0584
Chi-squared distribution	7.4678

Table 3.2.5: Table of statistical data resulting from the rotation periods obtained with TESS using Generalised Lomb-Sacrgle(GLS) method.

Additionally, the resulting histogram for the rotation periods of the star sample using TESS data with the GLS method indicates a mean of the periods between 6 and 8 days with a $\sigma = 2.94$ approximately. The data indicate a good fit to the normal distribution used. The rotation periods with the highest frequency are

found to be around 6 days, and the rotation periods found to show the lowest frequency are around 2 days.

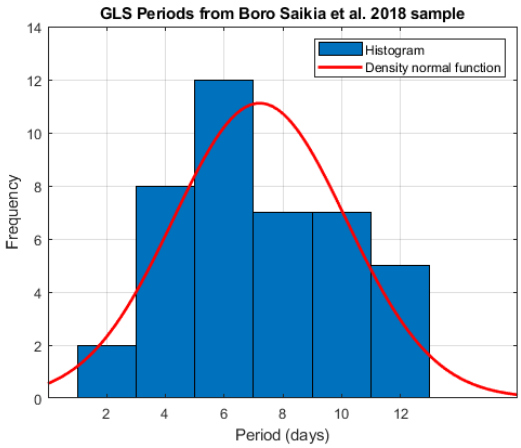

Figure 3.2.7: Histogram from TESS data for rotation periods obtained with Generalised Lomb Scargle(GLS).

GLS errors - Boro Saikia et al. (2018)	
Distribution	Generalized Extreme Value distribution
k	0.566315
μ	0.238379
σ	0.21819
Chi-squared distribution	3.875

Table 3.2.6: Table of statistical data resulting from the errors associated with the rotation periods obtained with TESS using Generalised Lomb Scargle(GLS).

And the histogram for the errors associated with this method indicates values between 0 and 1, i.e., not only the errors are lower, but also the GLS method could be more efficient than the Wavelets method in terms of the errors obtained. The distribution function indicates a good fit to the data. The associated errors indicate lower frequencies for values around 2%.

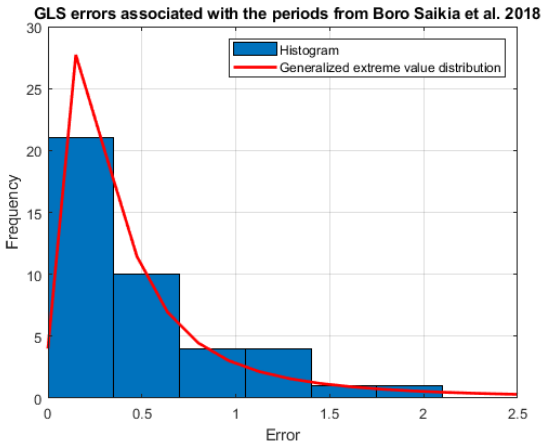

Figure 3.2.8: Histogram of the TESS data for the errors associated with the rotational periods obtained with Generalised Lomb Scargle(GLS).

3.2.0.2 Sample of stars from Messina et al. (2022)

TESS data have been downloaded from the Mikulski Archive for Space Telescopes (MAST) for 45 of the 168 stars in sectors (14-16) between July 18, 2019, and July 4, 2020. The light curves for each star have been manually downloaded using the SPOC pipeline. After that, we processed the data for each star using Lightkurve and extracted light curves from the data through a pixel file, using a custom aperture mask in order to remove background contaminants in each star.
Finally, we used the Peranso software (Light Curve and Period Analysis Software) where a GLS and WWZ analysis was performed.
As input data, we have used the sample of stars present in Messina et al. (2022), which is composed of 218 stars from the list of stars published by Tang et al. (2019), with 168 measured rotation periods by the authors (those who used GLS, CLEAN and ACF). From these 168 values, we found rotation periods for 45 stars and not for all of them due to the limitations imposed by the software used.
Like the authors, we used the generalized Lomb Scargle method. The FAP was implemented according to the equation given by Horne and Baliunas (1986).
We calculated the error associated with the rotation period, following the mechanism provided by Lamm et al. (2004).
As analyzed by Messina et al. (2022), a total of 17 periodic stars possess a visual companion only detected with Gaia DR2 but difficult to identify with TESS photometric data with a separation of $\rho \lesssim 10$". Regarding the stars analyzed under this study, only two stars, the binary system: TIC 1102311836 and TIC 1102311837 (148* and 149*, see Table 3.2.3) presented a secondary period in Gaia DR2. Single periods of 4.65 ± 0.11 days and 4.66 ± 0.14 days, respectively, were found with the GLS method, compared to 0.663 ± 0.006 days and 4.64 ± 0.45 days for the authors.

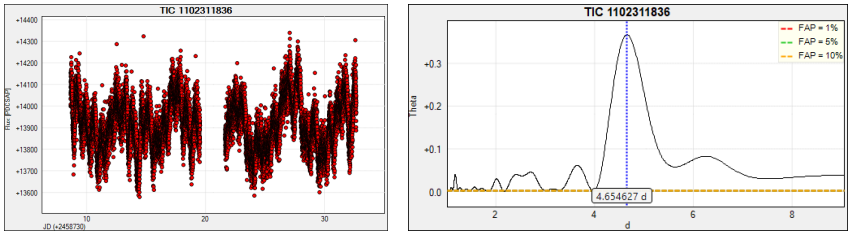

(a) **(b)**

Figure 3.2.9: TIC 1102311836 star. *Left*: (a) Light curve. *Right*: (b) Periodogram using GLS.

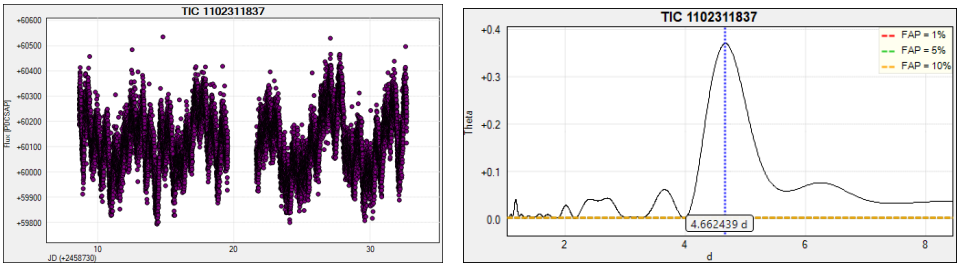

(a) **(b)**

Figure 3.2.10: TIC 1102311837 star. *Left*: (a) Light curve. *Right*: (b) Periodogram using GLS.

The sample of analyzed stars is shown below,

Sequ. #	TIC number	TESS Sector	Period of Messina et al. 2022 [d]	Period using GLS [d]	Period using wavelet (WWZ)[d]
8	0155856633	15/16/22	5.08 ± 0.16	2.75 ± 0.05	2.8 ± 0.15
21	0459221499	15/16/22	0.373 ± 0.003	0.373 ± 0.001	0.496 ± 0.002
39	0332312964	15/16/22/23	4.98 ± 0.52 / 0.363 ± 0.004	4.56 ± 0.11	4.6 ± 0.41
42	0141819826	16/15/22/23	7.1 ± 1.2	6.90 ± 0.65	6.88 ± 0.91
45	0311001628	16	0.602 ± 0.008	0.604 ± 0.007	0.604 ± 0.007
49	0310338842	15/16/22/23	7.8 ± 1.2	5.12 ± 0.27	5.08 ± 0.25
51	0141861147	15/16/22/23	1.38 ± 0.04	1.38 ± 0.01	1.4 ± 0.02
54	0141863294	16/22	8.1 ± 1.8	3.82 ± 0.16	3.96 ± 0.32
71	0233437236	15/16/22/23	6.9 ± 1.0	5.75 ± 0.28	5.68 ± 0.62
74	0198154161	16	9.3 ± 1.9	5.37 ± 0.37	5.32 ± 0.57
77	0010728867	16/22/23	7.6 ± 1.2	7.71 ± 0.74	7.66 ± 1.19
88	0310379752	22	0.561 ± 0.487	0.563 ± 0.006	0.567 ± 0.0065
91★[a]	1001276338	15/16/22/23	6.21 ± 0.80	6.22 ± 0.21	6.22 ± 0.74
93	0445859773	15/16	1.28 ± 0.03	1.24 ± 0.01	1.58 ± 0.05
95	0313322899	22	0.546 ± 0.006	0.546 ± 0.001	0.56 ± 0.006
102	0166089535	15/16/21/22	3.14 ± 0.05	1.54 ± 0.01	1.55 ± 0.05
105	0459246945	15/16/22/23	4.27 ± 0.38	4.59 ± 0.17	4.6 ± 0.41
116	0313338124	15/16/23	2.73 ± 0.15	1.36 ± 0.01	1.4 ± 0.04
122	0298162216	16/15/22/23	9.11 ± 0.58	5.37 ± 0.14	5.32 ± 0.52
124	0298163080	15/22/23	4.93 ± 0.50	4.41 ± 0.09	4.6 ± 0.41
126	0159613447	15/16/21/22/23	6.29 ± 0.82	6.33 ± 0.38	6.4 ± 0.79
127	0158462948	15/16/22/23	4.98 ± 0.51	5.07 ± 0.14	4.96 ± 0.47
133	0159631183	15/16/22/23	0.89 ± 0.01	0.89 ± 0.01	0.8 ± 0.01
135	0159636302	15/16/22/23	1.09 ± 0.02	1.09 ± 0.01	1.1 ± 0.01
139	0158541117	22/15	6.65 ± 0.88	3.71 ± 0.18	3.88 ± 0.29
143★	0161024760	22/16/23	6.48 ± 0.83	3.03 ± 0.08	3.16 ± 0.20
145	0158579468	15	7.9 ± 1.3	8.72 ± 0.54	8.6 ± 0.15
146	0161029191	16/22/23	5.34 ± 0.63	5.39 ± 0.17	5.32 ± 0.57
148★	1102311836	15/16/22/23	0.663 ± 0.006	4.65 ± 0.11	4.3 ± 0.35
149★	1102311837	15/16/22/23	4.64 ± 0.45	4.66 ± 0.14	4.6 ± 0.41
152	0462572935	16	8.8 ± 1.4	10.84 ±0.80	10.88 ± 2.27
153	0137832480	15/16/22/23	3.57 ± 0.26	3.28 ± 0.18	3.16 ± 0.01
155	0137834492	16/22/23	0.1050 ± 0.0002	0.025 ± 0.00002	0.025 ± 0.0000014
158	0137834559	15/16/22/23	5.37 ± 0.60	5.12 ± 0.15	4.96 ± 0.47
159★[a]	0202425640	15/16/22/23	9.23 ± 0.70	5.50 ± 0.28	5.48 ± 0.61
164	0232541198	14/15/16/21/23	5.21 ± 0.54	5.31 ± 0.16	5.32 ± 0.53
165	0165628355	15/23	9.21 ± 0.80	5.51 ± 0.17	5.68 ± 0.59
182	0165719269	16	7.3 ± 1.2	7.84 ± 0.45	7.84 ± 1.25
188	0202510436	15/16/22/23	7.5 ± 1.2	4.82 ± 0.20	4.96 ± 0.47
193	0159769293	16/23	7.4 ± 1.2	4.85 ± 0.17	4.96 ± 0.50
207	0159871737	16/23/24	4.58 ± 0.46	4.64 ± 0.19	4.6 ± 0.43
209	0159873822	16/23	7.5 ± 1.2	8.17 ± 0.52	8.20 ± 1.36
211	0159879031	16/23/24	4.28 ± 0.40	4.32 ± 0.10	4.24 ± 0.36
213	0159922985	23/16/24/25	5.20 ± 0.54	2.45 ± 0.04	2.44 ± 0.12
214	0219479795	23	7.0 ± 1.0	9.7 ± 0.73	10.12 ± 1.91

Table 3.2.7: Reproduction of the star sample of Messina et al. (2022). In the first column we note the analyzed star number of the sample, in the second column its name in the TESS project, in the third column the TESS sector of each star, in the fourth column the stellar rotation period found by Messina et al. (2022), finally in the fifth and sixth columns the rotation periods in determined under the GLS and WWZ method respectively.

WWZ periods - Messina et al. (2022)	
Distribution	Normal
μ	4.37471
σ	2.60489
Null hypothesis	0.0229
Chi-squared distribution	9.5424

Table 3.2.8: Table of statistical data resulting from the rotation periods obtained with TESS using wavelets (WWZ).

The following histogram has been obtained using the TESS data, in it we can see the fit of the normal distribution runs through the data, with more frequent rotation periods, in a range between 4 and 6 days, this tells us that a large part of the stars rotate with a period of 4.37 days. The sample indicates a $\sigma = 2.60$ and rotation periods bounded between 0 and 12 days.

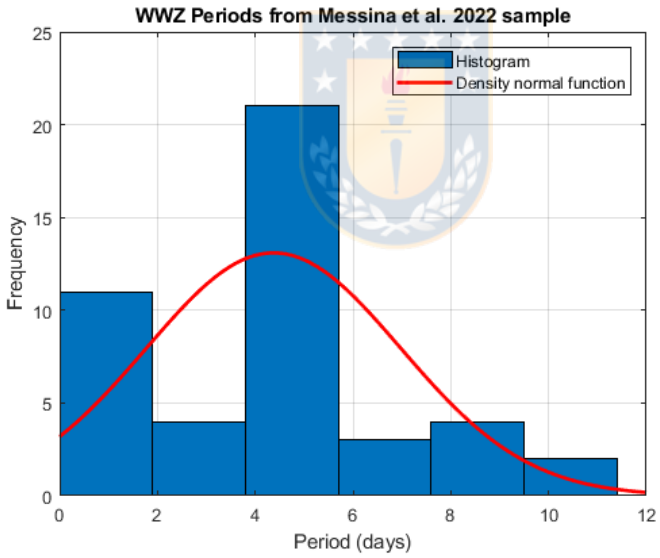

Figure 3.2.11: Histogram from TESS data for rotation periods obtained with wavelets (WWZ).

WWZ errors - Messina et al. (2022)	
Distribution	Generalized Extreme Value distribution
k	0.402173
μ	0.206213
σ	0.24429
Chi-squared distribution	4.5358

Table 3.2.9: Table of statistical data resulting from the errors associated with the rotation periods obtained with TESS using wavelets (WWZ).

While the histogram of the errors associated with the wavelet method, with values between 0 and 0.5%, being less frequent the errors with values of 2% accuracy. This is why the errors indicate high confidence due to low uncertainty values.

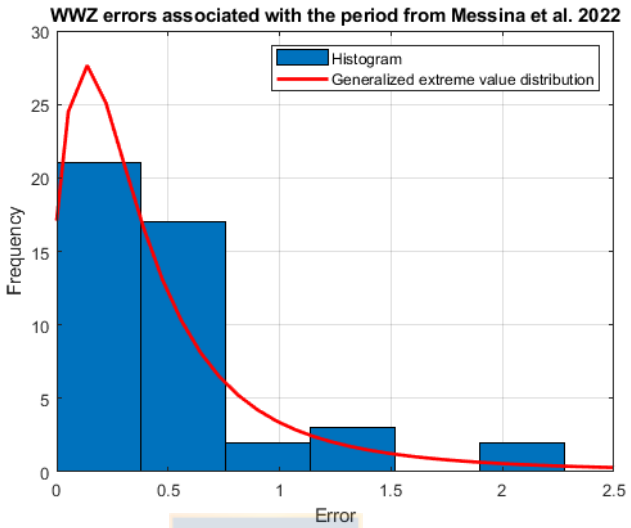

Figure 3.2.12: Histogram of the TESS data for the errors associated with the rotational periods obtained with wavelets (WWZ).

GLS periods - Messina et al. (2022)	
Distribution	Normal
μ	4.35758
σ	2.60299
Null hypothesis	0.0061
Chi-squared distribution	12.4213

Table 3.2.10: Table of statistical data resulting from the rotation periods obtained with TESS using Generalised Lomb-Sacrgle(GLS) method.

We also show the histogram obtained from the TESS data using the GLS method for the Messina et al. method for the Messina et al. 2022 sample. In the histogram, rotation periods of higher frequency are observed between 4 and 6 days with a frequency are observed between 4 and 6 days, with a σ of about 2.60. The normal distribution indicates a fit, crossing the data and indicating a more frequent rotation period in the sample, of 4.35 days.

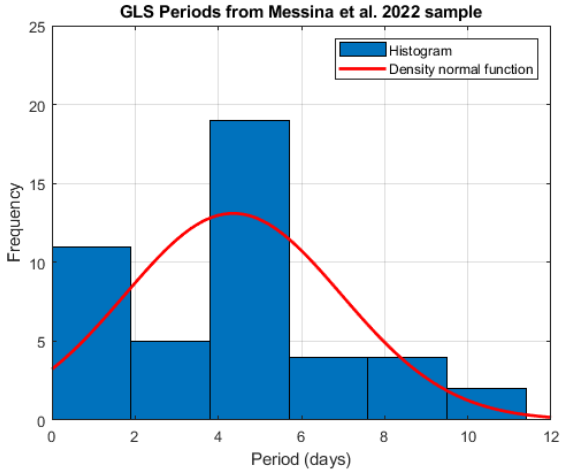

Figure 3.2.13: Histogram from TESS data for rotation periods obtained with Generalised Lomb Scargle(GLS).

GLS errors - Messina et al. (2022)	
Distribution	Generalized Extreme Value distribution
k	0.515489
μ	0.0825341
σ	0.101191
Chi-squared distribution	1.7209

Table 3.2.11: Table of statistical data resulting from the errors associated with the rotation periods obtained with TESS using Generalised Lomb Scargle(GLS).

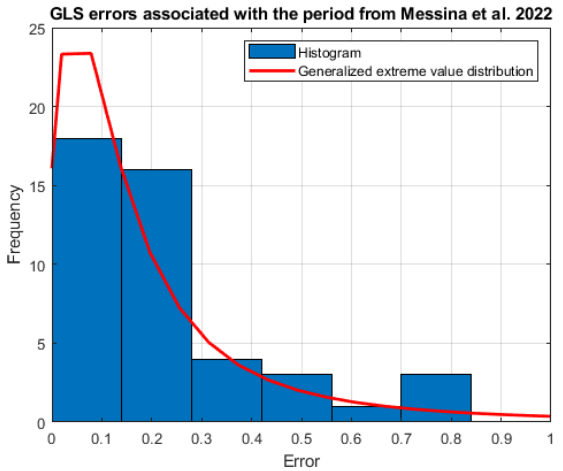

Figure 3.2.14: Histogram of the TESS data for the errors associated with the rotational periods obtained with Generalised Lomb Scargle(GLS).

Finally, we have the histogram of the errors associated with the GLS method. The

error values are in the range between 0 and 0.9%, the most frequent errors being between 0 and 0.2%, with less frequent errors of values greater than 0.5. This indicates and reinforces again the effectiveness of the Generalized Lomb Scargle method on a Wavelets analysis, due to the low errors obtained associated to the calculated errors.

Chapter 4

Summary and Discussion

In this section, we show the discussion of the results and future plans of this study.

In Chapter 2, we present the Transiting Exoplanet Survey Satellite (TESS), from which the data are extracted. We present the Lightkurve program and the different methods used to determine the rotation period. The light curves from each star, removing background contaminants and outliers present in the light curves.

Two samples of stars of spectral types F, G, K are analyzed. The first sample of stars, coming from the article Boro Saikia et al. (2018) of 53 cool stars, product of a combination of spectra from the HARPS archive and Mount Wilson data; and the second sample of stars extracted from Messina et al. (2022), corresponds to a list of 168 stars coming from Tang et al. (2019), data collected by TESS in the second year of its mission (Sectors 14-26).

Chapter 3 is devoted to the work of analyzing the accuracy of the two statistical methods frequency analysis methods: Generalized Lomb Scargle and Wavelets (Wavelet Z-transform) and an additional method called ANOVA provided results that differed significantly from the previous methods.

Thorough visual searches of periodograms were performed with both methods, i.e., GLS and Wavelets, considering the most prominent value of each curve as the rotation period. Wavelet plots (WWZ) were analyzed for a range of frequencies and time, for each color-delivered response.

A brief analysis is made for the calculation of the stellar rotation period for the eruptive variable star EV Lac, where the rotation periods found in the literature are compared with the rotation periods obtained in this study by means of GLS and Wavelets, reaching a great closeness in the results.
On the other hand, two samples of stars were analyzed.
The first sample comes from Boro Saikia et al. 2018 (Table A.2), which for a total of 53 stars the rotation period was determined for 41 stars with the GLS and Wavelets methods. The Sun was not considered in the calculations, and some cases such as HD152391, HD160346, HD1835, HD149661, HD190406, HD146233, HD155885, HD155886, HD156026, HD165341A and HD190007 (listed in Table A.2 of Boro Saikia et al. (2018)) were discarded due to the limitation imposed by the Peranso software such as difficulties in searching for TESS data, resulting in missing data. The accuracy of the periods determined in this study for 5 stars out of the 41 stars analyzed is distinguished, with a high closeness between the periods found in the literature.
Possible reasons for the remaining stars to have shorter periods using TESS data compared to the periods determined by various authors are discussed. One possible cause could be related to data gaps in the light curves extracted from TESS. In spite of this, the errors associated with each method were analyzed, where GLS stands out over Wavelets due to the lower error values obtained with this method, demonstrating that the methods used for this sample of stars are well executed.

We also analyzed of a second sample of cool stars, extracted from Messina et al. (2022). Star sample composed of 168 stars, of which the rotation period was successfully determined for 45 stars. The main cause of the number of stars analyzed is attributed to the limitations imposed by the software used, such as the non-finding of the TESS mission/project data, among others.
Similarly, the stellar rotation periods for these stars were determined with the GLS and Wavelets methods, and the results were compared with the rotation periods determined in Messina et al. (2022). Good agreement was reached for most of the rotation periods analyzed and similarly, low associated errors were found for both methods used. Again, with the results obtained, GLS stood out over Wavelets due to the lower associated errors, reaching a high accuracy with

the authors.

As future work, it is proposed to achieve an analysis for a larger sample of stars and to incorporate a survey of the magnetic cycles (cyclic period) with both methods used.

The study of the determination of stellar rotation periods is important to be highlighted as it could be debated in terms of the values determined in the literature. The rotation period is often associated with calculations of different parameters that incorporate these values. For example, the estimation of stellar age, the study of stellar magnetism, among others.

The study of stellar magnetism leads to an understanding of associated stellar phenomena. Many of the objects that exhibit magnetic fields have evidence suggesting that the region of field generation is in a turbulent state, giving rise to a theory that explains the amplification of the magnetic field caused by the motion of a conducting fluid. These present motions are dominated by rotation, a key ingredient in dynamo theory. While the full set of questions as to how these phenomena are generated have not yet been fully answered, studying them may bring us closer and closer to all the answers.

Bibliography

Abdul-Aziz, H., Abranin, E. P., Alekseev, I. Y., Avgoloupis, S., Bazelyan, L. L., Beskin, G. M., Brazhenko, A. I., Chalenko, N. N., Cutispoto, G., Fuensalida, J. J., Gershberg, R. E., Kidger, M. R., Leto, G., Malkov, Y. . F., Mavridis, L. N., Pagano, I., Panferova, I. P., Rodono, M., Seiradakis, J. H., Sergeev, S. G., Spencer, R. E., Shakhovskaya, N. I., and Shakhovskoy, D. N. (1995). Coordinated observations of the red dwarf flare star EV Lacertae in 1992. *A&A supplement*, 114:509.

Aller, A., Lillo-Box, J., Jones, D., Miranda, L. F., and Barceló Forteza, S. (2020). Planetary nebulae seen with TESS: Discovery of new binary central star candidates from Cycle 1. *A&A*, 635:A128.

Ambruster, C. W., Pettersen, B. R., Hawley, S., Coleman, L. A., and Sandmann, W. H. (1986). An episode of mass expulsion from the M-dwarf flare star EV Latertae ? In Rolfe, E. J. and Wilson, R., editors, *New Insights in Astrophysics. Eight Years of UV Astronomy with IUE*, volume 263 of *ESA Special Publication*, pages 137–140.

Baliunas, S., Sokoloff, D., and Soon, W. (1996a). Magnetic Field and Rotation in Lower Main-Sequence Stars: an Empirical Time-dependent Magnetic Bode's Relation? , 457:L99.

Baliunas, S. and Soon, W. (1995). Are Variations in the Length of the Activity Cycle Related to Changes in Brightness in Solar-Type Stars? *Ap.J*, 450:896.

Baliunas, S. L., Donahue, R. A., Soon, W. H., Horne, J. H., Frazer, J., Woodard-Eklund, L., Bradford, M., Rao, L. M., Wilson, O. C., Zhang, Q., Bennett, W., Briggs, J., Carroll, S. M., Duncan, D. K., Figueroa, D., Lanning, H. H., Misch, T., Mueller, J., Noyes, R. W., Poppe, D., Porter, A. C., Robinson, C. R., Russell, J., Shelton, J. C., Soyumer, T., Vaughan, A. H., and Whitney, J. H. (1995). Chromospheric Variations in Main-Sequence Stars. II. *Ap.J*, 438:269.

Baliunas, S. L., Hartmann, L., Noyes, R. W., Vaughan, H., Preston, G. W., Frazer, J., Lanning, H., Middelkoop, F., and Mihalas, D. (1983). Stellar rotation in lower main-sequence stars measured from time variations in H and K emission-line fluxes. II. Detailed analysis of the 1980 observing season data. , 275:752–772.

Baliunas, S. L., Nesme-Ribes, E., Sokoloff, D., and Soon, W. H. (1996b). A Dynamo Interpretation of Stellar Activity Cycles. *Ap.J*, 460:848.

Barning, F. J. M. (1963). The numerical analysis of the light-curve of 12 Lacertae. *Bulletin Astronomical Institute of the Netherlands*, 17:22.

Berdyugina, S. V. (2005). Starspots: A Key to the Stellar Dynamo. *Living Reviews in Solar Physics*, 2(1):8.

Böhm-Vitense, E. (2007). Chromospheric Activity in G and K Main-Sequence Stars, and What It Tells Us about Stellar Dynamos. *Ap.J*, 657(1):486–493.

Bohm-Vitense, E. (2007). Chromospheric activity in g and k main-sequence stars, and what it tells us about stellar dynamos. *The Astrophysical Journal*, 657(1):486–493.

Boro Saikia, S., Marvin, C. J., Jeffers, S. V., Reiners, A., Cameron, R., Marsden, S. C., Petit, P., Warnecke, J., and Yadav, A. P. (2018). Chromospheric activity catalogue of 4454 cool stars. Questioning the active branch of stellar activity cycles. *A&A*, 616:A108.

Borucki, W. J. (2017). Kepler: A Brief Discussion of the Mission and Exoplanet Results. *Proceedings of the American Philosophical Society*, 161(1):38–65.

Brandenburg, A., Mathur, S., and Metcalfe, T. S. (2017). Evolution of Co-existing Long and Short Period Stellar Activity Cycles. , 845(1):79.

Brandenburg, A., Saar, S. H., and Turpin, C. R. (1998). Time Evolution of the Magnetic Activity Cycle Period. *Astrophysical Journal, Letters*, 498(1):L51–L54.

Bravo, J. P., Roque, S., Estrela, R., Leão, I. C., and De Medeiros, J. R. (2014). Wavelets: a powerful tool for studying rotation, activity, and pulsation in Kepler and CoRoT stellar light curves. *A&A*, 568:A34.

Burrus C., Gopinath R., G. H. (1998). Introduction to Wavelets and Wavelet Transform—A Primer. *Recherche, 67*.

Charbonneau, P. (2010). Dynamo Models of the Solar Cycle. *Living Reviews in Solar Physics*, 7(1):3.

Cincunegui, C., Díaz, R. F., and Mauas, P. J. D. (2007). Hα and the Ca II H and K lines as activity proxies for late-type stars. *A&A*, 469(1):309–317.

Cowling, T. G. (1934). The magnetic field of sunspots. *Monthly Notices of the Royal Astronomical Society*, 94:39–49.

Cumming, A., Butler, R. P., Marcy, G. W., Vogt, S. S., Wright, J. T., and Fischer, D. A. (2008). The Keck Planet Search: Detectability and the Minimum Mass and Orbital Period Distribution of Extrasolar Planets. *Publications of the ASP*, 120(867):531.

de Wijn, A. G., Stenflo, J. O., Solanki, S. K., and Tsuneta, S. (2009). Small-Scale Solar Magnetic Fields. *Space Science Reviews*, 144(1-4):275–315.

Dobson, A. K. (1992). Short Time-Scale Variations in CA II H+K Observations. In Giampapa, M. S. and Bookbinder, J. A., editors, *Cool Stars, Stellar Systems,*

and the Sun, volume 26 of *Astronomical Society of the Pacific Conference Series*, page 297.

Doyle, J. G. (1987). *A&A*, 177:201.

Dragomir, D., Teske, J., Günther, M. N., Ségransan, D., Burt, J. A., Huang, C. X., Vanderburg, A., Matthews, E., Dumusque, X., Stassun, K. G., Pepper, J., Ricker, G. R., Vanderspek, R., Latham, D. W., Seager, S., Winn, J. N., Jenkins, J. M., Beatty, T., Bouchy, F., Brown, T. M., Butler, R. P., Ciardi, D. R., Crane, J. D., Eastman, J. D., Fossati, L., Francis, J., Fulton, B. J., Gaudi, B. S., Goeke, R. F., James, D., Klaus, T. C., Kuhn, R. B., Lovis, C., Lund, M. B., McDermott, S., Paegert, M., Pepe, F., Rodriguez, J. E., Sha, L., Shectman, S. A., Shporer, A., Siverd, R. J., Garcia Soto, A., Stevens, D. J., Twicken, J. D., Udry, S., Villanueva, Steven, J., Wang, S. X., Wohler, B., Yao, X., and Zhan, Z. (2019). TESS Delivers Its First Earth-sized Planet and a Warm Sub-Neptune. , 875(2):L7.

Dumusque, X., Lovis, C., Ségransan, D., Mayor, M., Udry, S., Benz, W., Bouchy, F., Lo Curto, G., Mordasini, C., Pepe, F., Queloz, D., Santos, N. C., and Naef, D. (2011). The HARPS search for southern extra-solar planets. XXX. Planetary systems around stars with solar-like magnetic cycles and short-term activity variation. , 535:A55.

Duncan, D. K., Vaughan, A. H., Wilson, O. C., Preston, G. W., Frazer, J., Lanning, H., Misch, A., Mueller, J., Soyumer, D., Woodard, L., Baliunas, S. L., Noyes, R. W., Hartmann, L. W., Porter, A., Zwaan, C., Middelkoop, F., Rutten, R. G. M., and Mihalas, D. (1991). CA II H and K Measurements Made at Mount Wilson Observatory, 1966–1983. *Ap.J supplement*, 76:383.

Eberhard, G. and Schwarzschild, K. (1913). On the reversal of the calcium lines H and K in stellar spectra. *Ap.J*, 38:292–295.

Eddy, J. A. (1976). The Maunder Minimum. *Science*, 192(4245):1189–1202.

Favata, F., Micela, G., and Reale, F. (2000). The corona of the dMe flare star AD Leo. *A&A*, 354:1021–1035.

Fischer, D. A., Butler, R. P., Marcy, G. W., Vogt, S. S., and Henry, G. W. (2003). A Sub-Saturn Mass Planet Orbiting HD 3651. , 590(2):1081–1087.

Foster, G. (1996). Wavelets for period analysis of unevenly sampled time series. *Ap.J*, 112:1709–1729.

Frick, P., Baliunas, S. L., Galyagin, D., Sokoloff, D., and Soon, W. (1997). Wavelet Analysis of Stellar Chromospheric Activity Variations. *Ap.J*, 483(1):426–434.

Gan, T., Wang, S. X., Teske, J. K., Mao, S., Howard, W. S., Law, N. M., Batalha, N. E., Vanderburg, A., Dragomir, D., Huang, C. X., Feng, F., Butler, R. P., Crane, J. D., Shectman, S. A., Beletsky, Y., Shporer, A., Montet, B. T., Burt, J. A., Feinstein, A. D., Flowers, E., Nandakumar, S., Barbieri, M., Corbett, H., Ratzloff, J. K., Galliher, N., Chavez, R. G., Vasquez, A., Glazier, A., and

Haislip, J. (2021). Revisiting the HD 21749 planetary system with stellar activity modelling. , 501(4):6042–6061.

Gray, R. O., Corbally, C. J., Garrison, R. F., McFadden, M. T., and Robinson, P. E. (2003). Contributions to the Nearby Stars (NStars) Project: Spectroscopy of Stars Earlier than M0 within 40 Parsecs: The Northern Sample. I. *Ap.J*, 126(4):2048–2059.

Haisch, B. and Schmitt, J. H. M. M. (1994). ROSAT All-Sky Survey Observations of X-Ray Variability in Cool Giant Stars. , 426:716.

Hale, G. E., Ellerman, F., Nicholson, S. B., and Joy, A. H. (1919). The Magnetic Polarity of Sun-Spots. *Ap.J*, 49:153.

Hartmann, L. W. and Noyes, R. W. (1987). Rotation and magnetic activity in main-sequence stars. *Annual Review of Astronomy and Astrophysics*, 25(1):271–301.

Hempelmann, A., Mittag, M., Gonzalez-Perez, J. N., Schmitt, J. H. M. M., Schröder, K. P., and Rauw, G. (2016). Measuring rotation periods of solar-like stars using TIGRE. A study of periodic CaII H+K S-index variability. *A&A*, 586:A14.

Horne, J. H. and Baliunas, S. L. (1986). A Prescription for Period Analysis of Unevenly Sampled Time Series. *Ap.J*, 302:757.

Howe, R. (2009). Solar Interior Rotation and its Variation. *Living Rev. Sol. Phys. 6, 1.*

Huenemoerder, D. P., Schulz, N. S., Testa, P., Drake, J. J., Osten, R. A., and Reale, F. (2010). X-ray Flares of EV Lac: Statistics, Spectra, and Diagnostics. *Ap.J*, 723(2):1558–1567.

Kodaira, K., Ichimura, K., and Nishimura, S. (1976). High-speed five-color photometry of the flare star EV Lacertae. *Publications of the ASJ*, 28:665–674.

Kraft, R. P. (1967). Studies of Stellar Rotation. V. The Dependence of Rotation on Age among Solar-Type Stars. *Ap.J*, 150:551.

Kürster, M. (1996). *in Proc. IAU Symp.*, 176, Stellar Surface Structure, eds Strassmeier K. G. and Linsky J. L., Kluwer, Dordrecht, p. 477.

Lamm, M. H., Bailer-Jones, C. A. L., Mundt, R., Herbst, W., and Scholz, A. (2004). A rotational and variability study of a large sample of PMS stars in <ASTROBJ>NGC 2264</ASTROBJ>. , 417:557–581.

Larmor, J. (1919). *How could a rotating body such as the Sun become a magnet.* Rep. Brit. Assoc. Adv. Sci. 159-160.

Lightkurve Collaboration, Cardoso, J. V. d. M., Hedges, C., Gully-Santiago, M., Saunders, N., Cody, A. M., Barclay, T., Hall, O., Sagear, S., Turtelboom, E., Zhang, J., Tzanidakis, A., Mighell, K., Coughlin, J., Bell, K., Berta-Thompson,

Z., Williams, P., Dotson, J., and Barentsen, G. (2018). Lightkurve: Kepler and TESS time series analysis in Python. Astrophysics Source Code Library.

Lomb, N. R. (1976). Least-Squares Frequency Analysis of Unequally Spaced Data. *Astrophysics and Space Science*, 39(2):447–462.

Lorente, R. and Montesinos, B. (2005). Predicting the Length of Magnetic Cycles in Late-Type Stars. , 632(2):1104–1112.

Mamajek, E. E. and Hillenbrand, L. A. (2008). Improved Age Estimation for Solar-Type Dwarfs Using Activity-Rotation Diagnostics. , 687(2):1264–1293.

Marmier, M., Ségransan, D., Udry, S., Mayor, M., Pepe, F., Queloz, D., Lovis, C., Naef, D., Santos, N. C., Alonso, R., Alves, S., Berthet, S., Chazelas, B., Demory, B. O., Dumusque, X., Eggenberger, A., Figueira, P., Gillon, M., Hagelberg, J., Lendl, M., Mardling, R. A., Mégevand, D., Neveu, M., Sahlmann, J., Sosnowska, D., Tewes, M., and Triaud, A. H. M. J. (2013). The CORALIE survey for southern extrasolar planets. XVII. New and updated long period and massive planets. , 551:A90.

Mathioudakis, M. and Doyle, J. G. (1992). Chromospheric heating in late-type dwarfs : acoustic or magnetic ? , 262:523–532.

Mavridis, L. N. and Avgoloupis, S. (1986). The flare star EV Lac. I. The activity cycle. *A&A*, 154:171–175.

Messina, S., Guinan, E. F., Lanza, A. F., and Ambruster, C. (1999). Activity cycle and surface differential rotation of the single Pleiades star HD 82443 (DX Leo). , 347:249–257.

Messina, S., Nardiello, D., Desidera, S., Baratella, M., Benatti, S., Biazzo, K., and D'Orazi, V. (2022). Gyrochronological dating of the stellar moving group Group X. , 657:L3.

Metcalfe, T. S., Egeland, R., and van Saders, J. (2016). Stellar Evidence That the Solar Dynamo May Be in Transition. , 826(1):L2.

Middelkoop, F. (1982). Magnetic structure in cool stars. IV - Rotation and CA II H and K emission of main-sequence stars. *A&A*, 107(1):31–35.

Miesch, M. (2005). Large-Scale Dynamics of the Convection Zone and Tachocline. *Living Rev. Sol. Phys. 2, 1.*

Miesch, M. S. and Toomre, J. (2009). Turbulence, Magnetism, and Shear in Stellar Interiors. *Annual Review of Fluid Mechanics*, 41(1):317–345.

Mittag, M., Hempelmann, A., Schmitt, J. H. M. M., Fuhrmeister, B., González-Pérez, J. N., and Schröder, K. P. (2017). Stellar rotation periods determined from simultaneously measured Ca II H&K and Ca II IRT lines. , 607:A87.

Montesinos, B., Thomas, J. H., Ventura, P., and Mazzitelli, I. (2001). A new look

at the relationship between activity, dynamo number and Rossby number in late-type stars. *Monthly Notices of the RAS*, 326(3):877–884.

Mullan, D. and Johnson, M. (1995). *in IA U Symp.*, 176, Poster Proceedings, ed. in Strassmeier K. G., Institut fiir Astronomie, Vienna, p. 206.

Noyes, R. W., Hartmann, L. W., Baliunas, S. L., Duncan, D. K., and Vaughan, A. H. (1984). Rotation, convection, and magnetic activity in lower main-sequence stars. *Ap.J*, 279:763–777.

Ossendrijver, A. J. H. and Hoyng, P. (1996). Stochastic and nonlinear fluctuations in a mean field dynamo. *A&A*, 313:959–970.

Pallavicini, R., Golub, L., Rosner, R., Vaiana, G. S., Ayres, T., and Linsky, J. L. (1981). Relations among stellar X-ray emission observed from Einstein, stellar rotation and bolometric luminosity. *Ap.J*, 248:279–290.

Parker, E. N. (1955). The Formation of Sunspots from the Solar Toroidal Field. *Ap.J*, 121:491.

Pettersen, B. R. (1980). Starspots and the rotation of the flare star EV Lac. *A.J.*, 85:871–874.

Pettersen, B. R., Kern, G. A., and Evans, D. S. (1983). Starspots and stellar flares on EV Lac and YZ CMi. *A&A*, 123:184–190.

Pettersen, B. R., Olah, K., and Sandmann, W. H. (1992). Longterm behaviour of starspots. II. A decade of new starspots of photometry of BY Draconis and EV Lacertae. *Ap.J supplement*, 96:497–504.

Pizzolato, N., Maggio, A., Micela, G., Sciortino, S., and Ventura, P. (2003). The stellar activity-rotation relationship revisited: Dependence of saturated and non-saturated X-ray emission regimes on stellar mass for late-type dwarfs. *A&A*, 397:147–157.

Pomerance, B. H., Abbott, B., and Ambruster, C. (1995). Simultaneous EUVE and IUE Flares from the Flare Star EV Lac. In *American Astronomical Society Meeting Abstracts #186*, volume 186 of *American Astronomical Society Meeting Abstracts*, page 21.03.

Priest, E. R. (2020). Solar Physics: Overview. *In Foster, B. (Ed.), Oxford Research Encyclopedia of Physics. Oxford University Press.*

Radick, R. R., Lockwood, G. W., Skiff, B. A., and Baliunas, S. L. (1998). Patterns of Variation among Sun-like Stars. *Ap.J supplement*, 118(1):239–258.

Ricker, G. R., Winn, J. N., Vanderspek, R., Latham, D. W., Bakos, G. Á., Bean, J. L., Berta-Thompson, Z. K., Brown, T. M., Buchhave, L., Butler, N. R., Butler, R. P., Chaplin, W. J., Charbonneau, D., Christensen-Dalsgaard, J., Clampin, M., Deming, D., Doty, J., De Lee, N., Dressing, C., Dunham, E. W., Endl, M., Fressin, F., Ge, J., Henning, T., Holman, M. J., Howard, A. W., Ida, S., Jenkins, J. M., Jernigan, G., Johnson, J. A., Kaltenegger, L., Kawai, N., Kjeldsen, H.,

Laughlin, G., Levine, A. M., Lin, D., Lissauer, J. J., MacQueen, P., Marcy, G., McCullough, P. R., Morton, T. D., Narita, N., Paegert, M., Palle, E., Pepe, F., Pepper, J., Quirrenbach, A., Rinehart, S. A., Sasselov, D., Sato, B., Seager, S., Sozzetti, A., Stassun, K. G., Sullivan, P., Szentgyorgyi, A., Torres, G., Udry, S., and Villasenor, J. (2015). Transiting Exoplanet Survey Satellite (TESS). *Journal of Astronomical Telescopes, Instruments, and Systems*, 1:014003.

Roizman, G. S. (1984). Is the Flare Star Ev-Lacertae an Eclipsing Binary. *Soviet Astronomy Letters*, 10:116–118.

Roques, P. E. (1955). A Search for Flare Stars. *Publications of the ASP*, 67(394):34.

Rüdiger, G. and Hollerbach, R. (2004). *The magnetic universe : geophysical and astrophysical dynamo theory.*

Ruediger, G. (1989). *Differential rotation and stellar convection. Sun and the solar stars.*

Rutten, R. G. M. (1984). Magnetic structure in cool stars. VII. Absolute surface flux in CA IIH and K line cores. *A&A*, 130:353–360.

Rutten, R. G. M. and Schrijver, C. J. (1987). Magnetic structure in cool stars. XIII - Appropriate units for the rotation-activity relation. *A&A*, 177(1-2):155–162.

Saar, S. H. and Brandenburg, A. (1999). Time Evolution of the Magnetic Activity Cycle Period. II. Results for an Expanded Stellar Sample. *Ap.J*, 524(1):295–310.

Scargle, J. D. (1982). Studies in astronomical time series analysis. II. Statistical aspects of spectral analysis of unevenly spaced data. *Ap.J*, 263:835–853.

Scargle, J. D. (1998). Studies in Astronomical Time Series Analysis. V. Bayesian Blocks, a New Method to Analyze Structure in Photon Counting Data. *Ap.J*, 504(1):405–418.

Schatten, K. H. (1993). Heliographic latitude dependence of the Sun's irradiance. *J. Geophys. Res.*, 98(A11)(18):907–18,910.

Schleicher, D. R. G. and Mennickent, R. E. (2017). A dynamo mechanism as the potential origin of the long cycle in double periodic variables. *A&A*, 602:A109.

Schmitt, J. H. M. M. (1994). ROSAT Observations of Stellar Flares. *Ap.J supplement*, 90:735.

Schröder, C., Reiners, A., and Schmitt, J. H. M. M. (2009). Ca II HK emission in rapidly rotating stars. Evidence for an onset of the solar-type dynamo. , 493(3):1099–1107.

Schwabe, S. H. (1843). Die sonne. *Astronomische Nachrichten*, 20(17):283–286.

Sciortino, S., Maggio, A., Favata, F., and Orlando, S. (1999). X-ray spectroscopy of the active dM stars: AD Leo and EV Lac. *A&A*, 342:502–514.

Soderblom, D. R., Jones, B. F., Balachandran, S., Stauffer, J. R., Duncan, D. K., Fedele, S. B., and Hudon, J. D. (1993). The Evolution of the Lithium Abundances of Solar-Type Stars. III. The Pleiades. *Astronomical Journal*, 106:1059.

Solanki, S. K., Inhester, B., and Schüssler, M. (2006). The solar magnetic field. *Reports on Progress in Physics*, 69(3):563–668.

Spoerer, G. (1889). Ueber die periodicitat der Sonnenflecken seit dem Jahr 1618. *Nova Acta der Ksl. Leop.- Carol. Deutschen Akademie der Naturforscher*, 53(2):281–324.

Steenbeck, M., Krause, F., and Rädler, K. H. (1966). Berechnung der mittleren LORENTZ-Feldstärke ???? X ???? für ein elektrisch leitendes Medium in turbulenter, durch CORIOLIS-Kräfte beeinflußter Bewegung. *Zeitschrift Naturforschung Teil A*, 21:369.

Stepien, K. (1993). Rossby Number or Rotation Period? In Krause, F., Radler, K. H., and Rudiger, G., editors, *The Cosmic Dynamo*, volume 157, page 141.

Tang, S.-Y., Pang, X., Yuan, Z., Chen, W. P., Hong, J., Goldman, B., Just, A., Shukirgaliyev, B., and Lin, C.-C. (2019). Discovery of Tidal Tails in Disrupting Open Clusters: Coma Berenices and a Neighbor Stellar Group. , 877(1):12.

Torrence, C. and Compo, G. P. (1998). A Practical Guide to Wavelet Analysis. *Bulletin of the American Meteorological Society*, 79(1):61–78.

VanderPlas, J. T. (2018). Understanding the Lomb-Scargle Periodogram. *Ap.J supplement*, 236(1):16.

Vaughan, A. H. and Preston, G. W. (1980). A survey of chromospheric CA II H and K emission in field stars of the solar neighborhood. *Publications of the ASP*, 92:385–391.

Vaughan, A. H., Preston, G. W., and Wilson, O. C. (1978). Flux measurements of Ca II and K emission. *Publications of the ASP*, 90:267–274.

Villegas, F. (2019). *Searching the cycle period in chromospherically active stars. Universidad de Concepción.*

Vogt, S. S. (1981). Starspots - A review of observations and theory. In Cram, L. E. and Thomas, J. H., editors, *The Physics of Sunspots*, pages 455–479.

Wang, L. and Sassen, K. (2008). Wavelet Analysis of Cirrus Multiscale Structures from Lidar Backscattering: A Cirrus Uncinus Complex Case Study. *Journal of Applied Meteorology and Climatology*, 47(10):2645.

White, S. M., Jackson, P. D., and Kundu, M. R. (1989). A VLA Survey of Nearby Flare Stars. *Ap.J supplement*, 71:895.

Wilson, O. C. (1968). Flux Measurements at the Centers of Stellar H- and K-Lines. *Ap.J*, 153:221.

Wright, N. J., Drake, J. J., Mamajek, E. E., and Henry, G. W. (2011). The Stellar-activity-Rotation Relationship and the Evolution of Stellar Dynamos. , 743(1):48.

Zechmeister, M. and Kürster, M. (2009). The generalised Lomb-Scargle periodogram. A new formalism for the floating-mean and Keplerian periodograms. , 496(2):577–584.

Appendix A

A1 Sample of stars from the article by Boro Saikia et al. (2018)

HD 3651

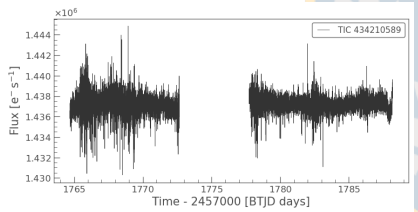

(a) Lightcurve of HD 3651

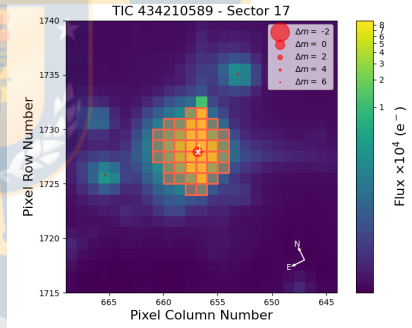

(b) Target Pixel File (TPF) of HD 3651

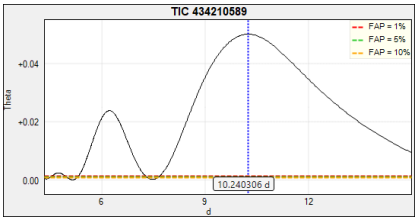

(c) Rotation period using GLS

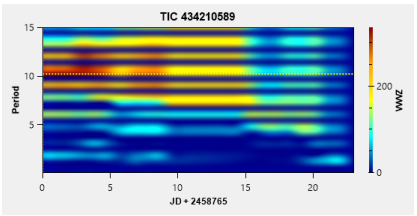

(d) Rotation period using WWZ

HD 4628

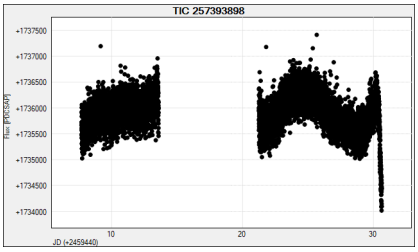

(a) Lightcurve of HD 4628

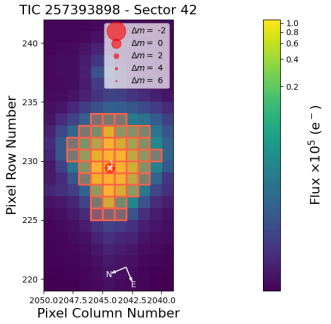

(b) Target Pixel File (TPF) of HD 4628

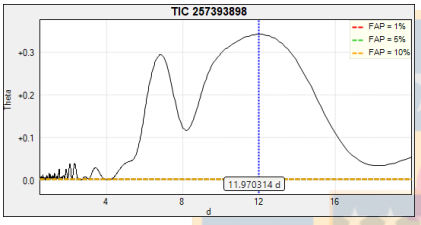

(c) Rotation period using GLS

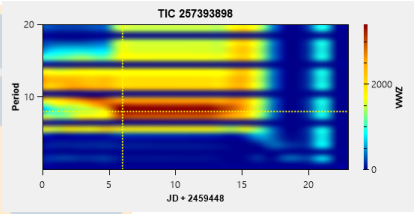

(d) Rotation period using WWZ

HD 10476

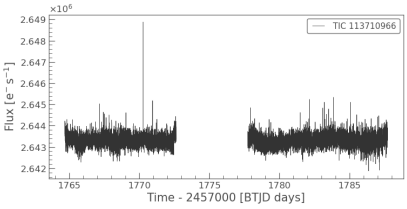

(a) Lightcurve of HD 10476

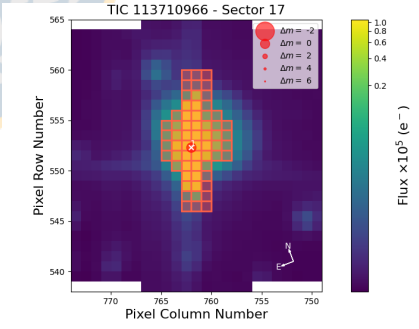

(b) Target Pixel File (TPF) of HD 10476

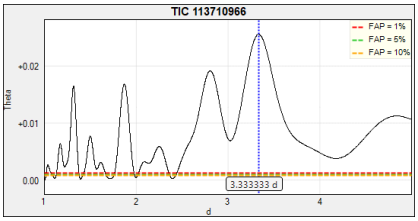

(c) Rotation period using GLS

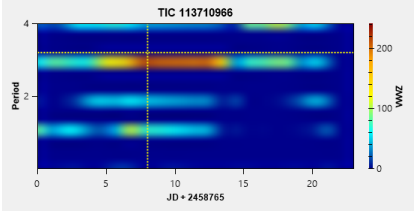

(d) Rotation period using WWZ

HD 16160

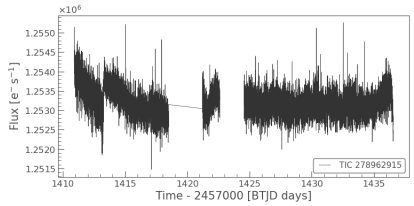

(a) Lightcurve of HD 16160

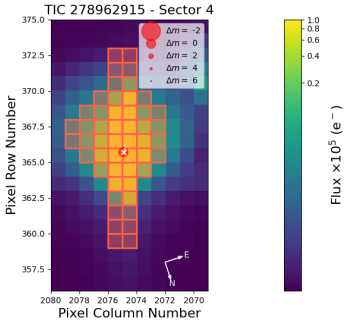

(b) Target Pixel File (TPF) of HD 16160

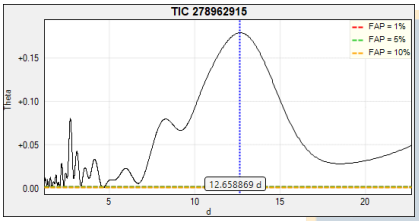

(c) Rotation period using GLS

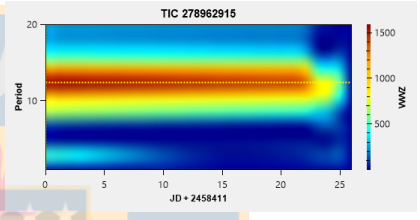

(d) Rotation period using WWZ

HD 26965

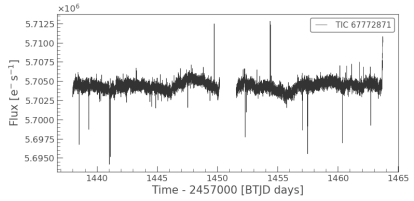

(a) Lightcurve of HD 26965

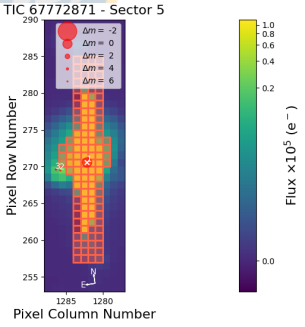

(b) Target Pixel File (TPF) of HD 26965

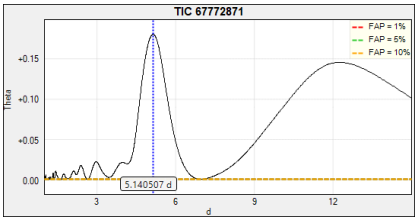

(c) Rotation period using GLS

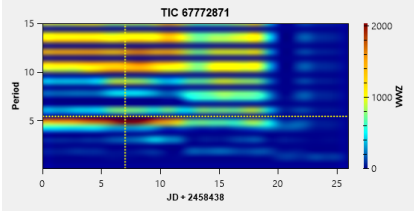

(d) Rotation period using WWZ

HD 32147

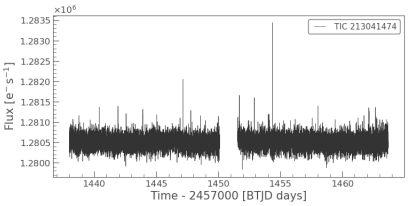

(a) Lightcurve of HD 32147

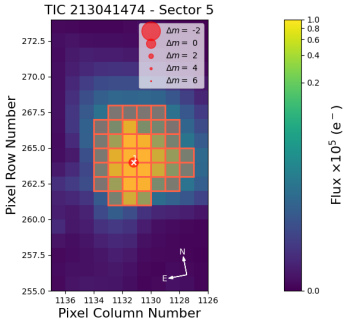

(b) Target Pixel File (TPF) of HD 32147

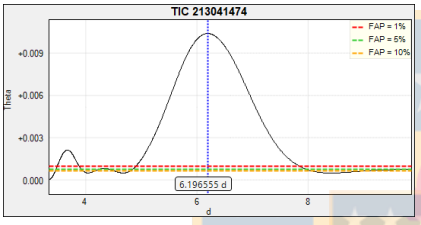

(c) Rotation period using GLS

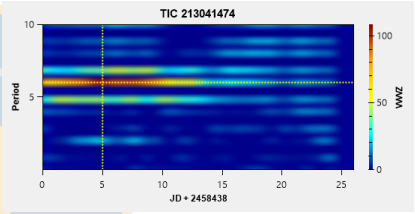

(d) Rotation period using WWZ

HD 81809

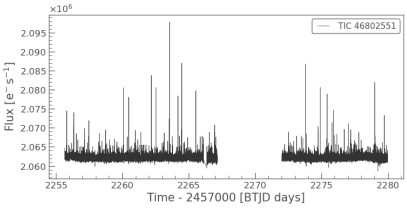

(a) Lightcurve of HD 81809

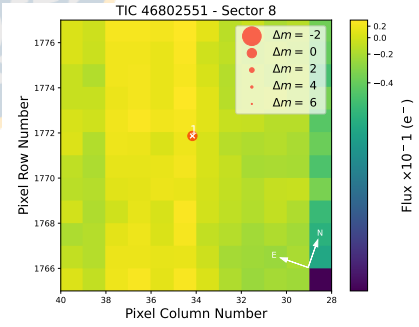

(b) Target Pixel File (TPF) of HD 81809

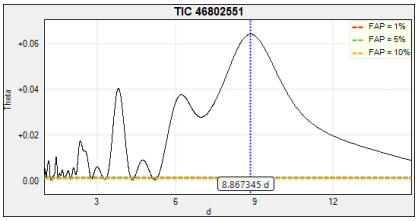

(c) Rotation period using GLS

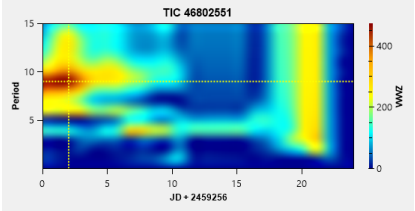

(d) Rotation period using WWZ

HD 103095

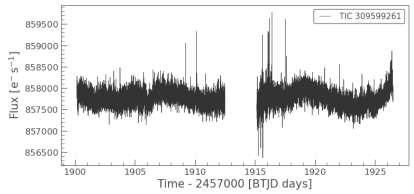

(a) Lightcurve of HD 103095

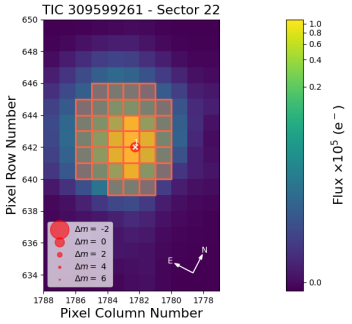

(b) Target Pixel File (TPF) of HD 103095

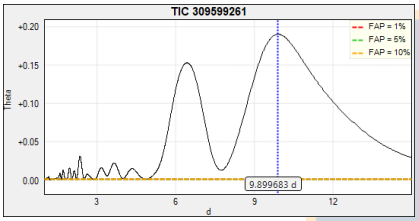

(c) Rotation period using GLS

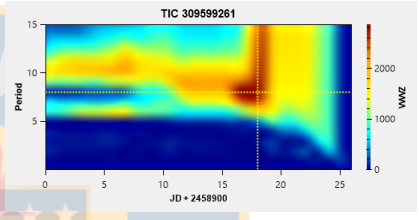

(d) Rotation period using WWZ

HD 166620

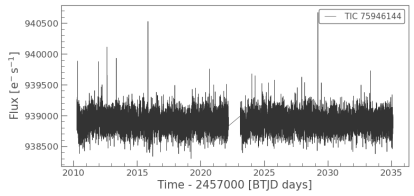

(a) Lightcurve of HD 166620

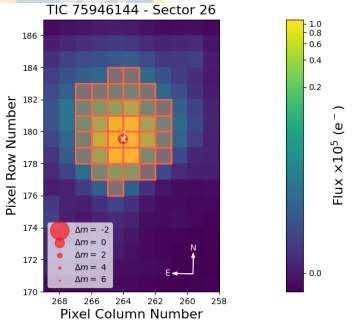

(b) Target Pixel File (TPF) of HD 166620

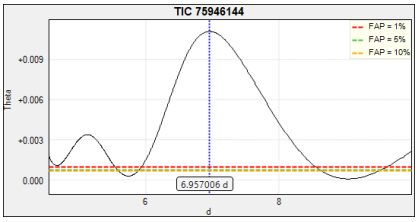

(c) Rotation period using GLS

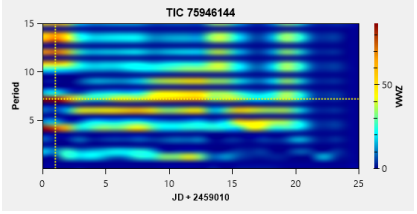

(d) Rotation period using WWZ

HD 185144

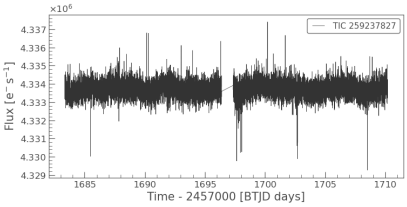

(a) Lightcurve of HD 185144

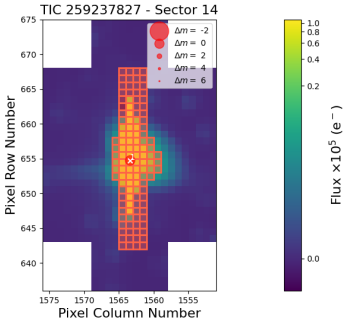

(b) Target Pixel File (TPF) of HD 185144

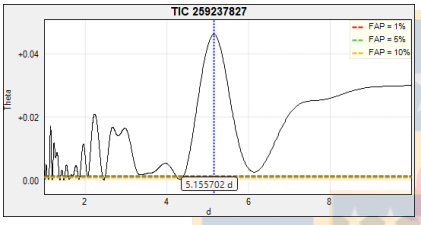

(c) Rotation period using GLS

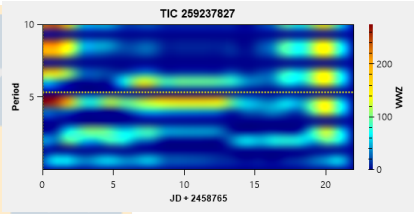

(d) Rotation period using WWZ

HD 201091

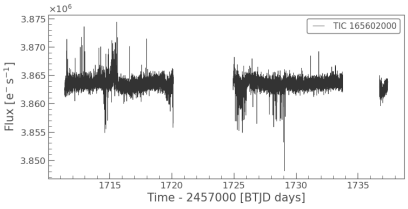

(a) Lightcurve of HD 201091

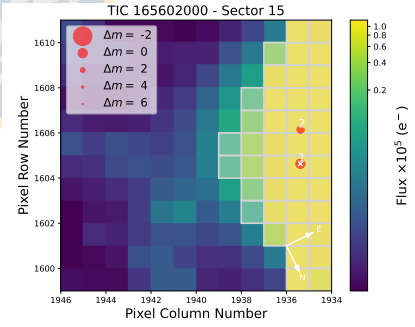

(b) Target Pixel File (TPF) of HD 201091

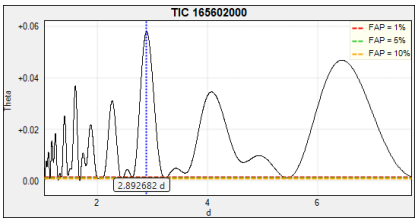

(c) Rotation period using GLS

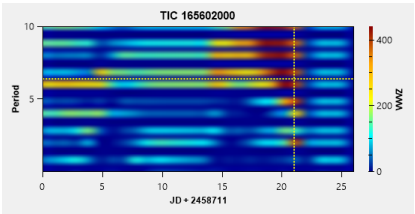

(d) Rotation period using WWZ

HD 219834B

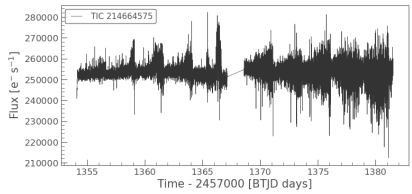

(a) Lightcurve of HD 219834B

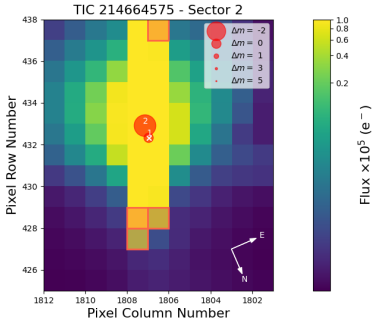

(b) Target Pixel File (TPF) of HD 219834B

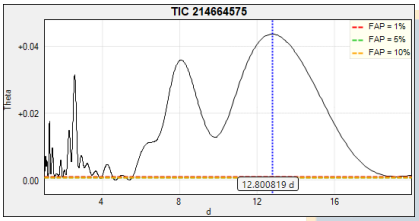

(c) Rotation period using GLS

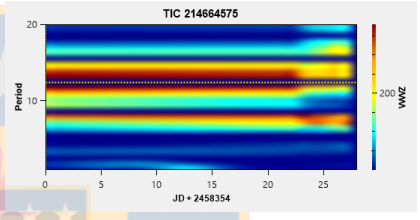

(d) Rotation period using WWZ

HD 101501

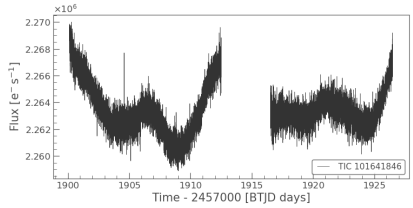

(a) Lightcurve of HD 101501

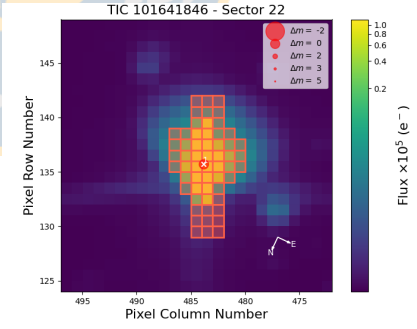

(b) Target Pixel File (TPF) of HD 101501

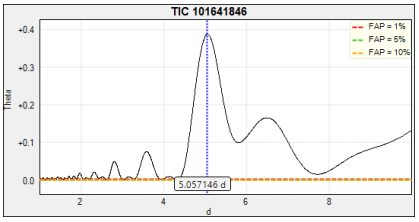

(c) Rotation period using GLS

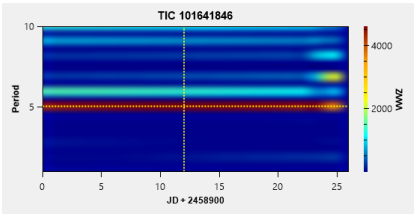

(d) Rotation period using WWZ

HD 20630

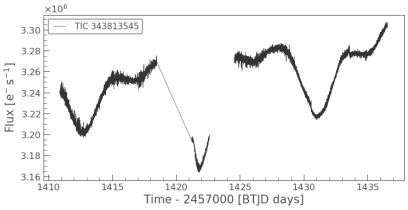

(a) Lightcurve of HD 206300

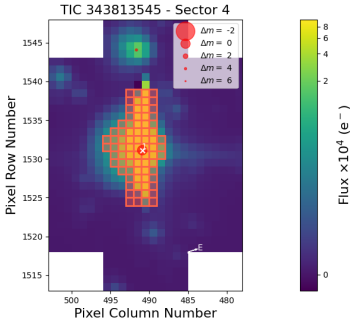

(b) Target Pixel File (TPF) of HD 20630

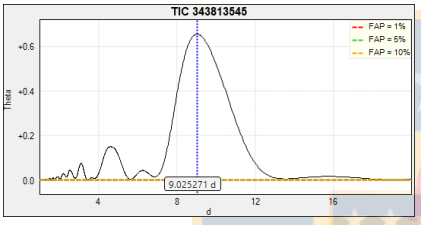

(c) Rotation period using GLS

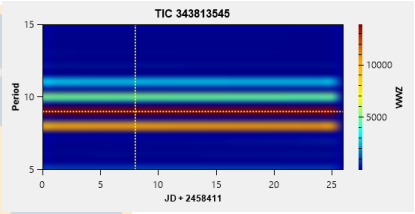

(d) Rotation period using WWZ

HD 10780

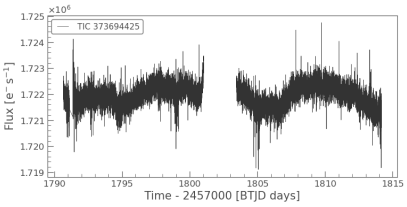

(a) Lightcurve of HD 10780

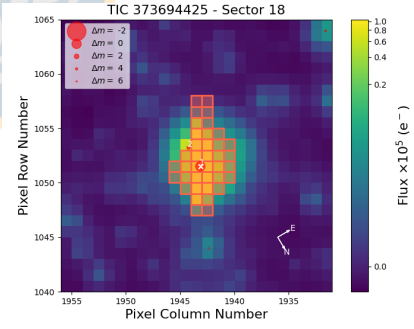

(b) Target Pixel File (TPF) of HD 10780

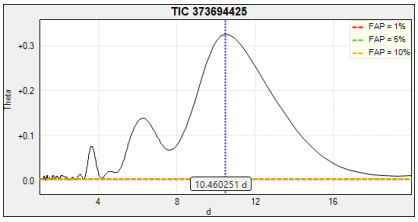

(c) Rotation period using GLS

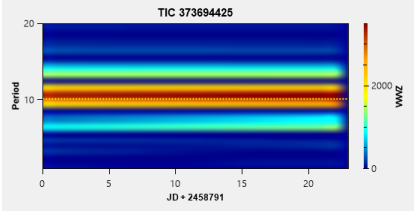

(d) Rotation period using WWZ

HD 18256

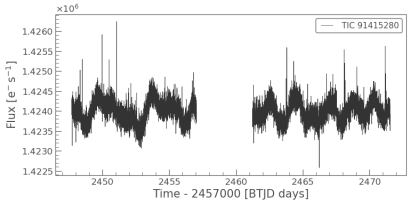

(a) Lightcurve of HD 18256

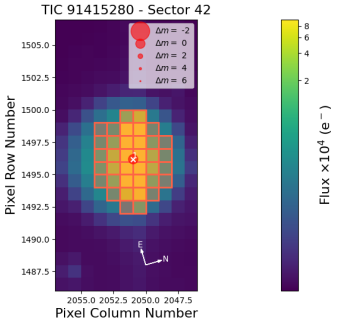

(b) Target Pixel File (TPF) of HD 18256

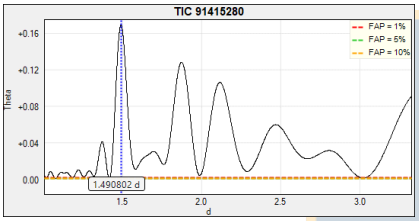

(c) Rotation period using GLS

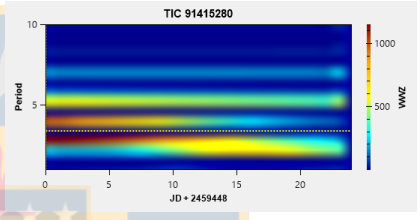

(d) Rotation period using WWZ

HD 26913

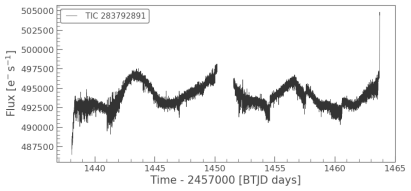

(a) Lightcurve of HD 26913

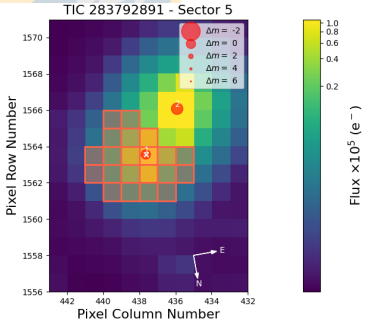

(b) Target Pixel File (TPF) of HD 26913

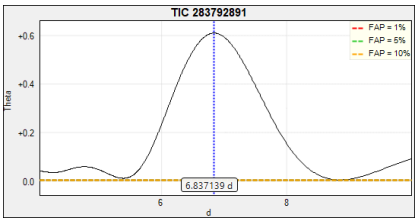

(c) Rotation period using GLS

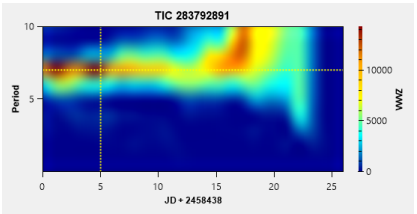

(d) Rotation period using WWZ

HD 26923

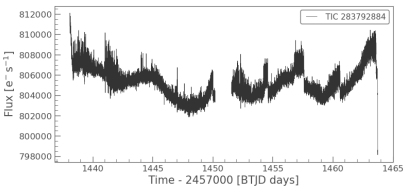

(a) Lightcurve of HD 26923

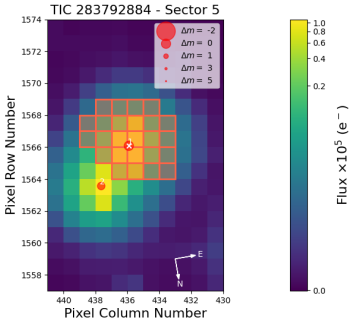

(b) Target Pixel File (TPF) of HD 26923

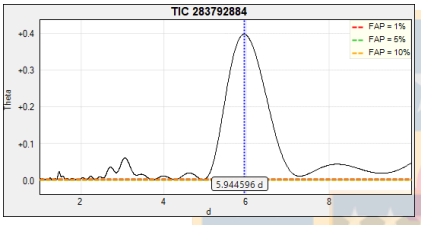

(c) Rotation period using GLS

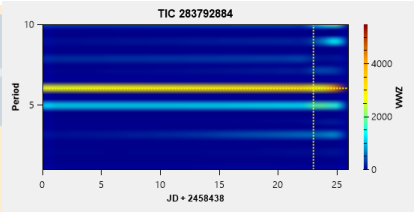

(d) Rotation period using WWZ

HD 37394

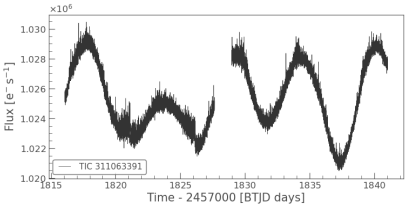

(a) Lightcurve of HD 37394

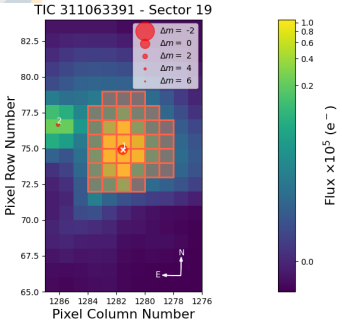

(b) Target Pixel File (TPF) of HD 37394

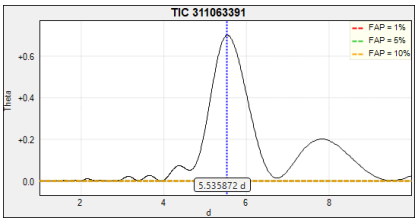

(c) Rotation period using GLS

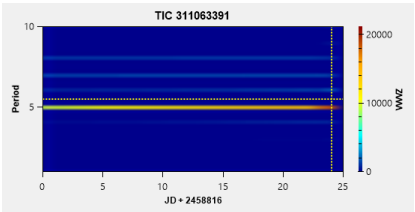

(d) Rotation period using WWZ

HD 76151

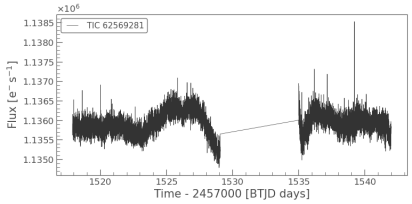

(a) Lightcurve of HD 76151

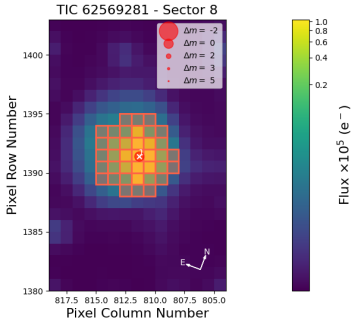

(b) Target Pixel File (TPF) of HD 76151

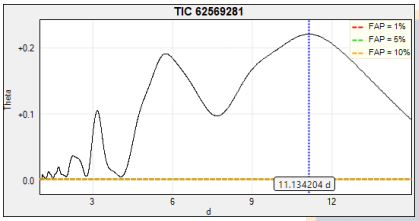

(c) Rotation period using GLS

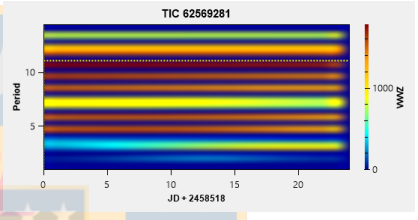

(d) Rotation period using WWZ

HD 78366

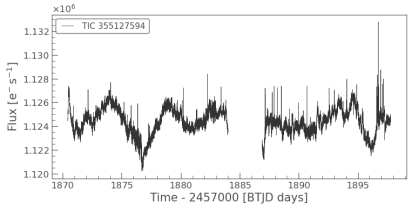

(a) Lightcurve of HD 78366

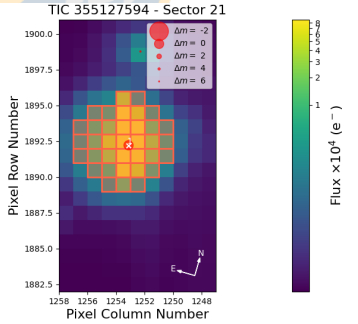

(b) Target Pixel File (TPF) of HD 78366

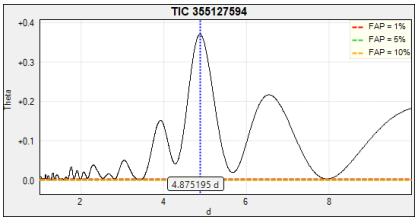

(c) Rotation period using GLS

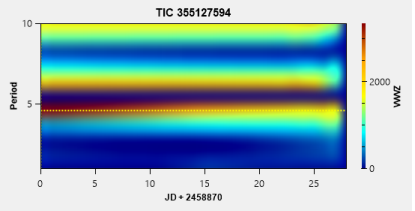

(d) Rotation period using WWZ

HD 82443

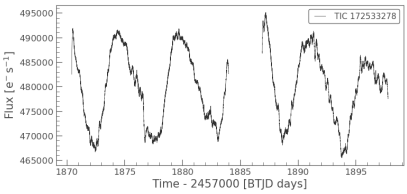

(a) Lightcurve of HD 82443

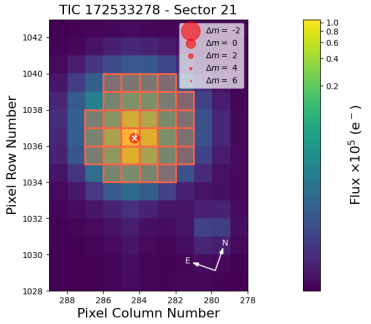

(b) Target Pixel File (TPF) of HD 82443

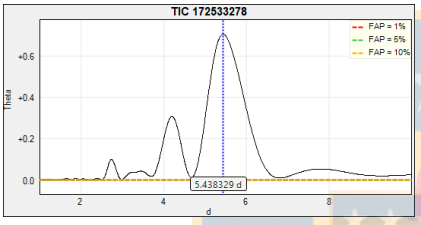

(c) Rotation period using GLS

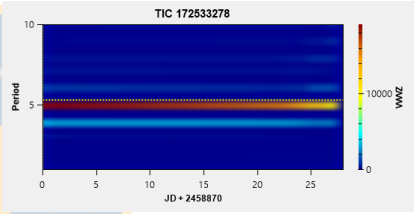

(d) Rotation period using WWZ

HD 82885

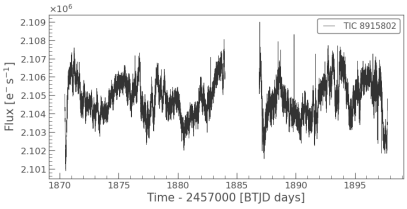

(a) Lightcurve of HD 82885

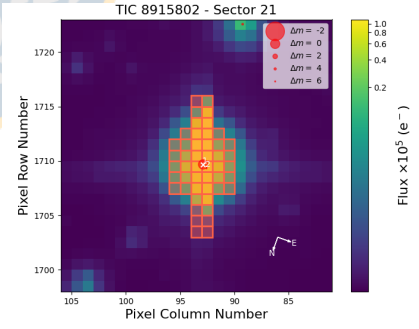

(b) Target Pixel File (TPF) of HD 82885

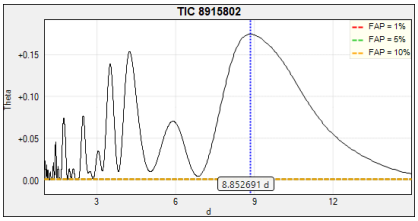

(c) Rotation period using GLS

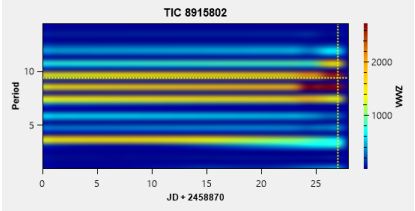

(d) Rotation period using WWZ

HD 100180

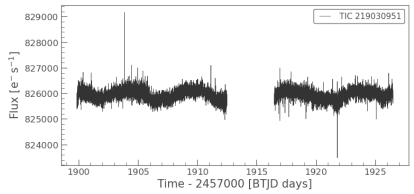

(a) Lightcurve of HD 100180

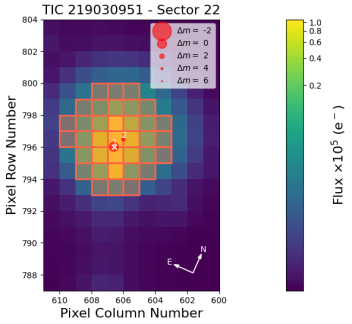

(b) Target Pixel File (TPF) of HD 100180

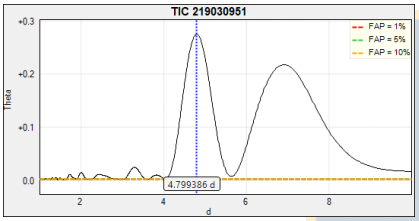

(c) Rotation period using GLS

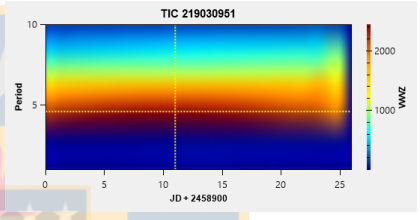

(d) Rotation period using WWZ

HD 115043

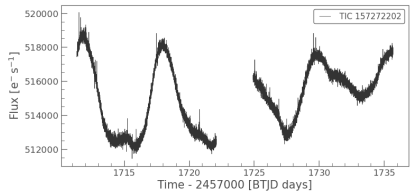

(a) Lightcurve of HD 115043

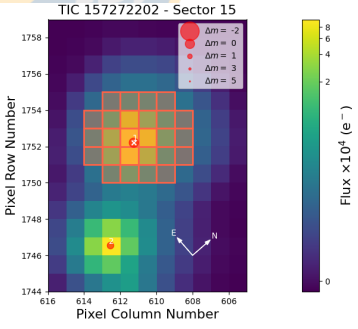

(b) Target Pixel File (TPF) of HD 115043

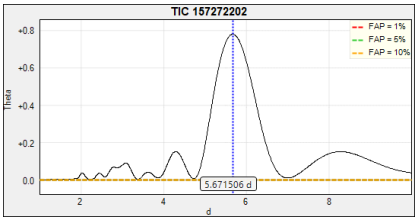

(c) Rotation period using GLS

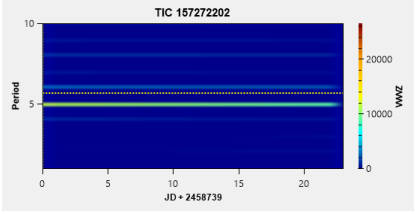

(d) Rotation period using WWZ

HD 115383

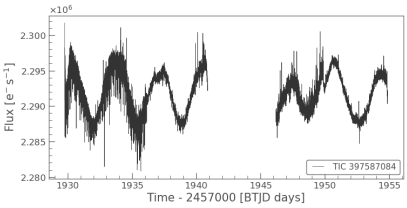

(a) Lightcurve of HD 115383

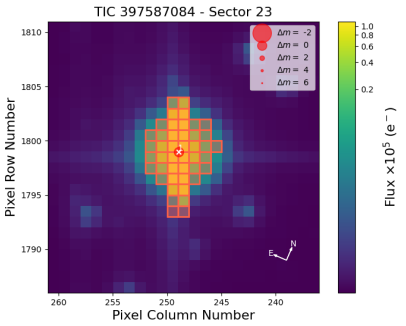

(b) Target Pixel File (TPF) of HD 115383

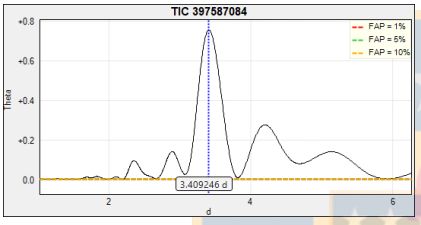

(c) Rotation period using GLS

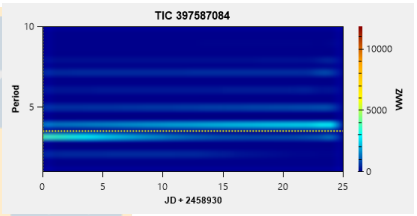

(d) Rotation period using WWZ

HD 201092

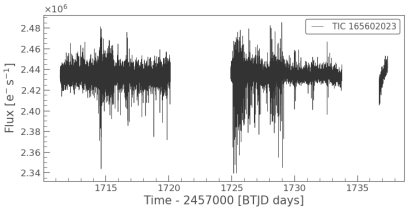

(a) Lightcurve of HD 201092

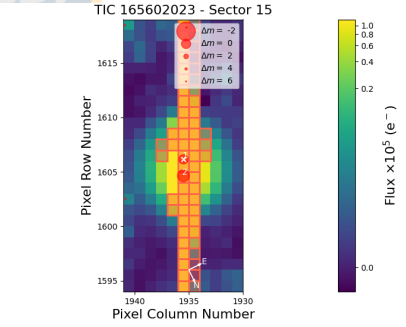

(b) Target Pixel File (TPF) of HD 201092

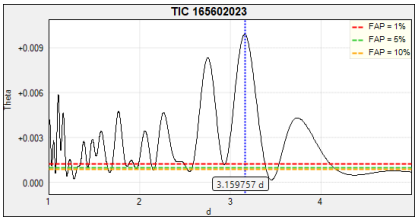

(c) Rotation period using GLS

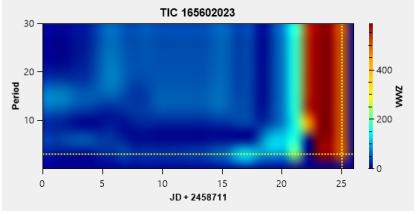

(d) Rotation period using WWZ

HD 20003

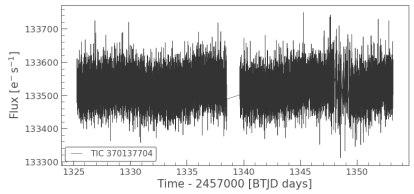

(a) Lightcurve of HD 20003

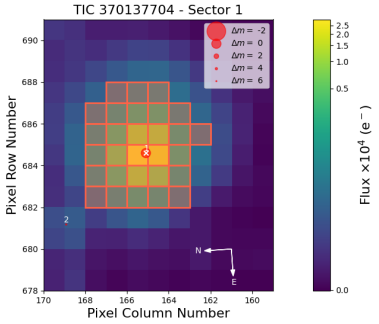

(b) Target Pixel File (TPF) of HD 20003

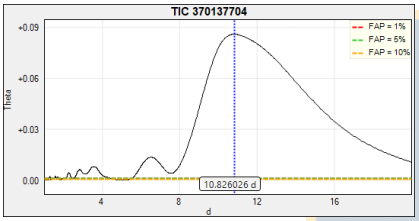

(c) Rotation period using GLS

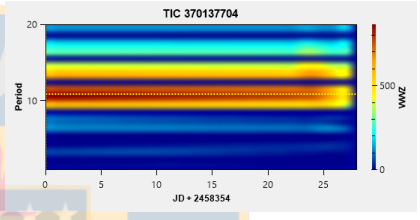

(d) Rotation period using WWZ

HD 20619

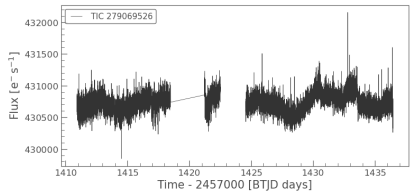

(a) Lightcurve of HD 20619

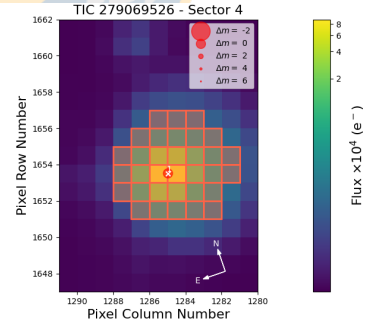

(b) Target Pixel File (TPF) of HD 20619

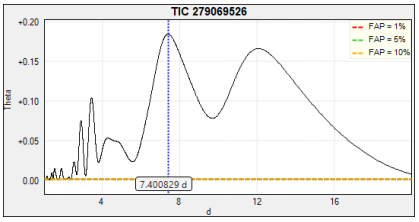

(c) Rotation period using GLS

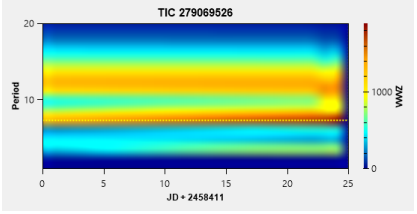

(d) Rotation period using WWZ

HD 21693

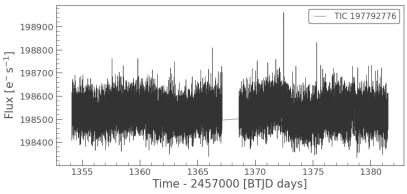

(a) Lightcurve of HD 21693

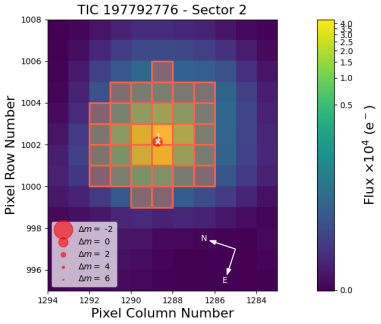

(b) Target Pixel File (TPF) of HD 21693

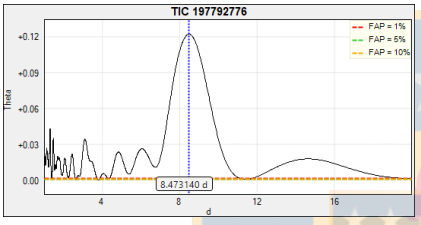

(c) Rotation period using GLS

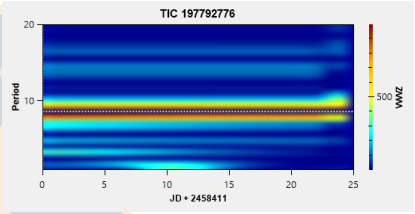

(d) Rotation period using WWZ

HD 45184

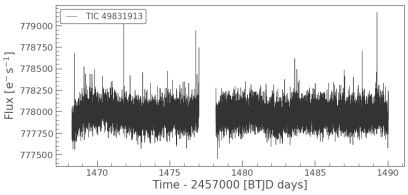

(a) Lightcurve of HD 45184

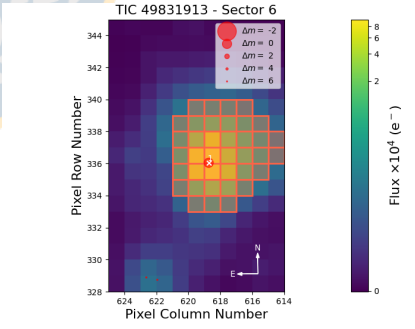

(b) Target Pixel File (TPF) of HD 45184

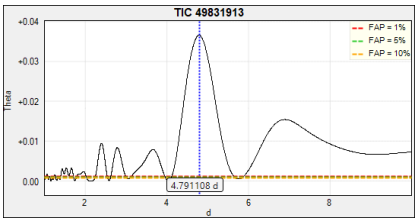

(c) Rotation period using GLS

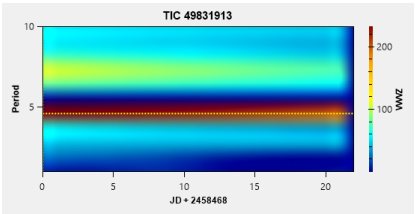

(d) Rotation period using WWZ

HD 7199

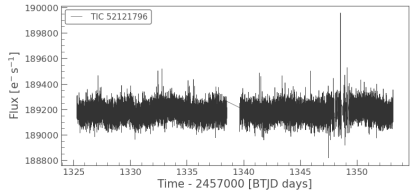

(a) Lightcurve of HD 7199

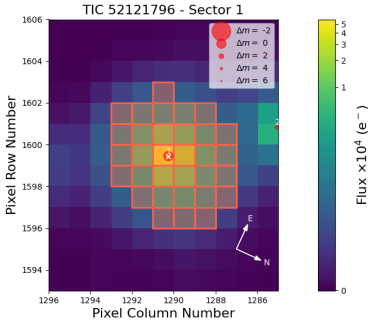

(b) Target Pixel File (TPF) of HD 7199

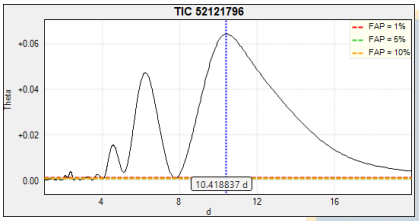

(c) Rotation period using GLS

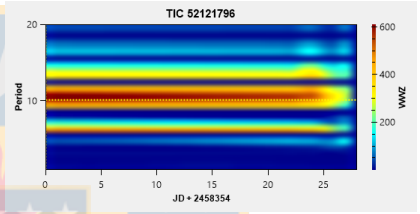

(d) Rotation period using WWZ

HD 82516

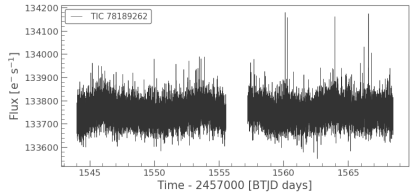

(a) Lightcurve of HD 82516

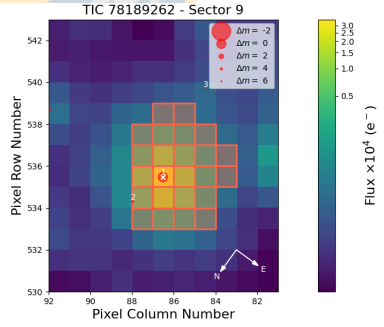

(b) Target Pixel File (TPF) of HD 82516

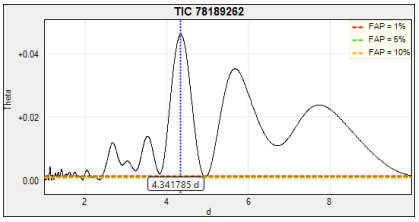

(c) Rotation period using GLS

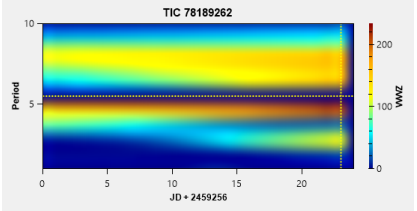

(d) Rotation period using WWZ

HD 89454

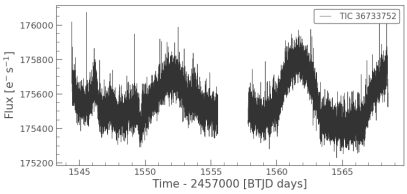

(a) Lightcurve of HD 89454

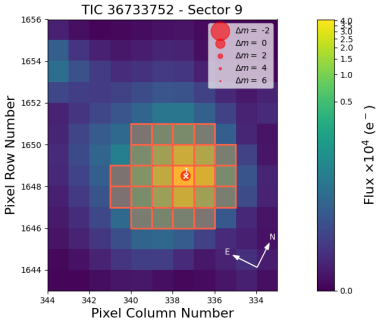

(b) Target Pixel File (TPF) of HD 89454

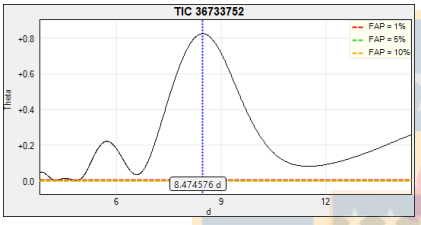

(c) Rotation period using GLS

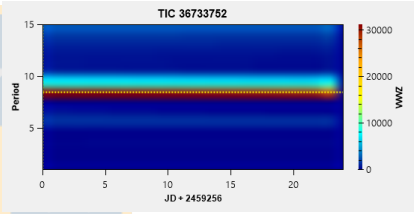

(d) Rotation period using WWZ

HD 157830

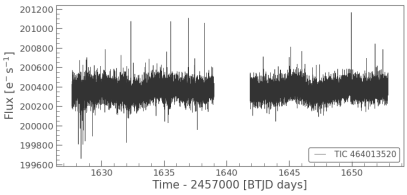

(a) Lightcurve of HD 157830

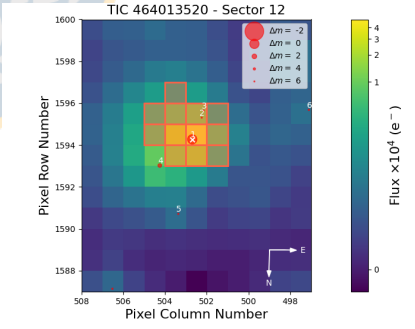

(b) Target Pixel File (TPF) of HD 157830

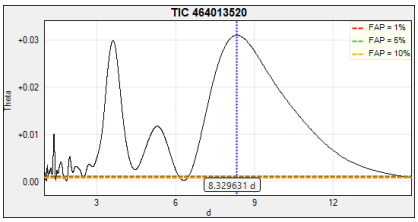

(c) Rotation period using GLS

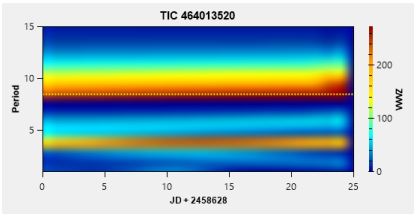

(d) Rotation period using WWZ

HD 361

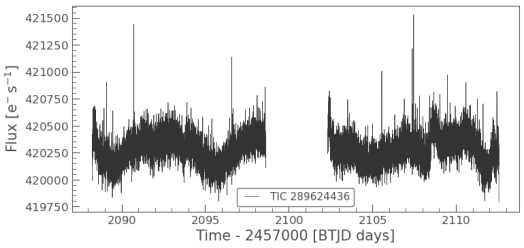

Lightcurve of HD 361

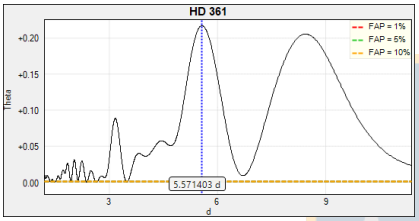

(a) Rotation period using GLS

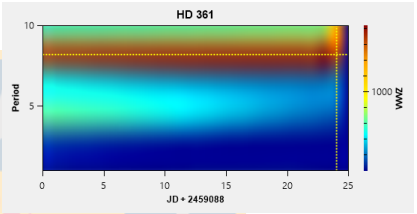

(b) Rotation period using WWZ

HD 12617

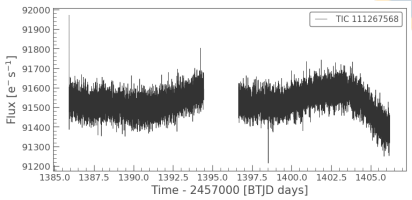

(a) Lightcurve of HD 12617

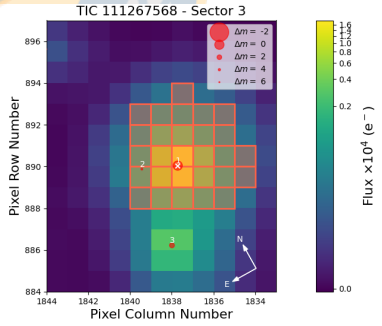

(b) Target Pixel File (TPF) of HD 12617

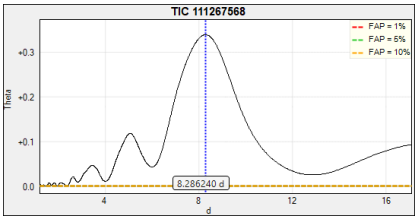

(c) Rotation period using GLS

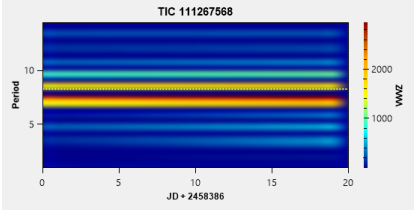

(d) Rotation period using WWZ

HD 166724

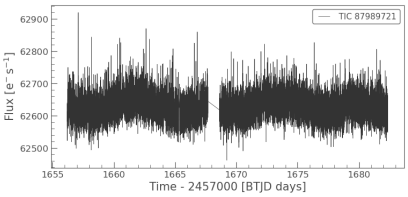

(a) Lightcurve of HD 166724

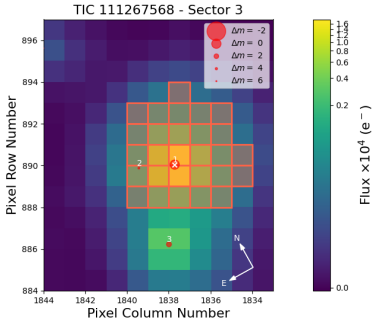

(b) Target Pixel File (TPF) of HD 166620

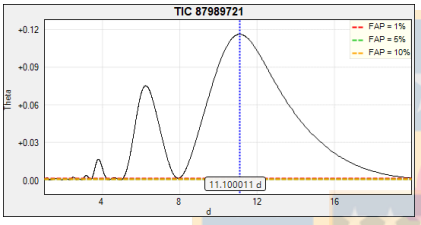

(c) Rotation period using GLS

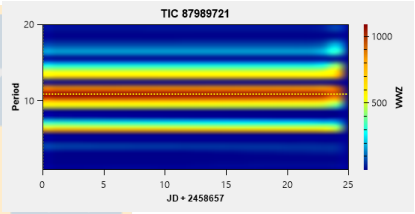

(d) Rotation period using WWZ

HD 21749

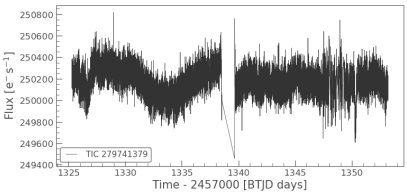

(a) Lightcurve of HD 21749

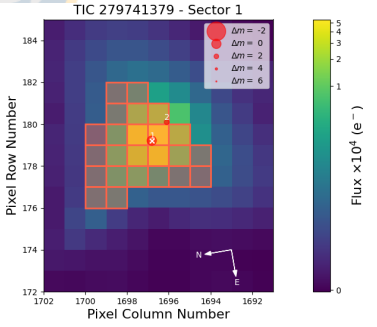

(b) Target Pixel File (TPF) of HD 21749

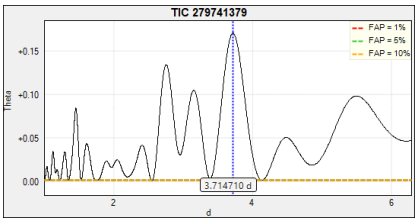

(c) Rotation period using GLS

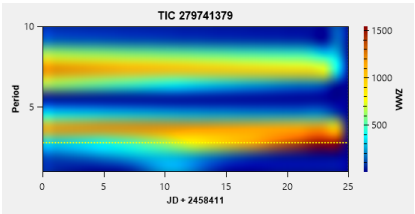

(d) Rotation period using WWZ

HD 154577

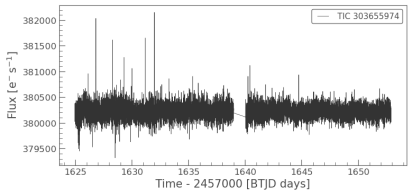

(a) Lightcurve of HD 154577

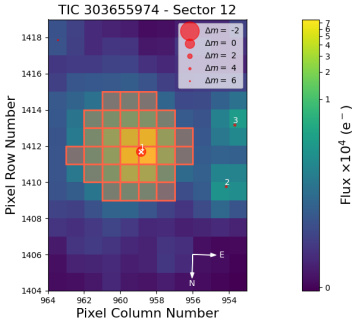

(b) Target Pixel File (TPF) of HD 154577

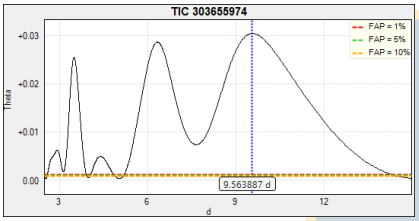

(c) Rotation period using GLS

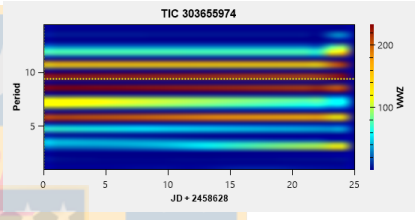

(d) Rotation period using WWZ

HD 88742

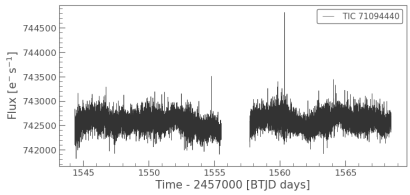

(a) Lightcurve of HD 88742

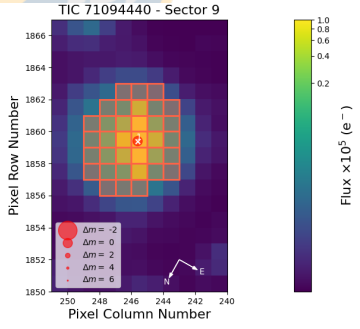

(b) Target Pixel File (TPF) of HD 88742

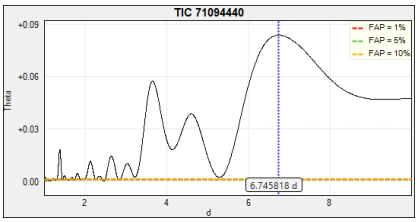

(c) Rotation period using GLS

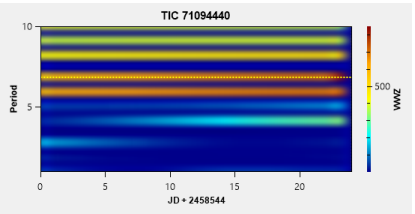

(d) Rotation period using WWZ

A2 Sample of stars from the article by Messina et al. (2022)

TIC 155856633

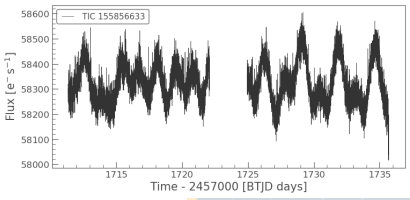

(a) Lightcurve of TIC 155856633

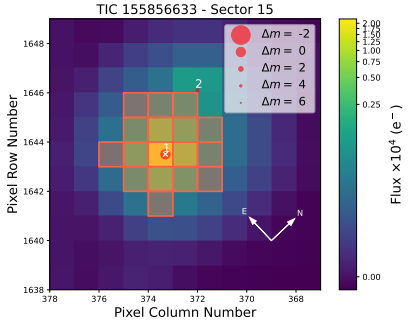

(b) Target Pixel File (TPF) of TIC 155856633

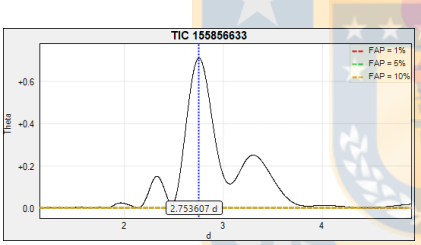

(c) Rotation period using GLS

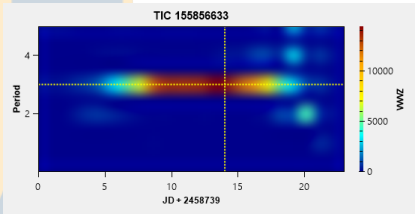

(d) Rotation period using WWZ

TIC 459221499

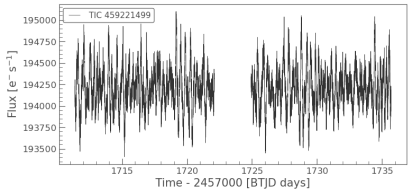

(a) Lightcurve of TIC 459221499

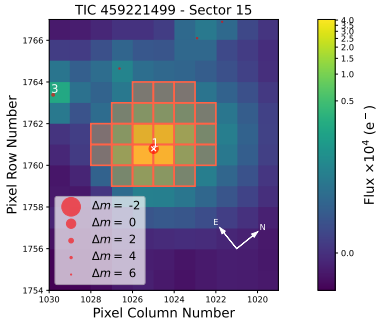

(b) Target Pixel File (TPF) of TIC 459221499

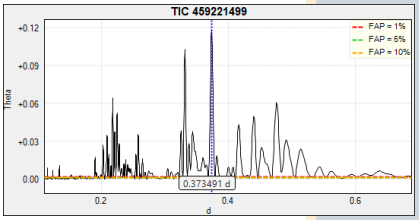

(c) Rotation period using GLS

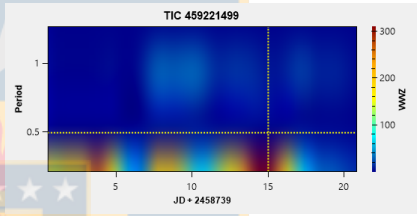

(d) Rotation period using WWZ

TIC 332312964

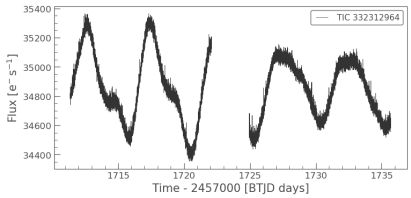

(a) Lightcurve of TIC 332312964

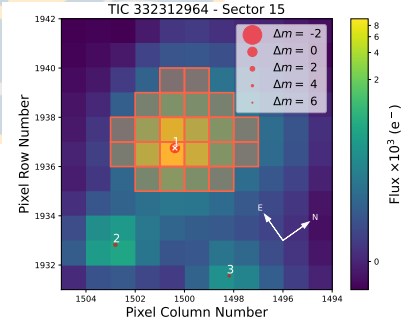

(b) Target Pixel File (TPF) of TIC 332312964

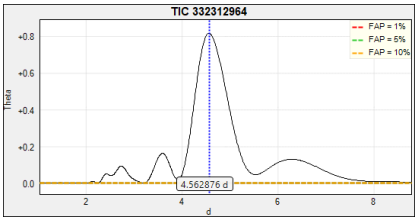

(c) Rotation period using GLS

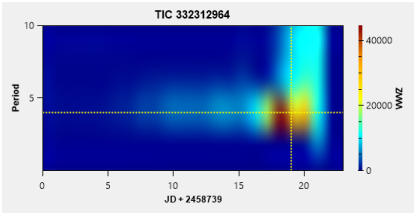

(d) Rotation period using WWZ

TIC 141819826

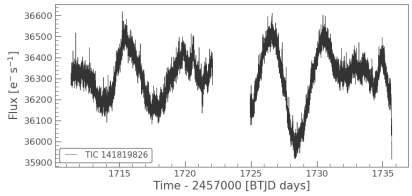

(a) Lightcurve of TIC 141819826

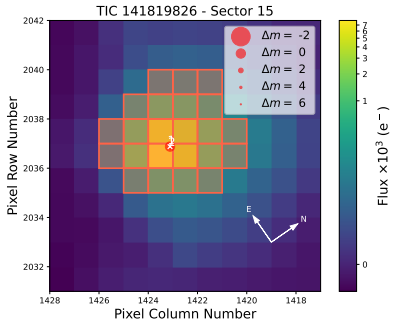

(b) Target Pixel File (TPF) of TIC 141819826

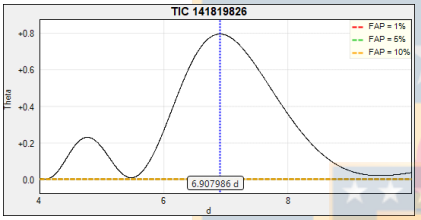

(c) Rotation period using GLS

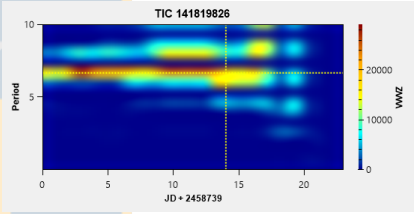

(d) Rotation period using WWZ

TIC 311001628

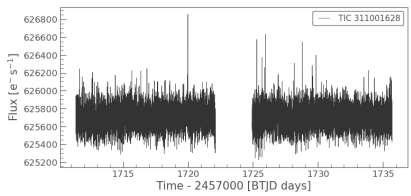

(a) Lightcurve of TIC 311001628

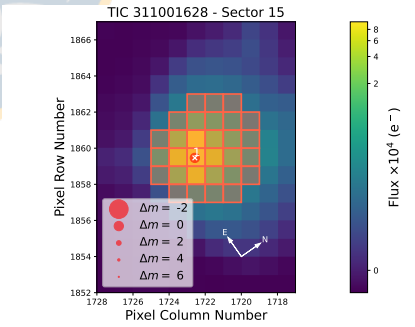

(b) Target Pixel File (TPF) of TIC 311001628

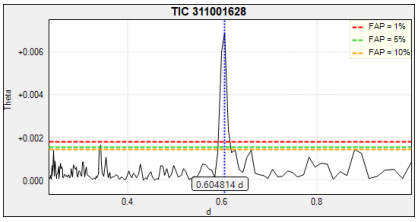

(c) Rotation period using GLS

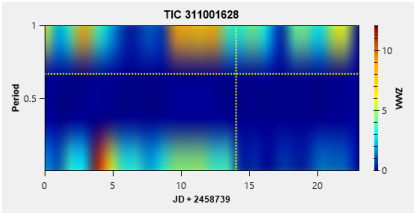

(d) Rotation period using WWZ

TIC 310338842

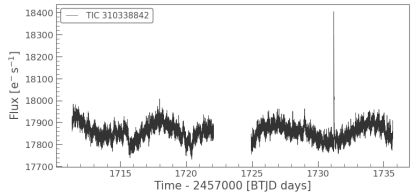

(a) Lightcurve of TIC 310338842

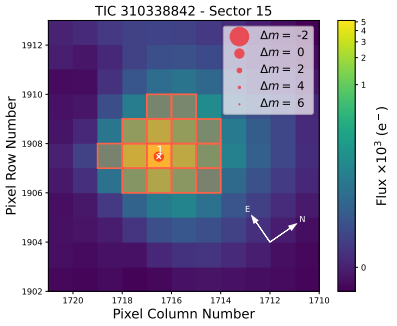

(b) Target Pixel File (TPF) of TIC 310338842

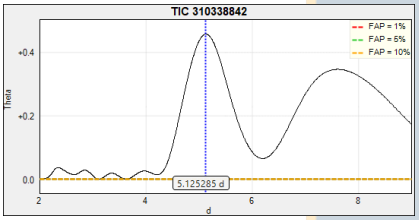

(c) Rotation period using GLS

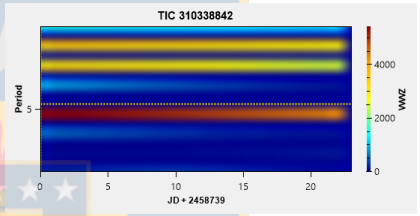

(d) Rotation period using WWZ

TIC 141861147

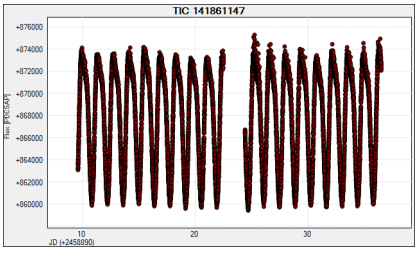

(a) Lightcurve of TIC 141861147

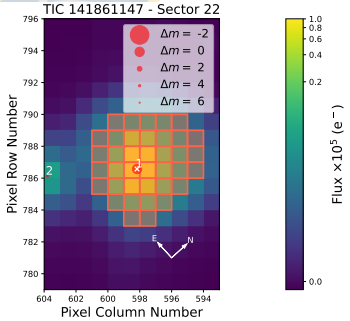

(b) Target Pixel File (TPF) of TIC 141861147

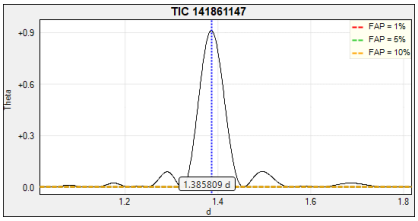

(c) Rotation period using GLS

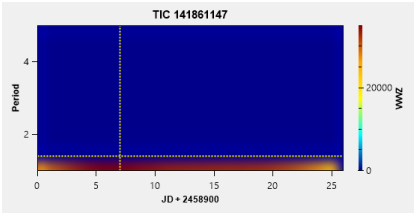

(d) Rotation period using WWZ

TIC 141863294

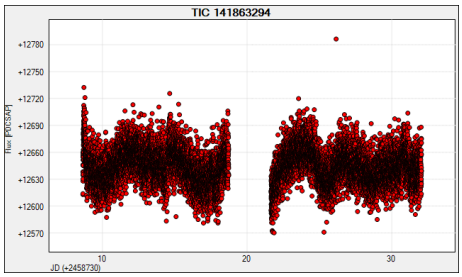

Lightcurve of TIC 141863294

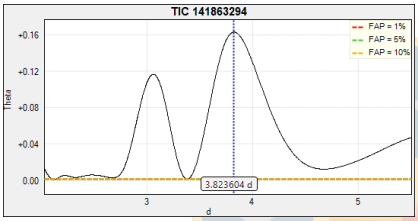

(a) Rotation period using GLS

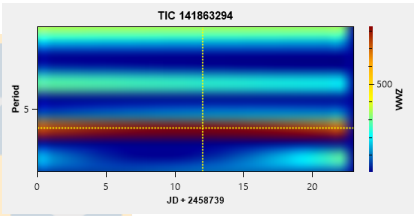

(b) Rotation period using WWZ

TIC 233437236

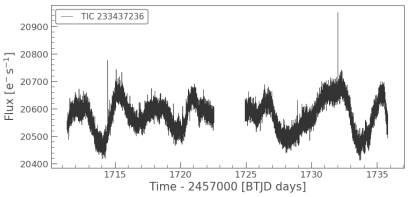

(a) Lightcurve of TIC 233437236

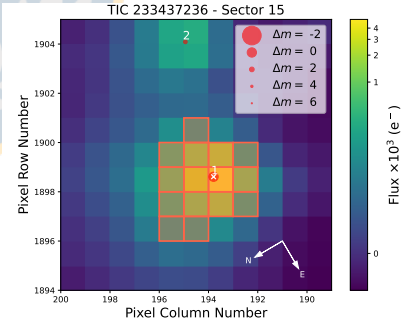

(b) Target Pixel File (TPF) of TIC 233437236

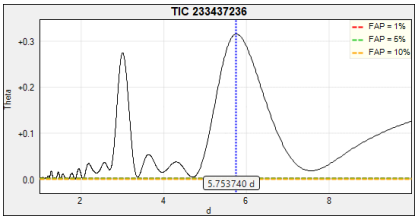

(c) Rotation period using GLS

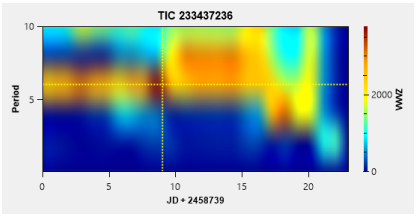

(d) Rotation period using WWZ

TIC 198154161

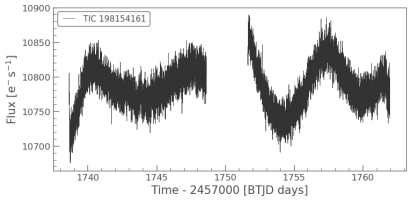

(a) Lightcurve of TIC 198154161

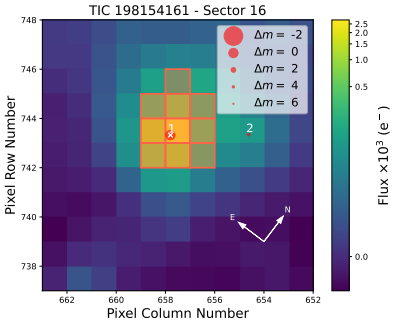

(b) Target Pixel File (TPF) of TIC 198154161

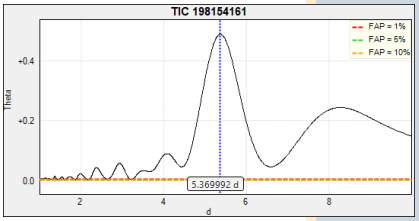

(c) Rotation period using GLS

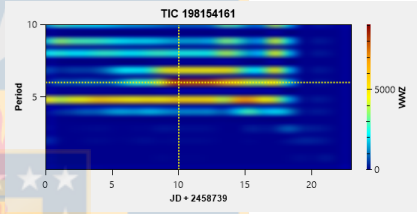

(d) Rotation period using WWZ

TIC 10728867

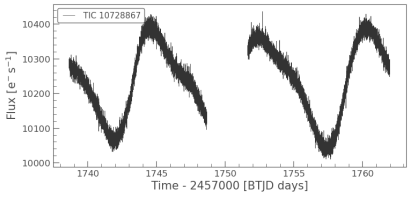

(a) Lightcurve of TIC 10728867

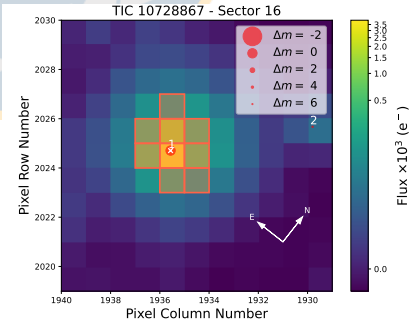

(b) Target Pixel File (TPF) of TIC 10728867

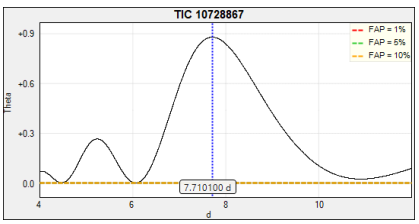

(c) Rotation period using GLS

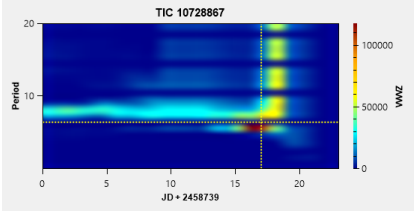

(d) Rotation period using WWZ

TIC 310379752

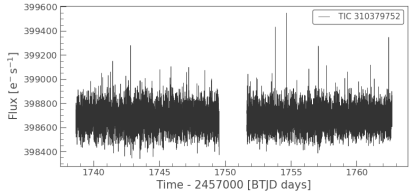

(a) Lightcurve of TIC 310379752

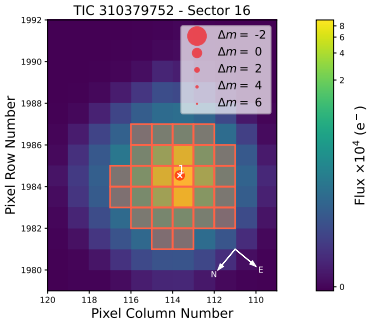

(b) Target Pixel File (TPF) of TIC 310379752

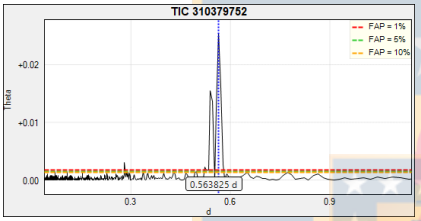

(c) Rotation period using GLS

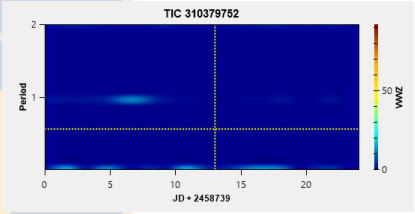

(d) Rotation period using WWZ

TIC 1001276338

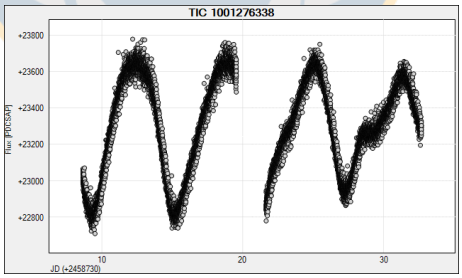

Lightcurve of TIC 1001276338

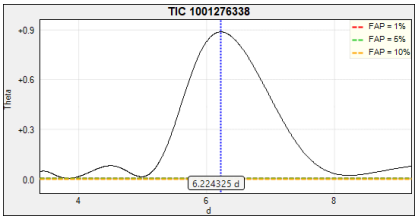

(a) Rotation period using GLS

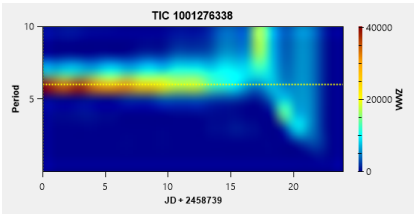

(b) Rotation period using WWZ

TIC 445859773

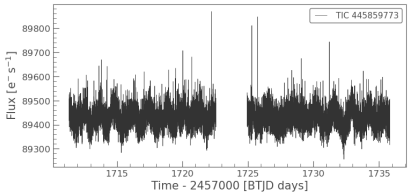

(a) Lightcurve of TIC 445859773

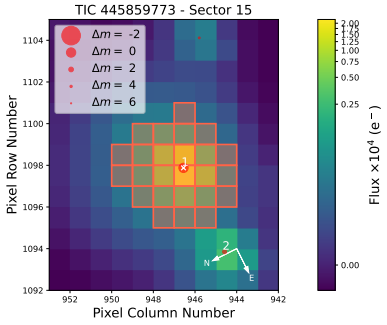

(b) Target Pixel File (TPF) of TIC 445859773

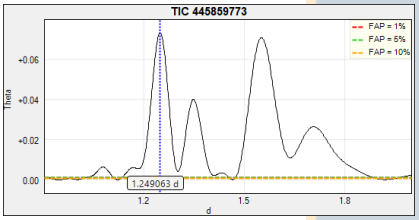

(c) Rotation period using GLS

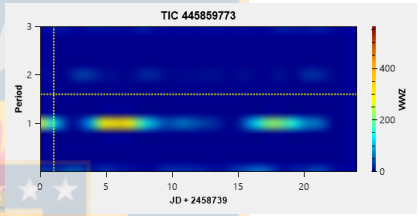

(d) Rotation period using WWZ

TIC 313322899

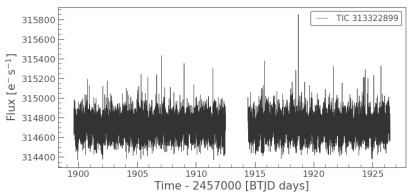

(a) Lightcurve of TIC 313322899

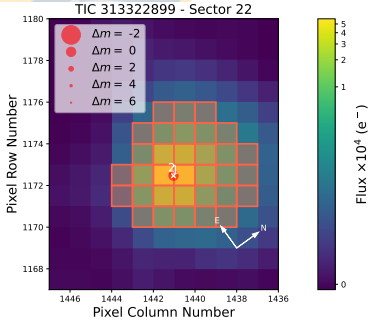

(b) Target Pixel File (TPF) of TIC 313322899

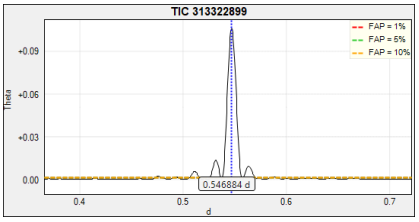

(c) Rotation period using GLS

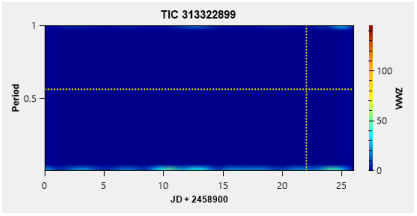

(d) Rotation period using WWZ

TIC 166089535

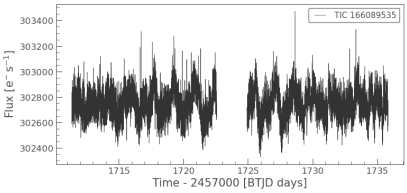

(a) Lightcurve of TIC 166089535

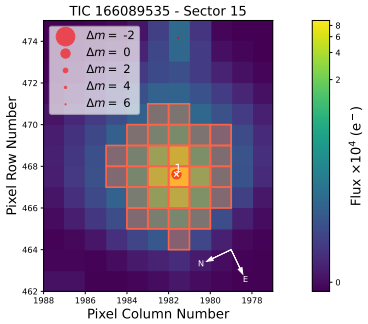

(b) Target Pixel File (TPF) of TIC 166089535

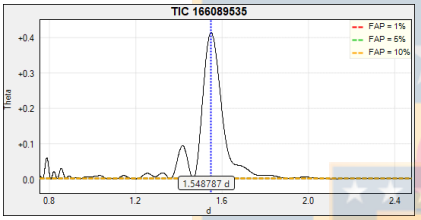

(c) Rotation period using GLS

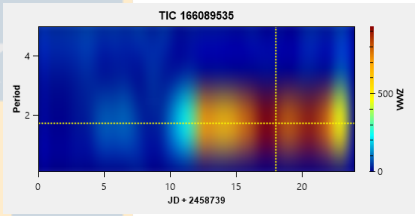

(d) Rotation period using WWZ

TIC 459246945

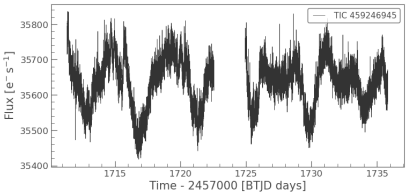

(a) Lightcurve of TIC 459246945

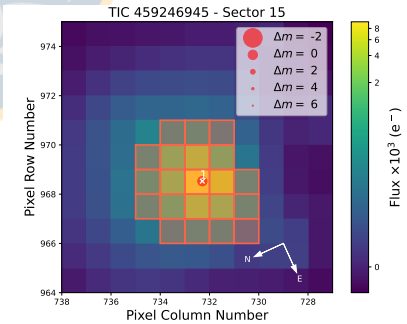

(b) Target Pixel File (TPF) of TIC 459246945

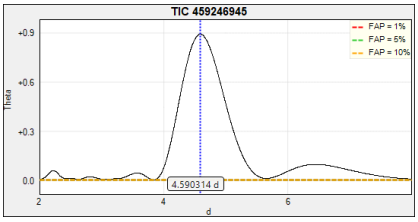

(c) Rotation period using GLS

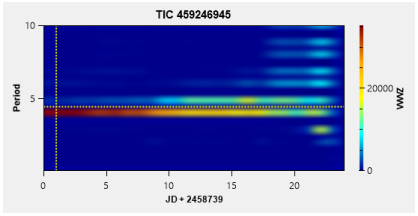

(d) Rotation period using WWZ

TIC 313338124

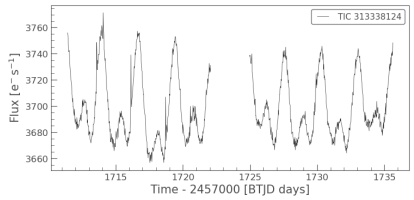

(a) Lightcurve of TIC 313338124

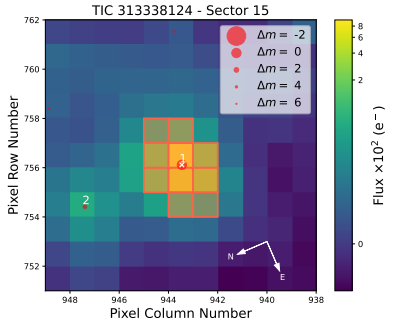

(b) Target Pixel File (TPF) of TIC 313338124

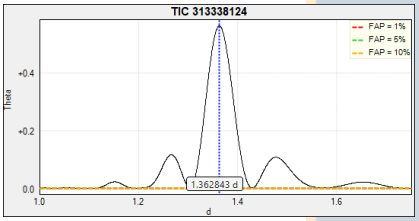

(c) Rotation period using GLS

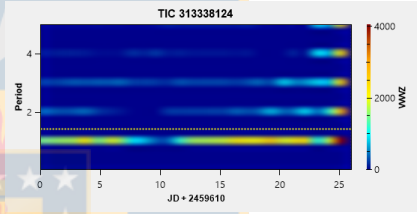

(d) Rotation period using WWZ

TIC 298162216

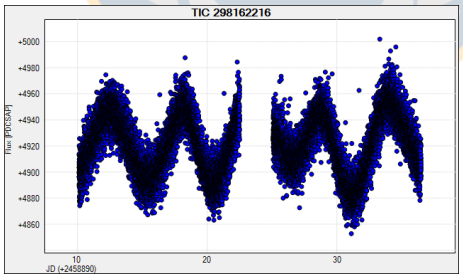

Lightcurve of TIC 298162216

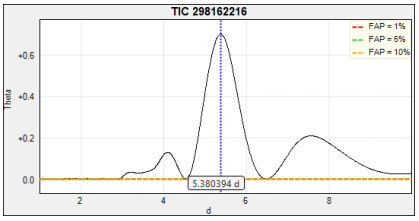

(a) Rotation period using GLS

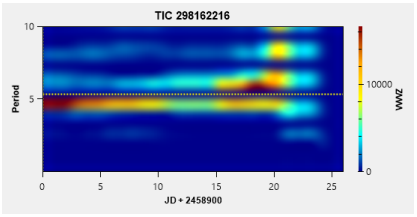

(b) Rotation period using WWZ

TIC 298163080

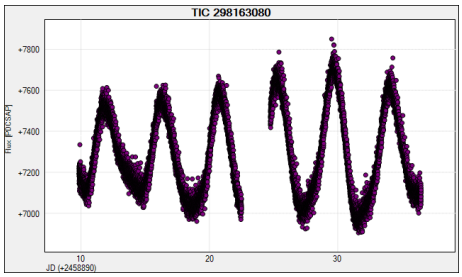

Lightcurve of TIC 298163080

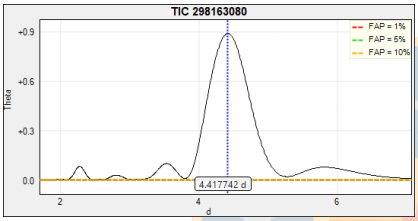

(a) Rotation period using GLS

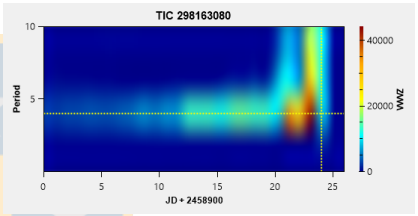

(b) Rotation period using WWZ

TIC 159613447

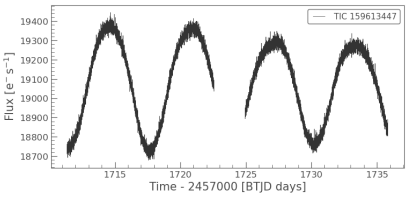

(a) Lightcurve of TIC 159613447

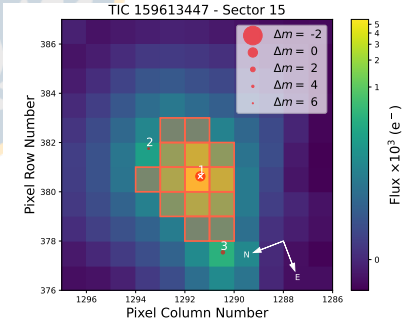

(b) Target Pixel File (TPF) of TIC 159613447

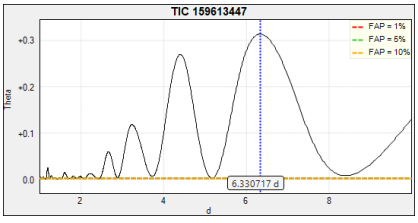

(c) Rotation period using GLS

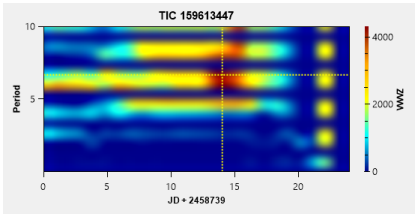

(d) Rotation period using WWZ

TIC 158462948

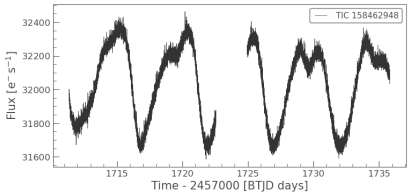

(a) Lightcurve of TIC 158462948

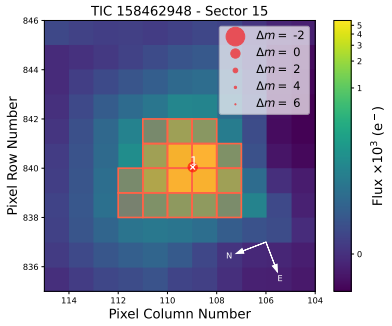

(b) Target Pixel File (TPF) of TIC 158462948

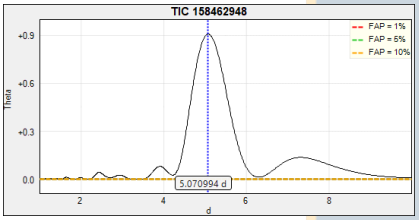

(c) Rotation period using GLS

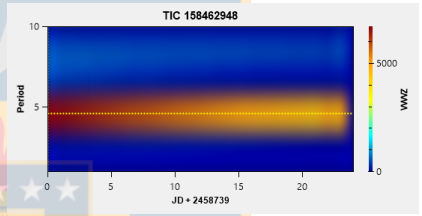

(d) Rotation period using WWZ

TIC 159631183

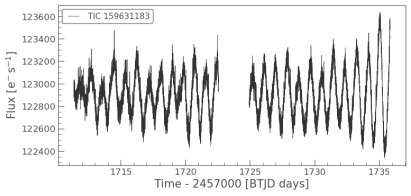

(a) Lightcurve of TIC 159631183

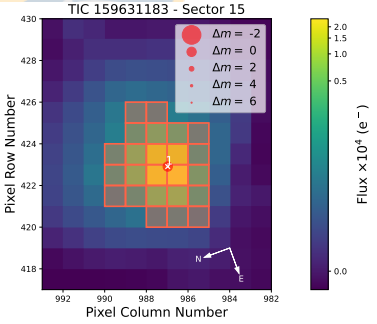

(b) Target Pixel File (TPF) of TIC 159631183

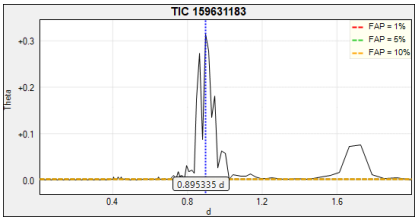

(c) Rotation period using GLS

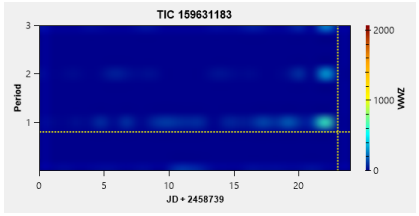

(d) Rotation period using WWZ

TIC 159636302

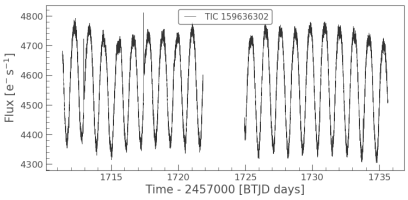

(a) Lightcurve of TIC 159636302

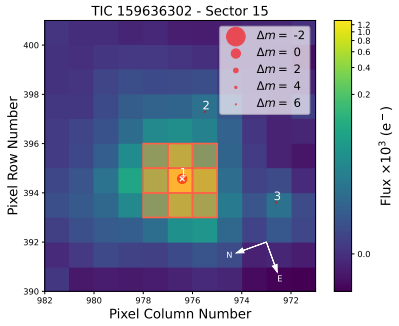

(b) Target Pixel File (TPF) of TIC 159636302

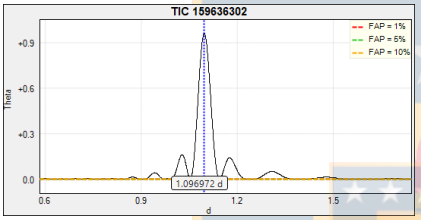

(c) Rotation period using GLS

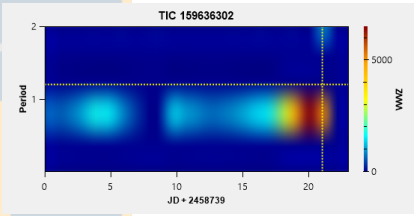

(d) Rotation period using WWZ

TIC 158541117

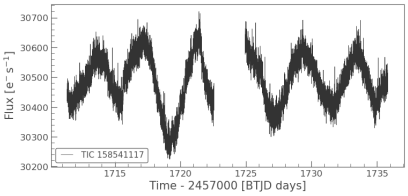

(a) Lightcurve of TIC 158541117

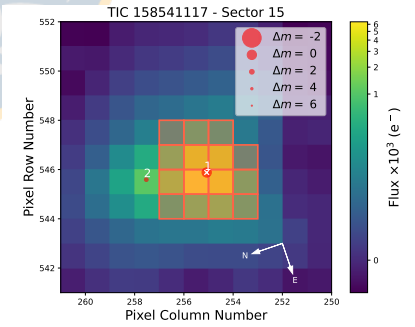

(b) Target Pixel File (TPF) of TIC 158541117

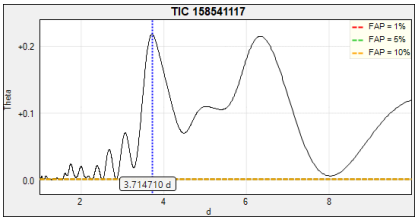

(c) Rotation period using GLS

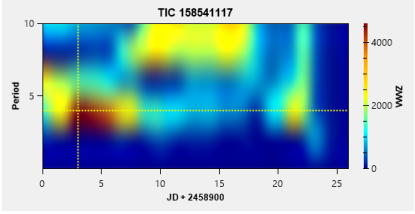

(d) Rotation period using WWZ

TIC 161024760

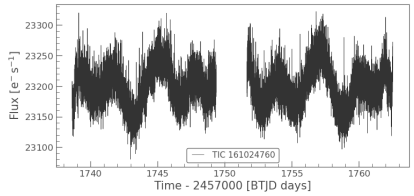

(a) Lightcurve of TIC 161024760

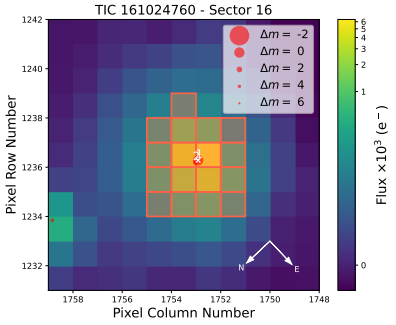

(b) Target Pixel File (TPF) of TIC 161024760

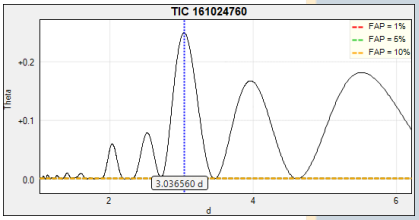

(c) Rotation period using GLS

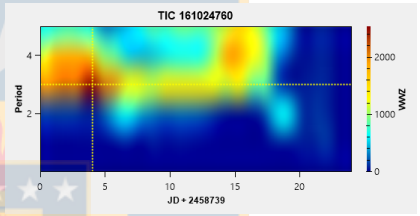

(d) Rotation period using WWZ

TIC 158579468

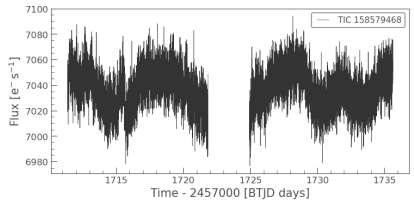

(a) Lightcurve of TIC 158579468

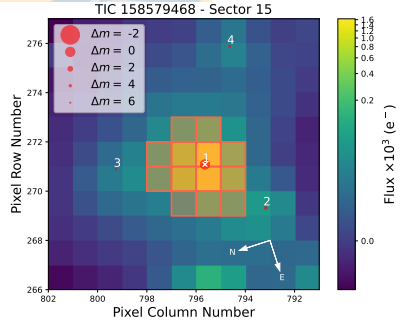

(b) Target Pixel File (TPF) of TIC 158579468

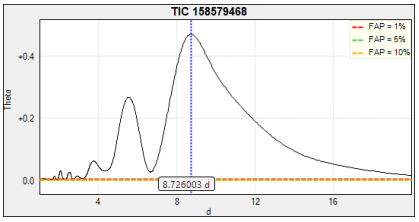

(c) Rotation period using GLS

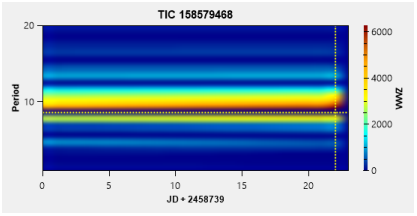

(d) Rotation period using WWZ

TIC 161029191

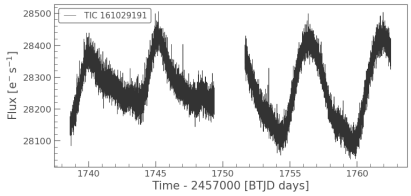

(a) Lightcurve of TIC 161029191

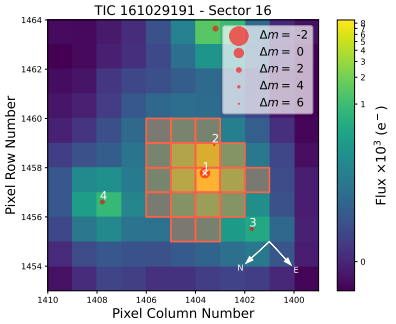

(b) Target Pixel File (TPF) of TIC 161029191

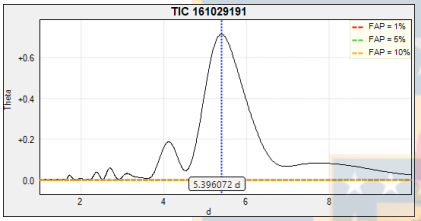

(c) Rotation period using GLS

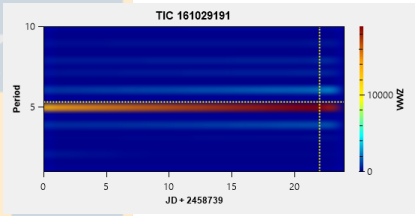

(d) Rotation period using WWZ

TIC 1102311836

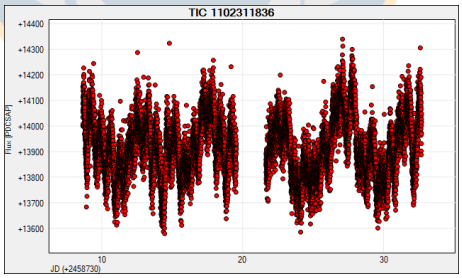

Lightcurve of TIC 1102311836

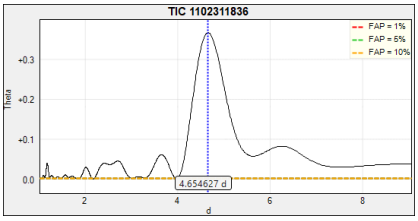

(a) Rotation period using GLS

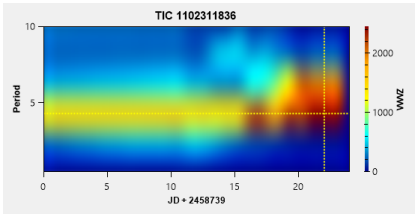

(b) Rotation period using WWZ

TIC 1102311837

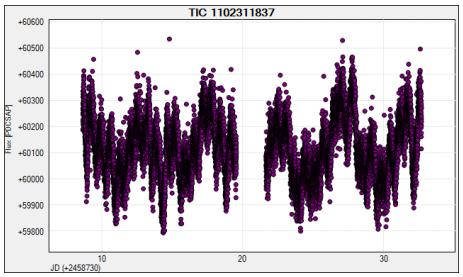

Lightcurve of TIC 1102311837

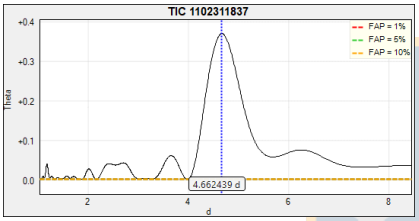

(a) Rotation period using GLS

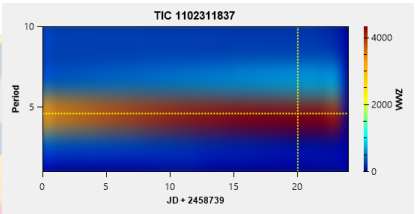

(b) Rotation period using WWZ

TIC 462572935

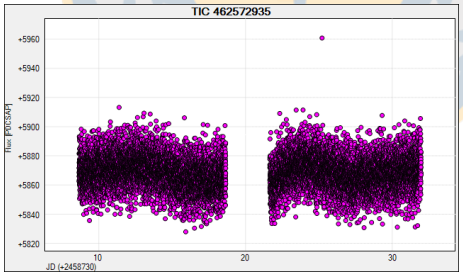

Lightcurve of TIC 462572935

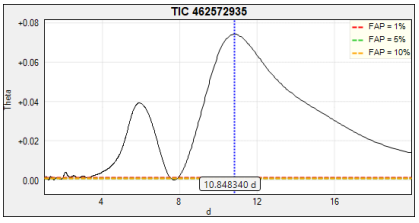

(a) Rotation period using GLS

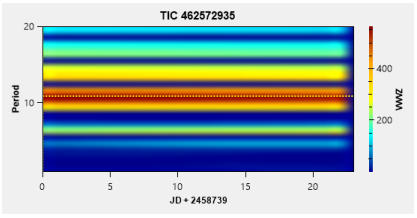

(b) Rotation period using WWZ

TIC 137832480

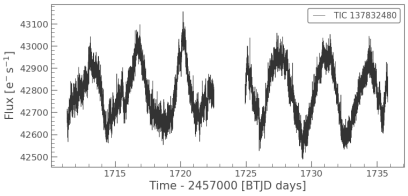

(a) Lightcurve of TIC 137832480

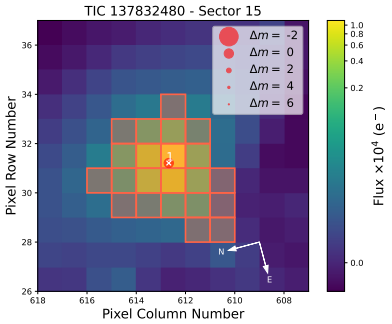

(b) Target Pixel File (TPF) of TIC 137832480

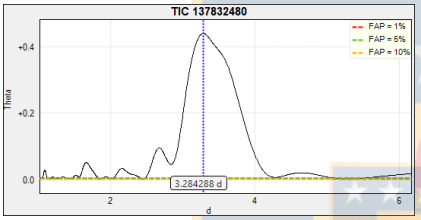

(c) Rotation period using GLS

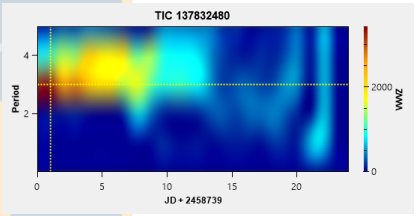

(d) Rotation period using WWZ

TIC 137834492

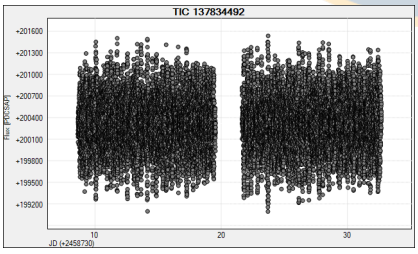

(a) Lightcurve of TIC 137834492

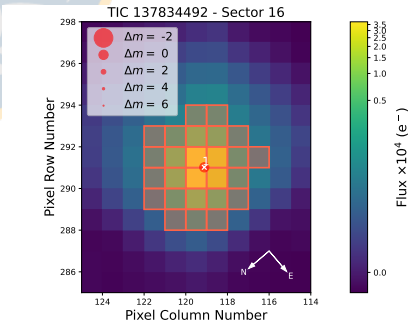

(b) Target Pixel File (TPF) of TIC 137834492

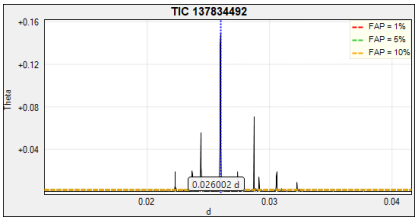

(c) Rotation period using GLS

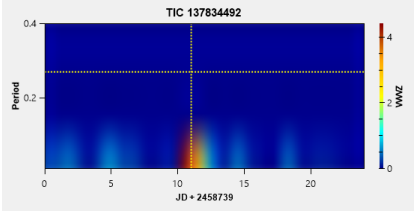

(d) Rotation period using WWZ

TIC 137834559

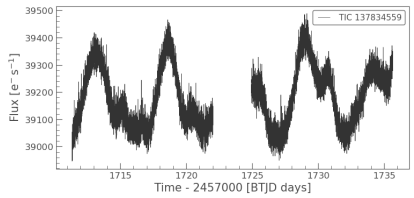

(a) Lightcurve of TIC 137834559

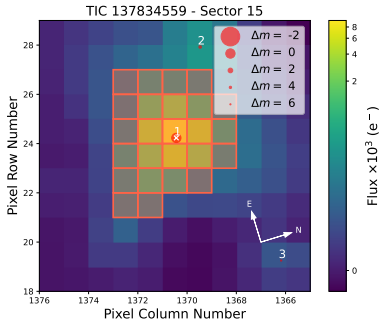

(b) Target Pixel File (TPF) of TIC 137834559

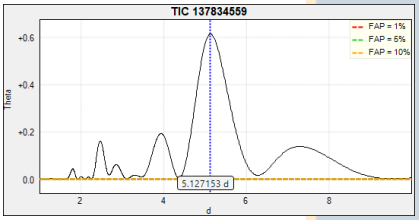

(c) Rotation period using GLS

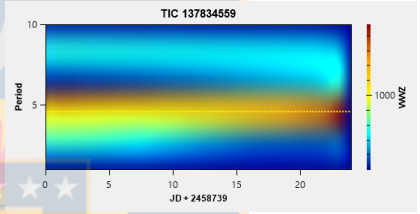

(d) Rotation period using WWZ

TIC 202425640

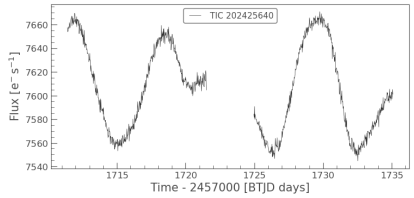

(a) Lightcurve of TIC 202425640

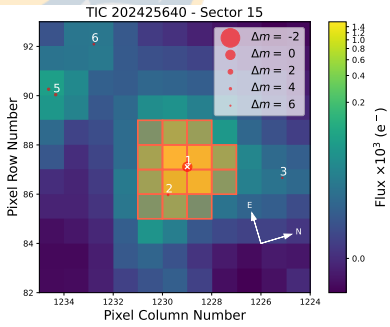

(b) Target Pixel File (TPF) of TIC 202425640

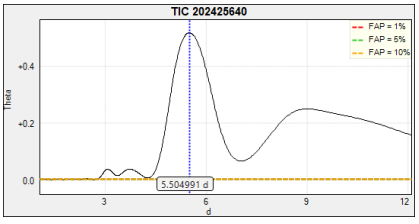

(c) Rotation period using GLS

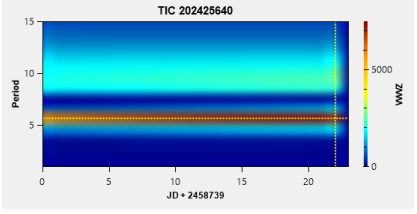

(d) Rotation period using WWZ

TIC 232541198

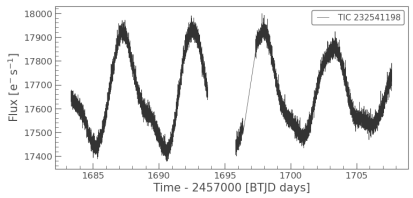

(a) Lightcurve of TIC 232541198

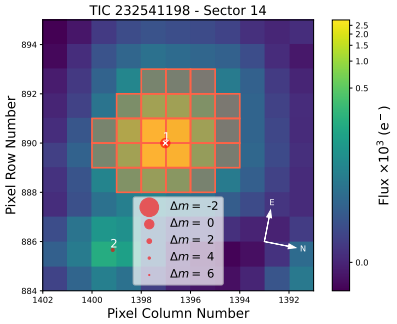

(b) Target Pixel File (TPF) of TIC 232541198

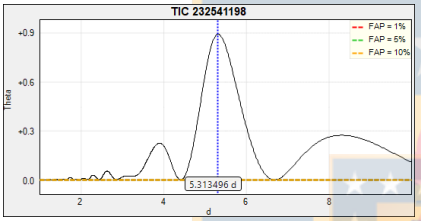

(c) Rotation period using GLS

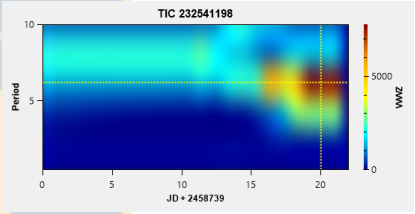

(d) Rotation period using WWZ

TIC 165628355

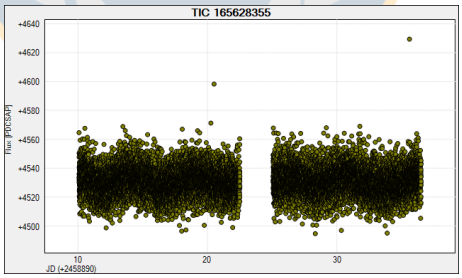

Lightcurve of TIC 165628355

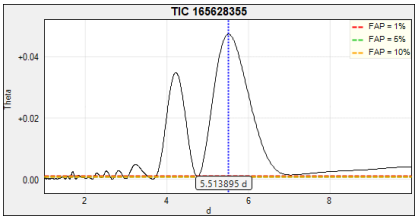

(a) Rotation period using GLS

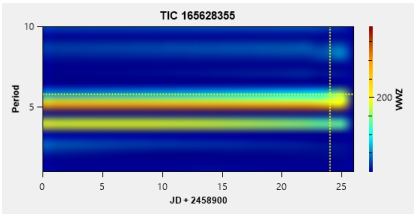

(b) Rotation period using WWZ

TIC 165719269

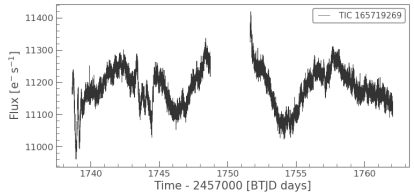

(a) Lightcurve of TIC 165719269

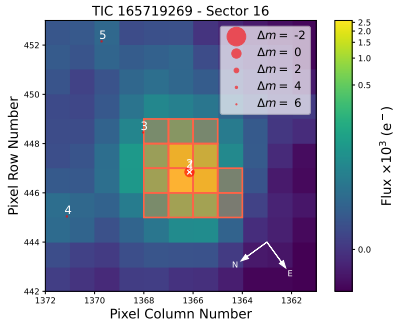

(b) Target Pixel File (TPF) of TIC 165719269

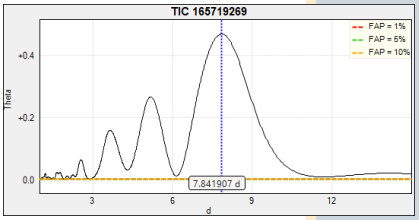

(c) Rotation period using GLS

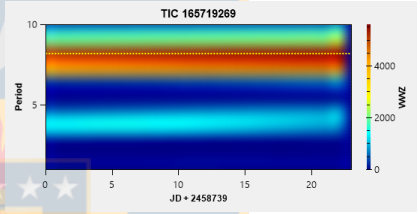

(d) Rotation period using WWZ

TIC 202510436

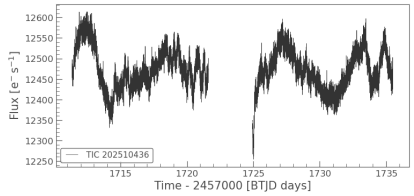

(a) Lightcurve of TIC 202510436

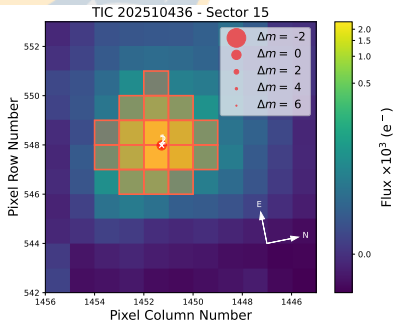

(b) Target Pixel File (TPF) of TIC 202510436

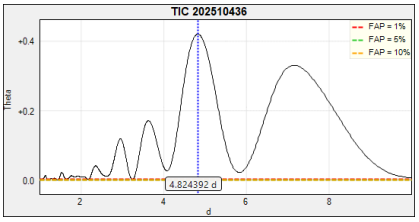

(c) Rotation period using GLS

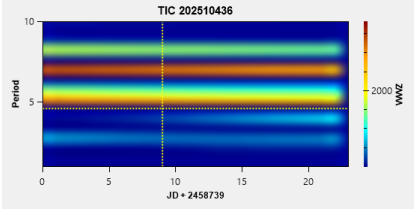

(d) Rotation period using WWZ

TIC 159769293

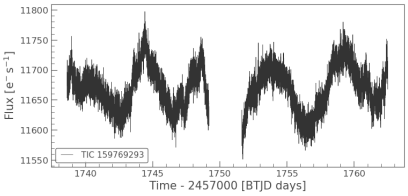

(a) Lightcurve of TIC 159769293

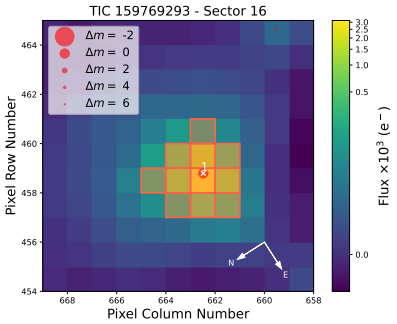

(b) Target Pixel File (TPF) of TIC 159769293

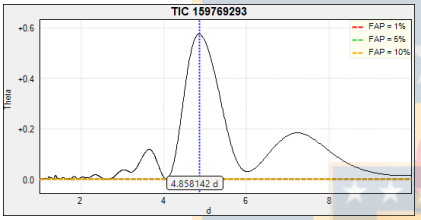

(c) Rotation period using GLS

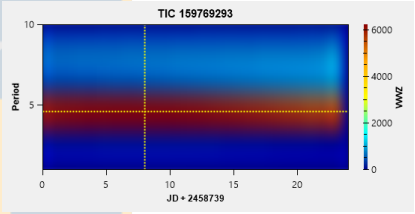

(d) Rotation period using WWZ

TIC 159873822

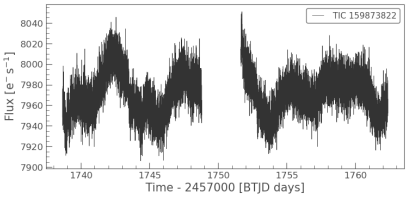

(a) Lightcurve of TIC 159873822

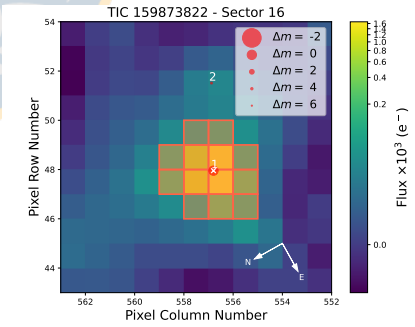

(b) Target Pixel File (TPF) of TIC 159873822

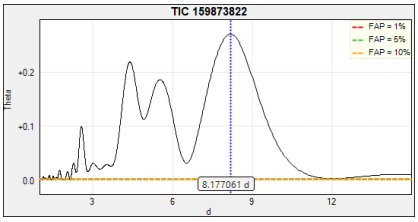

(c) Rotation period using GLS

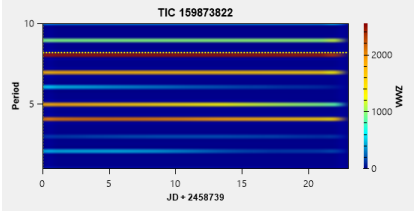

(d) Rotation period using WWZ

TIC 159871737

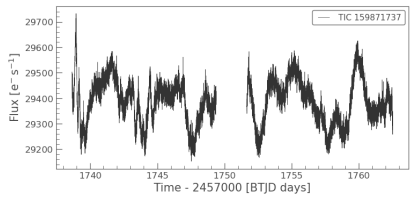

(a) Lightcurve of TIC 159871737

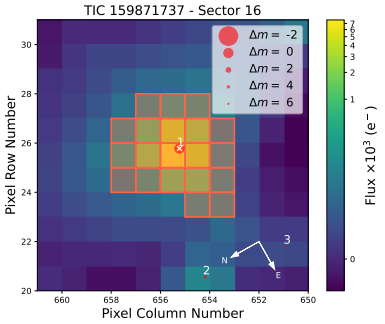

(b) Target Pixel File (TPF) of TIC 159871737

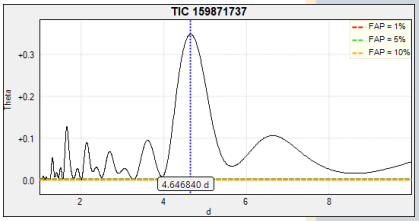

(c) Rotation period using GLS

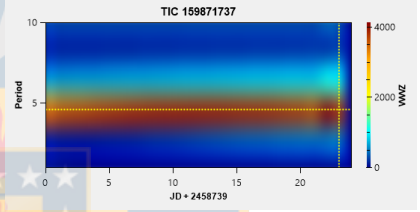

(d) Rotation period using WWZ

TIC 159879031

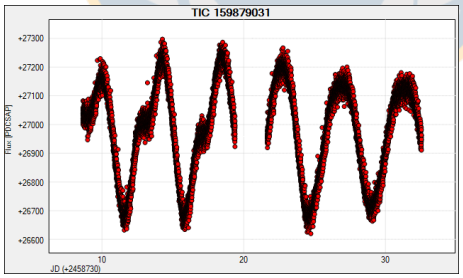

Lightcurve of TIC 159879031

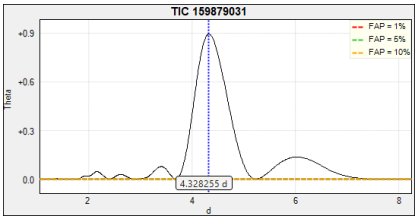

(a) Rotation period using GLS

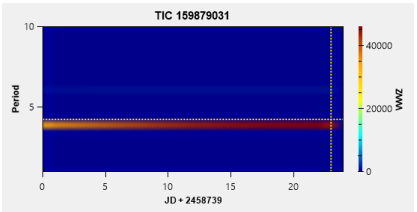

(b) Rotation period using WWZ

TIC 159922985

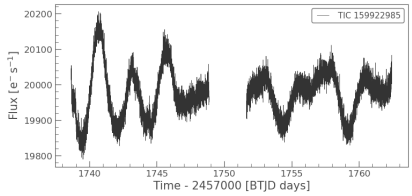

(a) Lightcurve of TIC 159922985

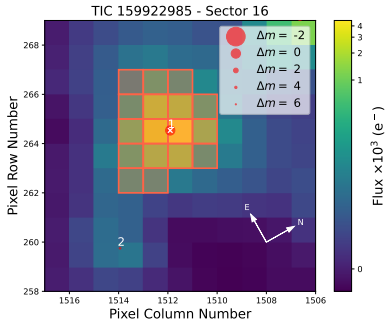

(b) Target Pixel File (TPF) of TIC 159922985

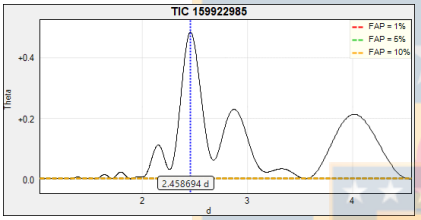

(c) Rotation period using GLS

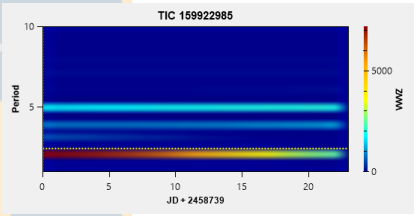

(d) Rotation period using WWZ

TIC 219479795

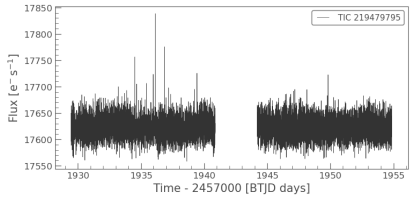

(a) Lightcurve of TIC 219479795

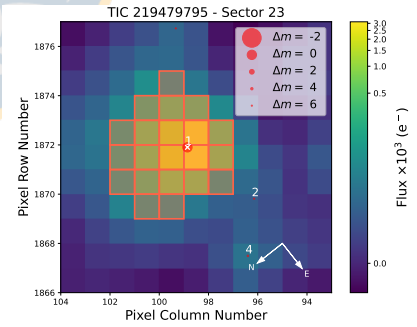

(b) Target Pixel File (TPF) of TIC 219479795

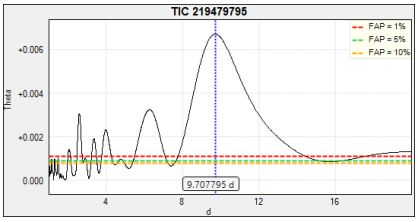

(c) Rotation period using GLS

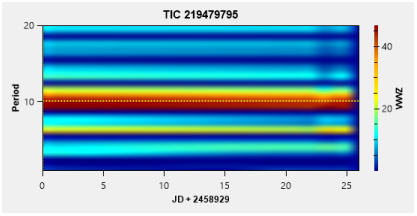

(d) Rotation period using WWZ

Exploring the magnetism of stars using TESS data

J.I. Soto[1], S.V. Jeffers[2], D.R.G. Schleicher[1] & J.A. Rosales[3]

[1] *Departamento de Astronomía, Universidad de Concepción, Chile*
[2] *Institut für Astrophysik, Georg-August-Universität Göttingen, Alemania*
[3] *Main Astronomical Observatory, National Academy of Sciences of Ukraine, Ucrania*

Contact / javieraisoto@udec.cl

Resumen / Algunos aspectos del origen de la actividad magnética en las estrellas aún no se conocen suficientemente bien. Aunque las primeras investigaciones que exploraban la relación entre el periodo de rotación estelar y la actividad magnética indicaban la posible existencia de una rama activa y otra inactiva, con datos más recientes no está tan claro si se trata realmente de dos regímenes distintos. Se cree que esto es una consecuencia de la acción de la dinamo dependiente de la rotación, que produce campos magnéticos que intervienen en la actividad estelar. Durante este estudio, investigamos si se puede utilizar datos de TESS para determinar los períodos de rotación mediante los métodos de Lomb-Scargle Generalizado y Wavelet, y comprobaremos si ambos métodos arrojan resultados coherentes.

Abstract / Some aspects of the origin of magnetic activity in stars are still not sufficiently understood. While initial investigations exploring the relationship between the stellar rotation period and magnetic activity indicated the possible existence of an active and an inactive branch, with more recent data it is less clear whether these are two distinct regimes. This could be a consequence of rotation-dependent dynamo action, which produces magnetic fields that are involved in stellar activity. In this study, we explore whether TESS data can be used to derive stellar rotation periods using the Generalised Lomb-Scargle and Wavelet methods, and test whether the two methods yield consistent results.

Keywords / stars: activity — stars: rotation — stars: solar-type

1. Introduction

The stellar rotation has been a key parameter in deriving stellar ages and is closely related to magnetic activity. One widely used technique for deriving rotation periods has been photometry. Another technique was presented by Eberhard & Schwarzschild (1913), where they first proposed the measurement of stellar activity in cool stars through the emission of the Ca II H+K core from the nucleus. In an attempt to demonstrate this hypothesis, the Mount Wilson project measured the chromospheric activity of over a thousand stars (Wilson, 1968); (Duncan et al., 1991), discovering that cool stars have cycles of magnetic action, classifying the stars into an Active Branch and an Inactive Branch. Baliunas et al. (1995) concluded that there are different stellar populations with three different activity cycles. Noyes et al. (1984) noted that the calcium emission flux depends on the Rossby number R_o, of the form $R_o = P_{rot}/4\pi\tau_c$, with P_{rot} the stellar rotation period and τ_c the stellar convection timescale. This relation was subsequently studied by Bohm-Vitense (2007)), where $R_o \equiv P_{rot}/\tau_c$. In a recent study, Boro Saikia et al. (2018) have determined activity for a larger sample of stars, finding that potentially the relation between rotation and activity period may form a continuum between the active and inactive branches, rather than a strict relation to them. The present work provides an analysis of two methods to estimate the rotation period of a star, the Generalised Lomb Scargle method, and the Wavelet transforms, to recognize which method is more accurate in obtaining rotation periods.

2. Methodology

We consider the star EV Lac (TIC 154101678; $\alpha_{2000} = 22:46:49.73$, $\delta_{2000} = +44:20:02.37$) as a reference. EV Lac is a common red dwarf of the known period. Pettersen (1980) was the first to determine a rotation period for this star, successfully finding a period of 4.378 days. The TESS data have been downloaded directly from the Mikulski Archive for Space Telescopes (MAST) database [*]. With the Kepler space mission (Borucki et al., 2010) led to the discovery of flares in several F-, G- and A-type stars (Balona, 2012).

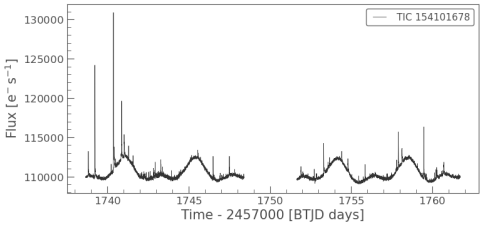

Figure 1: EV Lac light curve (TIC 154101678)

[*] https://archive.stsci.edu/

We use Lightkurve's Target Pixel File (TPF) **. We have applied custom apertures "create_threshold_mask(threshold=3)" which selects all pixels that have a flux greater than 3 standard deviations above the average luminosity. The tube aperture is small in this case but avoids capturing light from the background star. Once the light curve is modified, we save it as a FITS file.

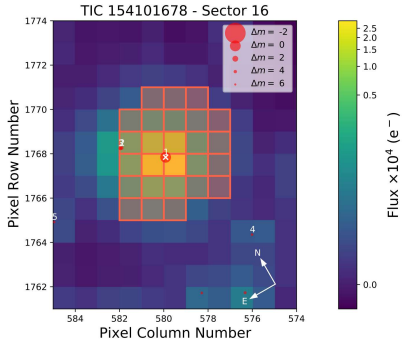

Figure 2: Target pixel file (TPF) of the star EV Lac. The centered red circle corresponds to the source in the field with scaled magnitudes. magnitudes. The white cross indicates the location of the target. The aperture mask used by the pipeline to extract the photometry was also plotted on the TPF.

In addition, we applied Peranso's LOWESS (Locally-Weighted Scatterplot Smoothing) *** technique. This method estimates the slope of each point by plotting a line of intersection. It creates a smooth best-fit curve and eliminates outliers to avoid incorporating them in subsequent period analysis calculations.

2.1. The Generalised Lomb-Scargle periodogram

In this work, we have used the Generalised Lomb-Scargle periodogram (GLS) from Zechmeister & Kürster (2009). GLS is a commonly used statistical tool that allows the efficient calculation of a Fourier-type power spectrum estimator from unevenly sampled data to determine the oscillation period. The Peranso software was used to perform an analysis with the GLS method and determine the rotation period of EV Lac. The following figure (see Figure 3) shows a period found for the EV Lac star of 4.33±0.13 days. This is a period quite close and in agreement with the periods found in the literature.

2.2. The wavelet transform

The wavelet transform is a method for analyzing signals with a high resolution in both the frequency and time domain (Torrence & Compo, 1998). This is achieved by working with different time scales Burrus et al. (1998). The Wavelet transform consists of a series of functions called wavelets. We can analogously decompose the light curve of a star by frequencies represented in the power spectrum at different scales. With the wavelet being placed in time, our signal can be convoluted with the wavelet in different time ranges. Bravo et al. (2014) applied the so-called Morlet wavelet to Kepler and CoRoT light curves, in stars with planetary transits, binary systems, a variable star dominated by magnetic activity, and pulsating stars, where they identified patterns in the rotation period due to active regions affecting the light curves.
We have analyzed the obtaining of the period using the Weighted Wavelet Z-transform (WWZ) method, also with the Peranso software. The WWZ is based on the Morlet wavelet (see (Grossmann et al., 1989)). In it, we found a period of 4.24 days, which is close to the values previously obtained in the literature.

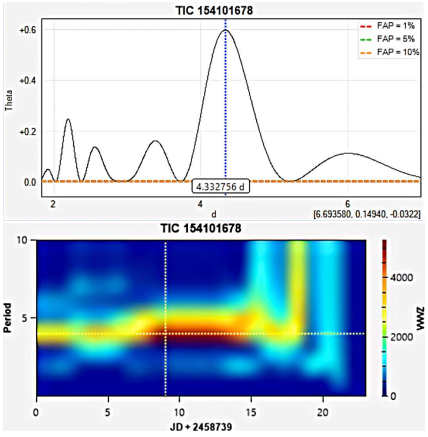

Figure 3: *Top panel:* Rotation period found for EV Lac by the Generalised Lomb Scargle method. *Bottom panel:* The rotation period found by the WWZ method is 4.24 days for the EV Lac star. The x-axis represents time, the y-axis represents frequency, and a color (z-axis) is used to plot the WWZ response.

3. Results

A total of 53 stars have been extracted from Table A.2 of the Boro Saikia et al. (2018) article. For five stars (see Tab. 1), we found a concordance with the periods given in the aforementioned paper. However, for stars where Boro Saikia et al. (2018) reported rotation periods larger than 10 days, both methods indicate shorter periods when applied to the TESS data, though typically with a lower statistical significance. We consider this likely to be a limitation due to the observing time windows of TESS and to potentially reflect shorter periodicities or time variations, though not to correspond to the physical rotation period. In Figs. 4, we reproduce the corresponding plots on the activity - rotation period relation from Boro Saikia et al. (2018), showing in red the new periods derived from TESS and in black the periods from their original data. We limit ourselves here to data points consistent with the previous periods.

** https://docs.lightkurve.org/
*** https://www.cbabelgium.com/peranso/

Name	Period found using Wavelet method [d]	Period using GLS [d]	Period from Boro Saikia et al. (2018) [d]	Period from Literature [d]
EV Lac	4.24 ± 0.46	4.33 ± 0.13	-	4.37 ((Pettersen, 1980))
HD20630	9.00 ± 0.15	9.02 ± 1.05	9.24	9.2 (Brandenburg et al. (2017))
HD26913	6.76 ± 0.09	6.84 ± 0.23	7.1	7.15 (Saar & Brandenburg (1999))
HD82443	5.32 ± 0.05	5.43 ± 0.14	5.37	5.37 (Messina et al. (1999))
HD115043	5.68 ± 0.07	5.67 ± 0.19	5.86	5.86 (Hempelmann et al. (2015))
HD115383	3.52 ± 0.02	3.40 ± 0.06	3.33	3.33 (Saar & Brandenburg (1999))

Table 1: Table schematizing the stellar rotation periods calculated according to the Wavelet method and the GLS method, compared with the stellar rotation periods found in the literature. From a total of 53 stars present in Table A.2 of the article (Boro Saikia et al., 2018), it has been obtained closely the rotation period for 5 stars listed in the table.

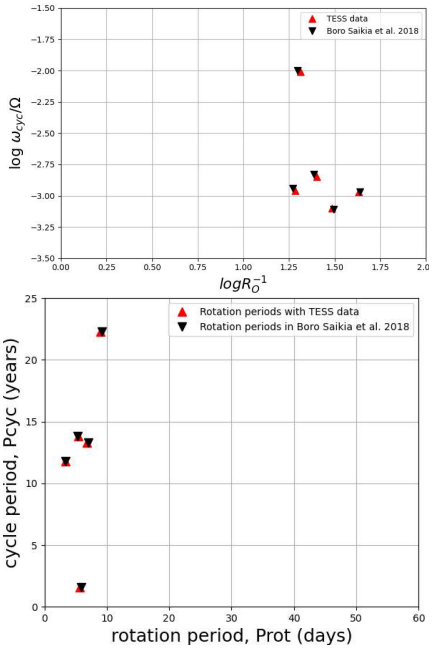

Figure 4: *Top panel:* ω_{cyc} / Ω vs. R_o^{-1} for stars from Table A.2 Boro Saikia et al. (2018), which closely match the rotation periods obtained with TESS data. *Bottom panel:* Activity-cycle period in years as a function of rotation period in days for stars in Table A.2 from Boro Saikia et al. (2018)

4. Conclusion

We find that stellar rotation periods can be derived from the TESS data if the stars have sufficiently short periods of less than 10 days. In these cases, both the generalized Lomb Scargle method and the Wavelet method provide results consistent with each other, showing low statistical error highlighting the effectiveness of both methods analyzed.

We propose that the reason for this is that the light curves provided by TESS have gaps that could interfere with the actual calculation of the rotation period. It is proposed that the obtained periods are far from most of the rotation periods present in Table A.2 of (Boro Saikia et al., 2018) due to the limitation of the software used. Handling two competent and innovative methods allows us to recognize their effectiveness of one over the other, apply them to different astrophysical phenomena related to signal analysis.

Acknowledgements: We thank Dr. Mennickent, R. E. of the Astronomy Department of the Universidad de Concepción for contributing to this work with their scientific expertise and providing valuable guidance and corrections for the development of this article. We are also grateful for the financial support of the FONDECYT regular project 1201280, for allowing the development of this research.

References

Baliunas S.L., et al., 1995, ApJ, 438, 269
Balona L.A., 2012, MNRAS, 423, 3420
Bohm-Vitense E., 2007, The Astrophysical Journal, 657, 486
Boro Saikia S., et al., 2018, A&A, 616, A108
Borucki W.J., et al., 2010, Science, 327, 977
Brandenburg A., Mathur S., Metcalfe T.S., 2017, ApJ, 845, 79
Bravo J.P., et al., 2014, A&A, 568, A34
Burrus C., Gopinath R., Guo H., 1998, Recherche, 67
Duncan D.K., et al., 1991, ApJS, 76, 383
Eberhard G., Schwarzschild K., 1913, ApJ, 38, 292
Grossmann A., Kronland-Martinet R., Morlet J., 1989, J.M. Combes, A. Grossmann, P. Tchamitchian (Eds.), *Wavelets*, 2–20, Springer Berlin Heidelberg, Berlin, Heidelberg
Hempelmann A., et al., 2015, A&A, 586
Messina S., et al., 1999, åp, 347, 249
Noyes R.W., et al., 1984, ApJ, 279, 763
Pettersen B.R., 1980, AJ, 85, 871
Saar S.H., Brandenburg A., 1999, ApJ, 524, 295
Saar S.H., Brandenburg A., 1999, The Astrophysical Journal, 524, 295
Torrence C., Compo G.P., 1998, Bulletin of the American Meteorological Society, 79, 61
Wilson O.C., 1968, ApJ, 153, 221
Zechmeister M., Kürster M., 2009, A&A, 496, 577